Tomographie à rayons-X pour caractériser l'altération par cristallisation des sels dans des milieux poreux multicouches

Tinhinane Chekai Attia

THESE DE DOCTORAT

ED 211 - Sciences exactes et leurs applications

Présentée et soutenue le : 19 décembre 2023
Par : Tinhinane CHEKAI

Thèse pour obtenir le grade de
Docteur de l'Université de Pau et des Pays de l'Adour
(Spécialité : Génie civil)

Tomographie à rayons-X pour caractériser l'altération par cristallisation des sels dans des milieux poreux multicouches

Thèse dirigée par : Hannelore DERLUYN

JURY

Président du jury

• David GREGOIRE	Professeur des Universités / Université de Pau et des Pays de l'Adour

Rapporteurs

• Masaru ABUKU	Professor / Kindai University
• Kevin BECK	Maître de Conférence HDR / Université d'Orléans

Examinateurs

• Sandrine GEOFFROY	Professeur des Universités / Université Toulouse III
• Noushine SHAHIDZADEH	Professor / University of Amsterdam
• Catherine NOIRIEL	Maître de Conférence HDR / Université Toulouse III
• Ran HOLTZMAN	Associate Professor / Coventry University

Résumé

Dans cette thèse, nous avons abordé un problème courant lié à la durabilité des matériaux de construction et à la préservation du patrimoine culturel : les dommages causés par la cristallisation des sels, en raison de l'interaction entre les sels, les changements environnementaux et les propriétés des matériaux. Alors que de nombreuses études ont examiné des matériaux poreux monocouche, les structures construites ainsi que les objets culturellement précieux sont souvent constitués d'assemblages multicouches. Notre étude s'est principalement concentrée sur la cristallisation des sels dans deux types de matériaux poreux multicouches, en examinant l'impact du type de sel et des propriétés des matériaux. Le premier objet d'étude était les carreaux en céramique hollandaise anciens, composés d'une couche de glaçure et d'un corps en argile. Le deuxième objet d'étude était de milieux poreux modèles fabriqués à partir de billes de verre consolidées, constitués d'une partie hydrophobe et d'une partie hydrophile, imitant un système à deux couches avec une mouillabilité différente, couramment rencontré dans le domaine de la conservation. Nous avons choisi le sulfate de sodium et le chlorure de sodium comme sels d'intérêt. En utilisant la microtomographie à rayons X, nous avons obtenu des données qualitatives et quantitatives de manière non invasive, ce qui nous a permis d'analyser la cinétique de séchage, les schémas d'accumulation de sel et les dommages. Nos résultats ont révélé des différences significatives entre le chlorure de sodium et le sulfate de sodium en termes d'efflorescence et de leur impact sur le séchage. Dans le cas des carreaux hollandais, l'efflorescence de chlorure de sodium s'est révélée rigide, ralentissant considérablement le processus de séchage, tandis que l'efflorescence de sulfate de sodium avait une nature plus légère et n'a pas affecté le séchage. En revanche, lors de l'étude des milieux poreux modèles, l'efflorescence de chlorure de sodium, similaire à celle des carreaux, était rigide, mais a provoqué un effet de pompage, accélérant le taux de séchage lorsqu'il était humide et réduisant le taux de séchage lorsqu'il était sec. Les motifs d'accumulation de sel ont également varié entre les deux sels dans les deux cas, avec de petites taches pour le chlorure de sodium dans les carreaux et de grands amas à l'interface de la glaçure et du corps en argile pour le sulfate de sodium. À noter que les deux sels ont provoqué des dommages macroscopiques sur les carreaux hollandais après plusieurs cycles d'altération par cristallisation. Dans le cas des milieux poreux modèles, les deux sels ont présenté une subflorescence concentrée à l'interface entre les zones hydrophobes et hydrophiles, avec le chlorure de sodium montrant une pénétration de sel dans la partie hydrophobe à la fin du processus de séchage, et le sulfate de sodium présentant une certaine accumulation dans la partie hydrophile, en dehors de l'interface. Les résultats de cette thèse sont une contribution précieuse à la littérature existante, offrant des informations essentielles aux conservateurs cherchant à développer des méthodes de conservation plus efficaces pour atténuer les dommages dus à la cristallisation des sels dans les matériaux de construction et les objets culturels.

Mots-clés : Milieux poreux en couches, Tomographie par rayons X, Cristallisation du sel, Altération, Analyse d'image

Abstract

In this thesis, we addressed a common issue in both the durability of building materials and cultural heritage preservation: crystallization damage resulting from the interplay of salts, environmental changes, and material properties. While numerous studies have examined single porous materials, built structures as well as culturally valuable artefacts often consist of multilayered assemblies. We focused on studying salt crystallization in two types of multilayered porous materials and investigated the effects of both the salt type and the material properties. The first object of study was antique Dutch ceramic tiles, which consist of a glaze layer and a clay body. The second object of study was model porous media made of consolidated glass beads that consist of a hydrophobic and a hydrophilic part, mimicking a two-layered system with different wettability that is often encountered in the conservation field. Sodium sulfate and sodium chloride were selected as the salts of interest. Using X-ray micro-computed tomography, we obtained both qualitative and quantitative data in a non-invasive manner on the drying kinetics and salt accumulation patterns for both porous media, as well as on damage for the case of the Dutch tiles. Finally, a pore network extraction method was merged with the image analysis workflow for the model porous media, enabling a detailed analysis of drying and salt accumulation at the pore scale. The behaviour of sodium chloride and sodium sulfate in terms of accumulation patterns and their effects on drying in the two studied cases were defined. We observed distinctive characteristics of efflorescence and their impact on the drying kinetics. In the case of the tiles, sodium chloride efflorescence was found to be stiff and significantly slowed down the drying process, whereas sodium sulfate efflorescence exhibited a fluffy nature and did not impact the tiles' drying. On the other hand, when studying the model porous media, sodium chloride efflorescence, like in the tiles, was stiff, but induced here a pumping effect that accelerated the drying rate when wet and resulted in a reduction in the drying rate when dry. In the case of sodium sulfate, its efflorescence was fluffy and led to a reduction in the drying rate. We additionally observed that the accumulation patterns differed. In the case of the tiles, sodium chloride formed small patches distributed across the clay body, while sodium sulfate accumulated in large clusters at the interface between the glaze and the clay body. Notably, both salts resulted in macroscopic damage in tiles with intact glazes after several weathering cycles. In the case of the model porous media, both salts exhibited subflorescence concentrated at the interface between the hydrophobic and hydrophilic regions, with sodium chloride showing salt creeping into the hydrophobic part by the end of the drying process, and sodium sulfate displaying some accumulation in the hydrophilic part, apart from the interface. The results of this thesis represent a valuable contribution to the existing literature. We observed how the type of salt affects accumulation patterns and drying behaviour, as well as its response to changes in the wettability of porous materials. The use of X-ray tomography provided 3D information regarding the spatial distribution through time of sodium chloride and sodium sulfate, as well as, for the model porous media, the distribution of brine at the pore scale level. These findings offer important insights for conservators seeking to develop more efficient conservation methods to mitigate salt crystallization damage in building materials and artefacts.

Keywords: Layered porous media, X-ray tomography, Salt crystallization, Weathering, Image analysis

Acknowledgements

I would like to express my gratitude to Kevin Beck and Masaru Abuku for reviewing this work and participating as jury members in the defense. I also thank Catherine Noiriel, Noushine Shahidzadeh, David Gregoire, and Ran Holtzman for their roles as examiners and jury members during my defense.

I want to extend my heartfelt thanks to everyone at the DMEX unit, especially Stéphane Faucher, Pascale Senéchal, and Peter Moonen, whose support, kindness, and insights were invaluable throughout this thesis journey. Huge thanks to David Gregoire for hosting me at the Anglet campus of the LFCR laboratory. I had a blast chatting with the team and learning a ton about mechanical testing and MIP measurements. And to Marie-Pierre Isaure, thank you for your time and expertise with the XRD measurements. I learned a lot and appreciated your guidance! heartfelt thank you goes out to Isabelle Garachon and Kate van Lookeren for their insightful responses to my numerous inquiries about Dutch tiles.

I want to express my gratitude to all the members of the Crystinart project for their invaluable insights over the past three years, especially during our long conversations as PhD students - Nicolo, Rozeline, and myself. A special thank you goes to Noushine Shahidzadeh for welcoming me to her department at the University of Amsterdam, where our discussions were incredibly fruitful. I'm grateful to my thesis supervisor, Hannelore Derluyn, for her meticulous review of this manuscript and her insightful guidance throughout the past three years. Hannelore, thank you for introducing me to the captivating world of X-ray imaging, which I've grown to love. These experiences have equipped me well for the journey into the research world.

I express my sincere gratitude to the people who offered their moral support without any questions, notably Stephane, Othmane, Syrine, Sonia, and Tetiana. These last three years have been a blessing, and I have enjoyed all of our off-work meetings ;)

I want to thank my parents, without whom this work would not be possible. Their support and belief in my dreams, even during challenging times, are invaluable. I would also like to thank my brothers Halim and Massi for their great sense of humour that got me through very difficult moments, and my beloved sister Thiziri, who always shares both my happiness and sadness. In the end, I express my appreciation for the love of my life, my best friend, my dear husband Hamid, who is always by my side, giving me the hope I need and teaching me how to persevere, hold on, and never give up.

Contents

List of Figures

List of Tables

General introduction

Leonardo da Vinci stated "In time, and with water, everything changes" [20, 2, 60], and salt seems to facilitate this statement when it comes to building materials and cultural heritage. And since time does not stand still, this statement also applies to our current constructions. Salt has been introduced into our constructions since the beginning of time. Either through man, such as the Siwa oasis in ancient Egypt, where it was used as a binder to improve the cohesion of mud bricks as far back as 2000 BC. Or it was naturally introduced into the construction from various sources such as groundwater uptake or sea spray.
The damaging impact of salt on construction has been evident throughout history. However, it wasn't until the 19th century that scientific investigation began to take interest in this phenomenon. Despite numerous studies since then, a comprehensive understanding of salt weathering remains not fully achieved.

Damage induced by salt crystallization is influenced by many factors which depend on the material like the structural properties (e.g porosity, pore size distribution) [49, 21, 1, 48], and the environmental conditions exercised on the material like the properties of the salt solution (e.g molar concentration, solubility), the nature of the salts (e.g hydration state, density) and the climatic condition (e.g temperature, relative humidity)[48, 11, 19].

During the drying of the brine-saturated porous material, the salt accumulates in different patterns and locations. This accumulation can have an aesthetic impact without necessarily causing structural damage to the porous material. In such cases, the pattern of salt accumulation is referred to as efflorescence, which is evident when salt accumulates on the exterior surface, as illustrated in Figure 1. When salt accumulates within the porous media, this is referred to as subflorescence. It is typically associated with damage to the porous material and can impact it in various ways, as illustrated in Figure 2.

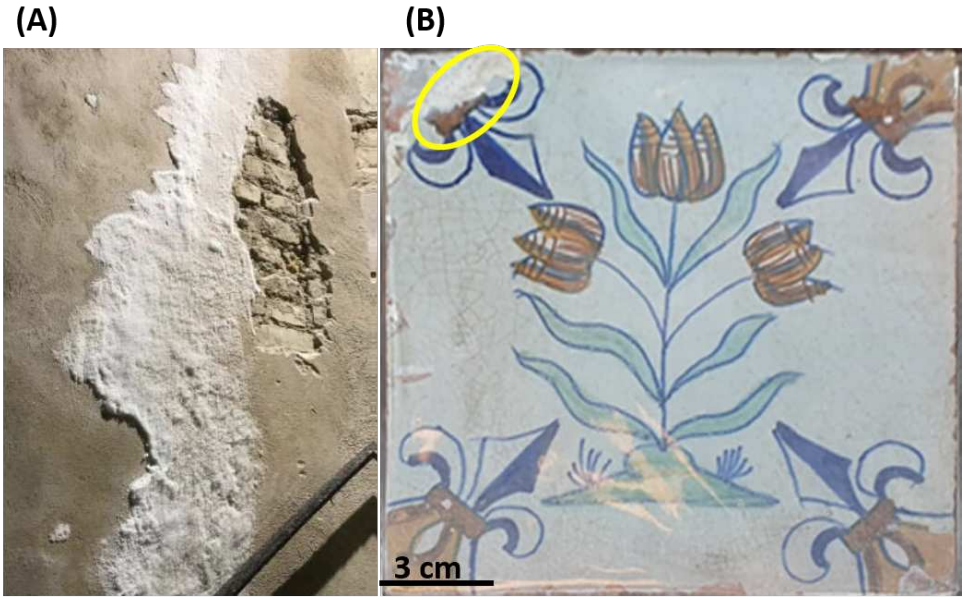

Figure 1: Salt efflorescence: (A) a building wall suffering from sulfates crystallization [3], (B) Dutch tile showing salt efflorescence (Amsterdam, The Netherlands (picture ©T. Chekai))

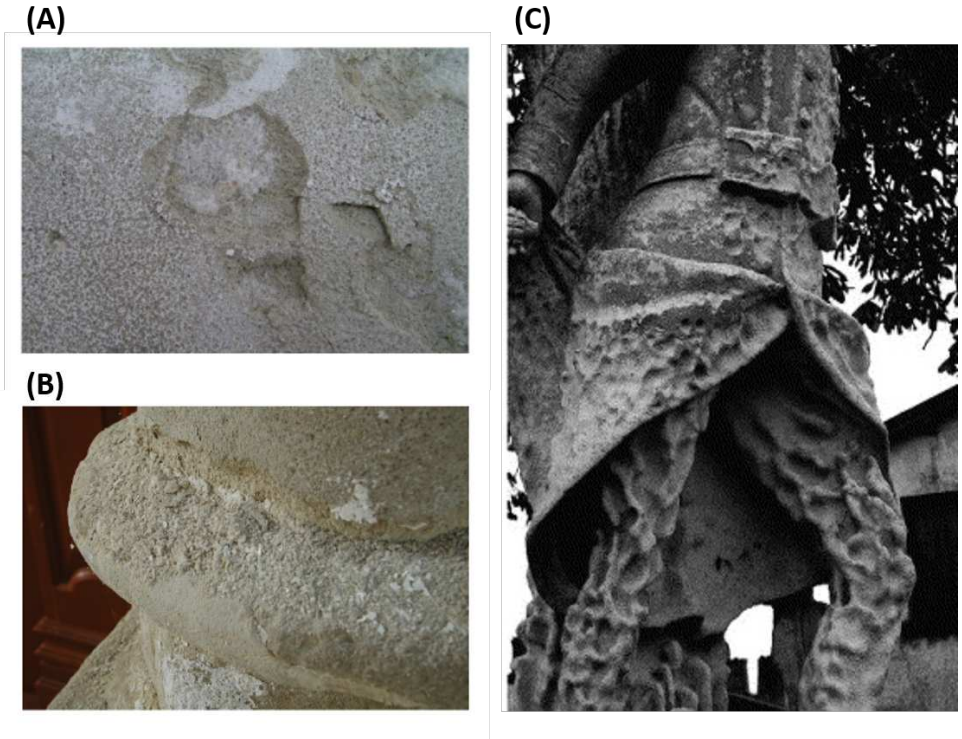

Figure 2: Salt subflorescence: scaling (A) and sanding (B) of the plaster (St. Nicholas church in Brouwershaven, The Netherlands) [38], (C) statue of a soldier in La Rochelle, France [50]

When discussing salt damage, a concept that is widely addressed in the literature is crystallization pressure. This concept was first introduced by Lavalle in 1853 [33], and since then, numerous authors have explored and examined the phenomenon of crystallization pressure [43], [13], [24]. A complete thermodynamical description was made by M.Steiger [57] where the crystallization pressure was presented as:

$$\delta P_i = \frac{RT}{V_m} ln \frac{a}{a_0} - \nu_{cl,i} \cdot \frac{dA_i}{dV} \tag{1}$$

Where δP$_i$ is the crystallization pressure in [Pa], R is the gas constant in [J/(mol·K], T is the absolute temperature in [K], V_m is the molar volume of the solid phase in [m³/mol], $\frac{a}{a_0}$ is the ration of the activity coefficient and the standard state activity coefficient, $\nu_{cl,i}$ is the surface free energy in [J/m²], dA_i is the area of surface created in [m^2], and dV is the volume transformed during growth at i^{th} crystal face, where i is the crystal face.
The foundation of this equation is based on the assumption that when a crystal is in contact with a supersaturated solution within a confined environment (a pore), it gives rise to stress. This stress can lead to damage within the pore when it surpasses the material's tensile strength.

To remediate the damage caused by salt crystallization, it is essential to comprehend the mechanisms underlying this damage in building materials and cultural heritage. Achieving this understanding requires the development of laboratory weathering protocols capable of accurately simulating field-related damage. In [25] the authors discussed the challenges and approaches to define relatable weathering protocols for salt damage in building materials. This work proposed a simple conceptual model for the development of salt damage, distinguishing between an "induction" phase and a "propagation" phase as shown in figure 3. The induction phase is characterized by salt transport and accumulation within the material, without immediately causing detectable damage. Accurate quantification of the rate of salt accumulation during this phase is crucial as it informs the selection of appropriate tests for assessing the long-term durability of building materials. Subsequently, the propagation phase is entered once a critical point, referred to as 'damage onset', is reached. In this phase, the material undergoes degradation and experiences a loss of structural strength. Tests that can initiate and propagate damage become necessary during this stage to determine a damage rate representative of real-world conditions, which in turn aids in evaluating the remaining service life of materials undergoing degradation.

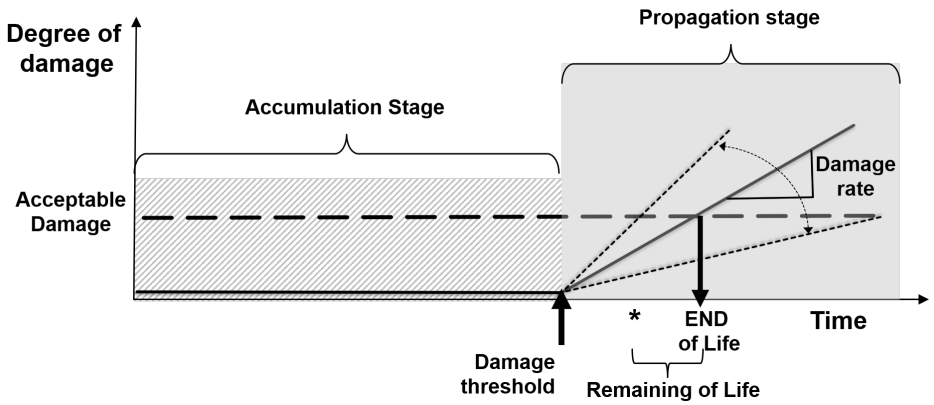

Figure 3: Schematic representation of the conceptual model [25]

In recent work by the RILEM TC [37], a weathering protocol was proposed for single porous materials using sodium chloride and sodium sulfate. This protocol recognizes the significance of a specific salt accumulation level required to initiate damage and characterizes salt-induced damage as a two-phase process based on the work of the authors in [25]. Two distinct weathering protocols were implemented for sodium chloride and sodium sulfate due to their differing properties, which we will present in chapter 1. The majority of salt weathering studies have focused on basic materials such as building stones and simple model porous materials [17, 19, 51, 50]. While understanding the phenomenon in simple materials is crucial, common cultural heritage materials are typically complex, often including multiple layers of different natures.

This thesis is a part of the broader European project CRYSTINART, which is a collaborative research effort initiated by Prof. N. Shahidzadeh at the University of Amsterdam and involves four universities: the University of Amsterdam (UvA), the University of Pau and Pays de l'Adour (UPPA), the University of Bologna (UNIBO), and the Technical University of Eindhoven (TU/e). The Rijksmuseum is also a partner in this project. The project commenced in September 2020 and is scheduled to conclude by February 2024. The primary objective of CRYSTINART is to enhance our comprehension of salt crystallization and mechanical damage in multilayered porous artworks, with a specific focus on unraveling the interplay between nano, micro, and macro-scale processes that govern internal crystallization phenomena and fluid dynamics. This is to be achieved through a dual-pronged approach: from an experimental perspective, guided by the work of the PhD student Rozeline Wijnhorst at UvA and TU/e, and the work of the PhD student Tinhinane Chekai at UPPA, alongside a numerical modeling approach led by UNIBO.

Several strategies have been proposed to protect our buildings from moisture. One such method involves the use of tin-glazed tiles on walls. These tiles, beyond their moisture-repelling properties, have often been recognized for their artistic contributions, to decorating cities worldwide. Examples include the Portuguese azulejos and Dutch tiles. While these structures effectively repel moisture infiltration into walls, they remain vulnerable to groundwater moisture, which not only transports soluble salts into the building but also causes damage to the tiles. Salt weathering in tiles is a widespread issue affecting these beautiful structures.

Another technique used to prevent moisture infiltration into buildings is the application of hydrophobic agents on wall facades. However, similar to tiles, these treated surfaces are susceptible to the damaging effects of soluble salts transported by groundwater, introducing additional complexity to our understanding of this issue.

Rozeline Wijnhorst, PhD student at UvA, and Tinhinane Chekai, PhD student at UPPA, conducted parallel investigations into those selected subjects of study. Both students explored salt accumulation and damage via a designed weathering protocol involving tin-glazed Dutch tiles, employing sodium chloride and sodium sulfate, but employing different methodologies. Rozeline Wijnhorst conducted her research using SEM, SEM-EDX, and profilometer techniques, while Tinhinane Chekai utilized 3D X-ray computed tomography to investigate these aspects. Another collaborative study focused on sintered glass beads porous media. Rozeline Wijnhorst examined 2D samples consisting of a single layer of glass beads packed inside a rectangular capillary, which were subsequently sintered. Tinhinane Chekai, on the other hand, worked with 3D samples composed of glass beads of the same size where 4D X-ray tomography was used to study the drying kinetics and the crystallization patterns of sodium chloride and sodium sulfate. In both 2D and 3D samples, one-third of their volume was made hydrophobic. The aim of these studies was to investigate crystallization in these sample types using two salts, sodium chloride and sodium sulfate, and to explore the impact of wettability on drying kinetics and crystallization patterns in the two types of samples. The UNIBO team, meanwhile, focused on developing and implementing multiscale numerical models for predicting damage due to salt crystallization. Their work involves the development of macro-scale and micro-mechanical models, as well as the study of micro-macro interactions. The experimental results obtained at UvA and UPPA serve as validation and input data for the UNIBO team's modelling efforts.

The thesis manuscript starts with Chapter 1 where a comprehensive review of the current state of knowledge is made regarding sodium chloride and sodium sulfate properties, salt crystallization damage in tin-glazed tiles, and crystallization in glass beads packing.
Chapter 2 represents notions of porous media and characterization methods used in this thesis.
Chapter 3 is dedicated to the study conducted on tin-glazed tiles, providing structural, hygric, and mechanical characterizations of Dutch tiles. The chapter also investigates salt weathering of these structures using X-ray tomography and scanning electron microscopy (SEM) imaging.
Chapter 4 investigates the subsequent experimental part, concentrating on the study of salt and moisture transport, alongside salt accumulation, in an artificial porous media characterized by two distinct wettabilities. Within this chapter, 4D X-ray computed tomography is used to observe in situ salt crystallization and drying of the artificial porous media when saturated with a salt solution. The emphasis here lies in comprehending the overall drying behaviour and accumulation trends derived from both qualitative and quantitative analyses of the X-ray CT images.
Continuing from Chapter 4, Chapter 5 provides a more in-depth analysis of the results, focusing on pore-scale investigations. The objective is to study the interrelations between evaporation, precipitation, wettability, and pore size, during drying-precipitation events. This chapter seeks to derive precise quantitative data from image analysis at the pore scale.
In the final chapter of the manuscript, a comparative analysis between the two primary experimental studies is made, followed by a restatement of the objectives outlined at the beginning of this thesis. This concluding section is succeeded by an exploration of potential future studies that can build upon the foundations established within this thesis.

Chapter 1

State of the art

In this chapter, we delve into relevant literature related to this thesis. First, we introduce the salts of interest, outlining their properties and their induced damage. Then, we present relevant literature on tin-glazed tiles. Following that, we present literature related to salt crystallization in glass beads packed porous media and the influence of wettability on crystallization.

Contents

1.1 Salts of interest

Salt precipitation takes place when two soluble substances come into contact and chemically react, resulting in the formation of a solid structure with a well-organized and consistent pattern known as a crystalline structure. The phase transformation governing the balance between solute and solvent during the process of crystallization relies on both concentration and temperature. The ionic components gradually transition from the stable dissolved state, where crystallization is not possible, to a state where spontaneous crystallization becomes possible. This transition passes through an intermediate phase where the solution reaches saturation. Although it does not reach a critical state of supersaturation, it allows for gradual crystal growth. The hygroscopicity of a salt refers to its ability to adsorb water molecules and form hydrogen bonds on its surface. When the atmosphere provides sufficient moisture, a deliquescence phenomenon occurs. The relative humidity at which the salt transforms into a solution or adopts a more hydrated form is defined as the equilibrium relative humidity. If the actual relative humidity is less than the equilibrium relative humidity, the salt remains in a solid or less hydrated state; if actual relative humidity is greater than the equilibrium relative humidity, the salt dissolves or adopts a higher hydration state. The hygroscopicity of the salt is greater when its equilibrium relative humidity is low and its solubility is high. Pressure and temperature affect solubility and also influence the equilibrium relative humidity [58, 12].In this next part we will present two salts that are chosen to work with in this thesis. The two salt sodium chloride and sodium sulfate were chosen based on their common encounter in the field of building materials and cultural heritage when it comes to salt weathering [35, 52].

1.1.1 Sodium chloride

Sodium chloride, commonly referred to as table salt, plays a substantial role in the weathering and degradation of porous building materials. Above 0°C, sodium chloride forms an anhydrous phase called halite. The solubility of the anhydrous phase, characterized by a cubic crystalline structure, exhibits a relatively constant trend with temperature, as illustrated in Figure 1.1. Additionally, its equilibrium relative humidity fluctuates around 75%, as depicted in Figure 1.2, which represents the threshold at which NaCl crystals can dissolve, leading to the formation of a solution i.e. a phenomenon known as deliquescence. Deliquescence cycling of sodium chloride is recognized as damaging to porous materials [35, 19] and has been utilized as a method for inducing damage in artificial weathering protocols [37].

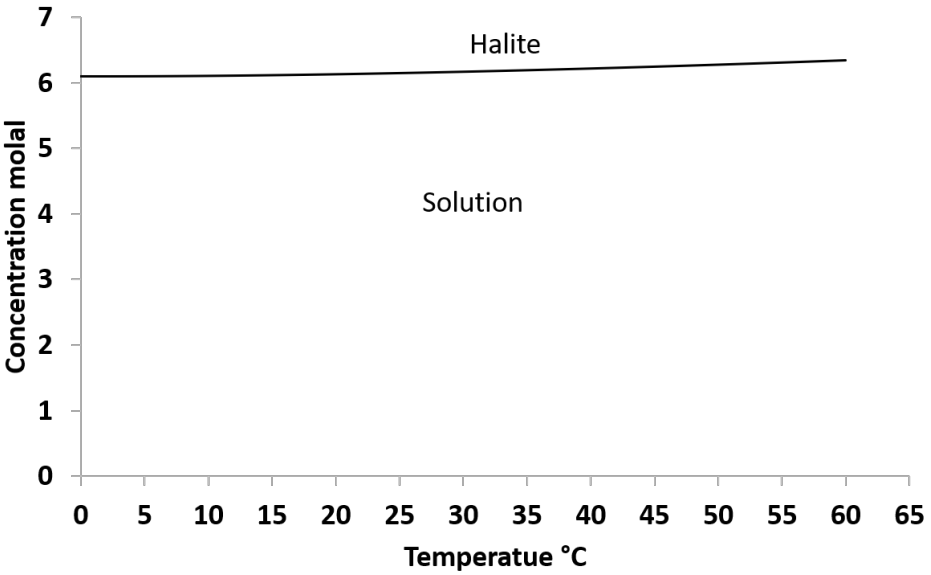

Figure 1.1: Solubility diagram of sodium chloride [17]

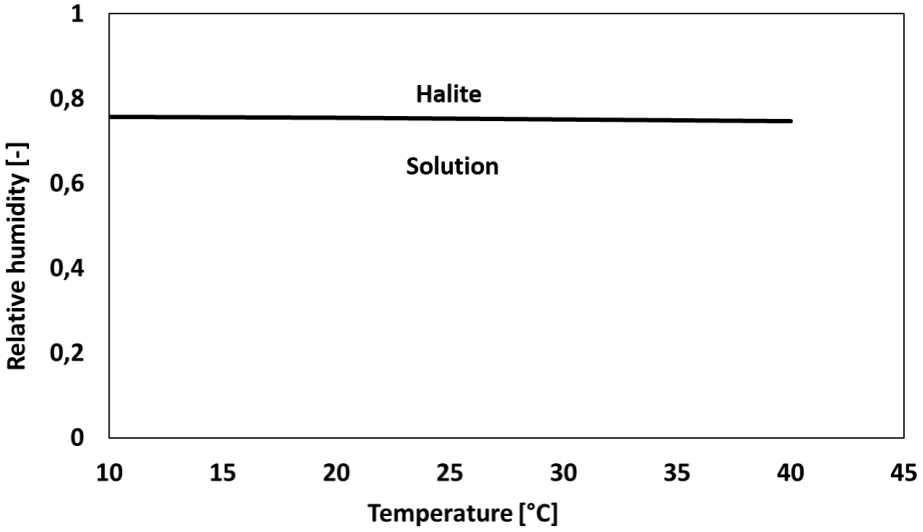

Figure 1.2: Phase diagram of sodium chloride [12]

1.1.2 Sodium sulfate

Sodium sulfate is a chemically complex salt with multiple anhydrous forms, including thénardite and a metastable Phase III. It also has hydrated forms, such as the stable decahydrate (mirabilite) below 32.4°C, and the metastable heptahydrate below 24°C as shown in figure 1.3. Unlike sodium chloride, sodium sulfate temperature has a great effect on its solubility and on its phases equilibrium relative humidity. Focusing solely on stable phases, the damaging effect of sodium sulfate is attributed to the supersaturation of the solution with respect to mirabilite through the dissolution of thenardite [51]. This property is used to design weathering protocols [37].

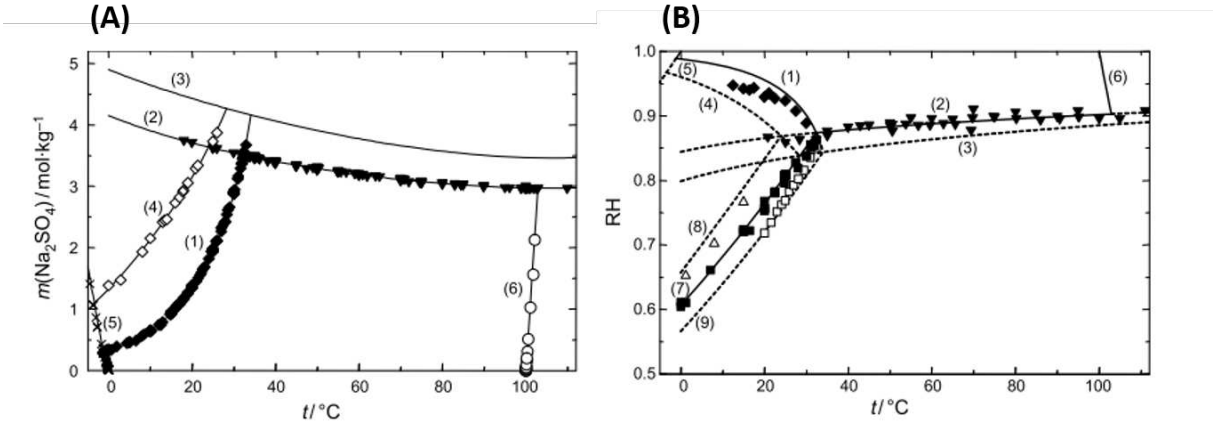

Figure 1.3: (A) solubility diagram of sodium sulfate, and (B) phase diagram of sodium sulfate: (1) Na2SO4·10H2O (mirabilite), (2) Na2SO4(V) (thenardite), (3) Na2SO4(III), (4) Na2SO4·7H2O, freezing temperatures (5) and boiling temperatures (6). [59]

1.2 Salt crystallization in tin-glazed tiles

Dutch ceramic tiles, cherished for their historical and cultural significance, have gathered limited attention within the academic literature. Adding to that, there has been limited research dedicated to the study of degradation processes, particularly related to salt crystallization. Most academic efforts have predominantly revolved around the determination of the composition and historical contexts of these tiles [8]. While studies have investigated biological degradation and degradation in Portuguese tiles due to salt crystallization, there is a significant lack of comprehensive research on salt degradation mechanisms specific to Dutch tiles.

While earlier research on Dutch tiles did not explicitly investigate the impact of salt crystallization, it did offer valuable insights into field damage and potential contributing factors affecting these tiles. K.van Lookeren Campagne [6], used archival sources to understand the production techniques and problems faced in the 17^{th} and the 18^{th} century. The aim of this study was to derive information that will aid in the interpretation of chemical and material analysis, possibly placing issues of susceptibility to deterioration within a clearer historical context. It was cited that the deterioration of these historic tiles is generally a result of a combination of environmental factors like exposure to moisture, temperature fluctuations, and pollutants in the air and problems intrinsic to the tiles themselves including issues with the glaze, such as cracking or crazing, as well as problems with the clay composition. In this work it was also noted that the Dutch tiles were exported all over the globe, making the deterioration of this structure a worldwide issue that needs to be addressed.

In terms of salt degradation in Dutch tiles, K.van Lookeren Campagne [7] has discussed the influence of the climatic conditions and the significance of the production process on deterioration mechanisms of 17^{th} century Dutch tiles. In the same study, the author stated that salt damage is a major factor in the deterioration of tin-glazed tiles as shown in figure 1.1, and that the damaging salts are transported into the porous ceramic body with water. The influence of the climatic conditions was also put forward where it was discussed that when the humidity levels fall below the point of deliquescence of a particular salt, the salt crystallizes and causes damage. This damage is usually manifesting in pushing away the glaze and the ceramic material from the surface. A comparison was also made between Dutch tiles and Portuguese tiles in terms of damage, where it is stated that the clay composition plays a role in the glaze loss problem. The Dutch tiles show variations in the chemical composition of their clay body, with some clay bodies being more iron-rich and others more calcium-rich. On the other hand, the Portuguese tiles have a red, iron-rich/low-calcium clay composition. The Dutch tiles show glaze loss and poor glaze attachment, while the Portuguese tiles have suffered from damage to the ceramic body itself. An experimental study of Portuguese tiles with poor glaze adhesion has also suggested that high calcium content in the ceramic body is related to the problem of glaze detachment.

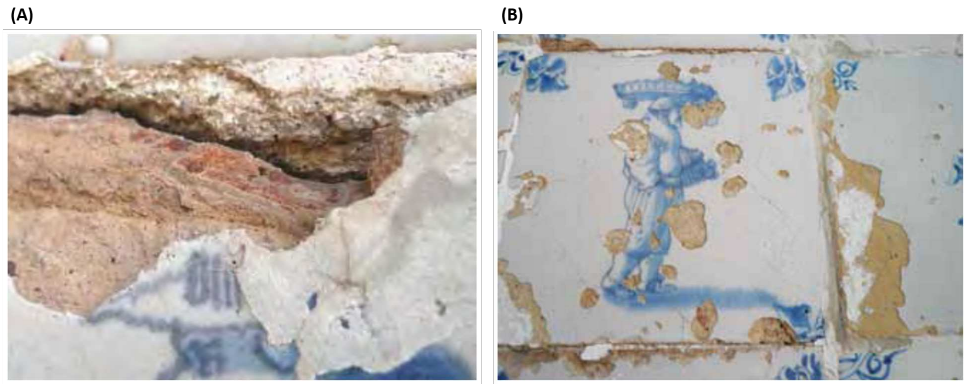

Figure 1.4: Dutch tiles: (A) Salt damage resulting in the delamination of a ceramic body, (B) An example of salt damage resulting in 'shivering' of the glaze [7]

Existing literature has extensively addressed the characterization of Portuguese tiles and the investigation of salt-induced degradation. Notably, Mimoso's work [40] delves into various aspects, including the interface between glaze and clay body, characteristics of the decay process, detection of weak points, and proposes solutions for preserving Portuguese tiles. A recurring observation in numerous Portuguese monuments is that salt crystallization plays a significant role in the decay patterns of azulejos. Furthermore, moisture, combined with salt crystallization, has been identified as a leading cause of decay in these tiles. An additional key insight is the critical importance of studying the interface between the glaze and the clay body, as weak points in this region can lead to water penetration and glaze detachment. It's worth noting that the decay of tiles doesn't uniformly affect all tiles; it typically initiates at weak points, which may be absent in some tiles. The physical and chemical properties of these tiles were also studied in detail by Pereira [46]. This study focused on the physical, chemical, and mineralogical characterization of historical Portuguese azulejos from the 17th to the early 19th century. Various physical properties were examined, encompassing the pore structure of the ceramic body using mercury intrusion porosimetry (MIP), the specific surface area through the BET method, water absorption curves through capillary water uptake, and the thermal and moisture expansion coefficients determined via dilatometry. These investigations aimed to provide a comprehensive understanding of the composition, behaviour, and degradation mechanisms of these tiles. To investigate salt-induced degradation of these tiles, a study by L.Esteves [23] focused on artificial ageing using sodium chloride and decay of azulejos. The samples used in the study were presumed to be from the Lisbon workshops and exhibited various degrees of decay. Each azulejo sample was divided into three separate test items, each representing distinct types of tile degradation.

To establish consistent and reproducible conditions for the ageing procedures, an initial desalination process was conducted using pure water on all the tested samples. After the desalination procedure, the samples were meticulously labelled and utilized as follows: one set underwent accelerated ageing cycles, another was exposed to wetting without saline contamination, and the third served as a reference control group. Scanning Electron Microscopy (SEM) images were employed to identify pre-existing weaknesses in the tiles and correlate them with glaze loss observed during the ageing tests. Prior to the ageing test, an initial testing cycle aimed to release any damaged glaze parts. This cycle began with saturating the samples in a 330g/l NaCl solution for 7 days, followed by a 7-day drying period at 60°C. Subsequently, the samples underwent a 7-day desalination phase. Following this preliminary step, the samples underwent 5 sets of 15 wetting and drying cycles. In the first cycle of each set, the clay body faced upward, and a 20% volume of the saturated salt solution required to reach capillary saturation was introduced into each sample's clay body. Afterwards, the samples underwent a 7-day drying period. In the subsequent 14 cycles of each set, the samples were contaminated with 20% of the volume required to reach capillary saturation but this time with pure water. The drying phase followed, lasting 7 days at 60°C. The entire ageing test extended over a duration of 17 months and 29 days. During drying, the samples were sealed in airtight plastic containers, as illustrated in figure 1.5. These containers held the test items in place, with exposed edges left open to mimic joint spaces, and epoxy paste sealed the sides. Following the completion of the 5 series, an additional 5-week desalination process was carried out. The ageing tests resulted in the loss of glaze in several samples, and some samples experienced clay body fractures during the ageing process. It is noteworthy that samples initially displaying significant degradation exhibited more pronounced degradation during the ageing test. Conversely, samples with no apparent major initial degradation suffered the least damage throughout the ageing test.

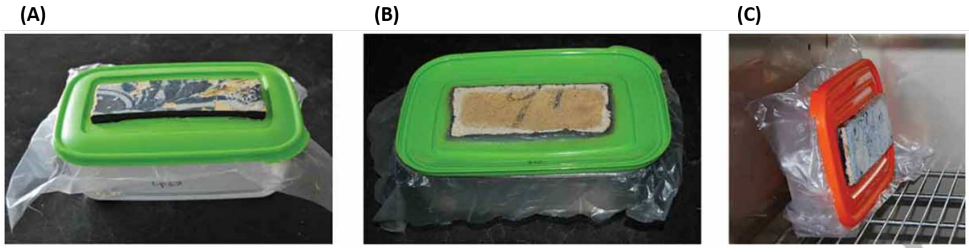

Figure 1.5: Experiment setup: (A) setup tile + plastic box, (B) wetting procedure for the wetting cycle with 20% of the capillary saturation volume, (C) drying inside the oven showing the position of the setup tile + plastic box [46]

In light of these findings, several unanswered questions and potential research perspectives have been raised. Addressing these unanswered questions and exploring potential research perspectives will provide valuable insights into the understanding of salt-induced damage in tiles. This thesis aims to address some of the gaps that persist in the current body of research. While previous studies predominantly focused on the impact of sodium chloride, our research extends its scope to encompass the influence of sodium sulfate. Moreover, in contrast to the lengthy ageing test proposed in prior work, we introduced a faster ageing test to induce damage in the Dutch tiles. Most notably, the majority of samples in previous studies already exhibited some form of decay prior to testing. In our investigation, we explore a broader spectrum of samples, including those in pristine condition with no observable macroscopic decay, as well as those displaying one specific type of decay that is crazing.

Furthermore, our research takes into account the absence of 3D analyses of salt accumulation patterns and salt damage in tin-glazed tiles, which we address by employing X-ray computed tomography (CT) to provide a comprehensive perspective on the subject.

1.3 Salt crystallization in glass beads packs with different wettability

The prediction of damages induced by salt crystallization in porous materials requires an understanding of the evaporation rate and the evolution of liquid distribution within the pore space [54]. Various factors, such as environmental conditions, wettability of the porous materials, and the presence of salt, influence the drying pattern and its associated phenomena [47], [10].

The occurrence and morphology of efflorescence and subflorescence depend on various factors, including wetting behaviour, interfacial properties, and concentration gradients. In the study conducted by N. Shahidzadeh [56], the research delves into the evaporation dynamics of saturated sodium chloride and sodium sulfate solution droplets on both hydrophobic and hydrophilic surfaces, as well as the evaporation of saturated solutions within hydrophilic square capillaries. The investigation explores resulting crystallization patterns, providing insights into how wetting properties influence the crystal formation process. The findings indicate that sodium chloride crystals tend to form in contact with air or hydrophobic medium, a phenomenon that could counteract conservation efforts when utilizing hydrophobic treatment to prevent salt accumulation for this specific salt. In hydrophilic capillaries, it was observed that hydrated crystals of sodium sulfate tend to form as subflorescence, whereas anhydrous crystals manifest as efflorescence. However, regardless of the salt phase, if the wetting film extends toward the surface, efflorescence occurs for both salts i.e. sodium chloride and sodium sulfate.

In the study conducted by N. Sghaier [54], two systems of two-dimensional artificial porous media were developed. The first system consisted of a hydrophilic layer of glass beads enclosed between two hydrophilic glass plates, while the second system involved hydrophobic glass beads encased between two hydrophobic glass plates. Both systems were fully saturated with an almost saturated NaCl solution and subjected to drying from all four sides under controlled conditions of 22°C and 12% relative humidity, achieved using a LiCl saturated solution, as depicted in Figure 1.6. The system's weight was continuously monitored using a balance, and its evolution was tracked with a CCD camera positioned above the system, as shown in Figure 1.7.

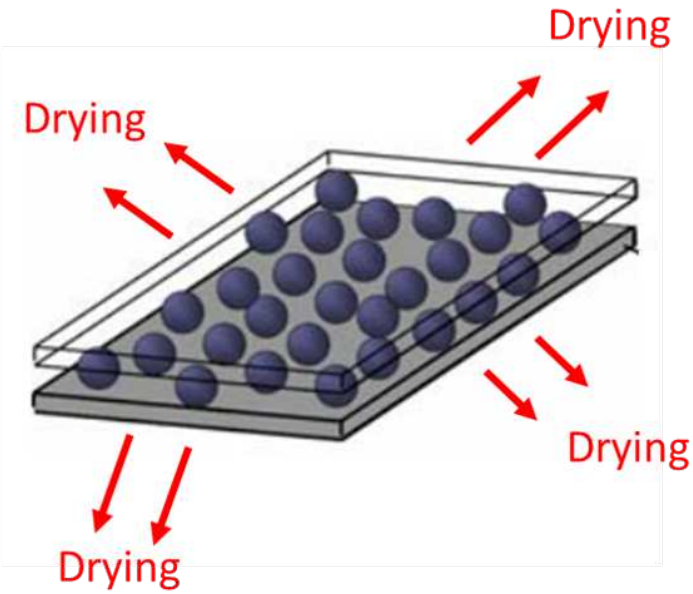

Figure 1.6: Artificial porous media, showing the drying surfaces and the setup glass beads + glass plates [54]

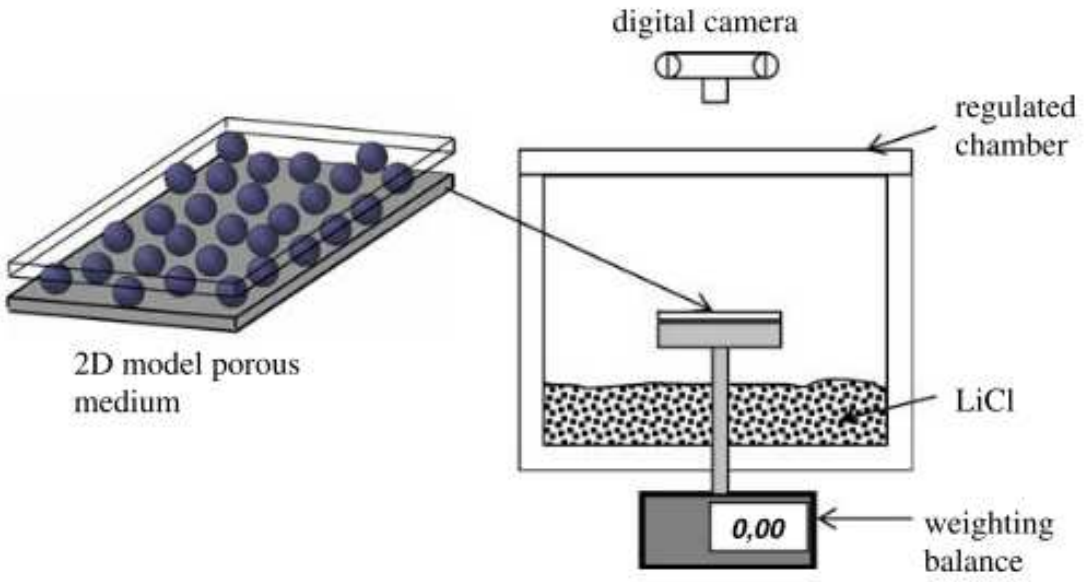

Figure 1.7: Drying experimental setup[54]

The authors investigated the influence of wettability and the presence of salt on drying patterns and analyzed the transport processes and growth mechanisms involved in the formation of salt structures. Observations of the drying process in hydrophilic and hydrophobic systems reveal distinct patterns in the presence of sodium chloride. In the hydrophilic medium, the drying process is characterized by capillary fingerings and trapped liquid clusters, which are typical of invasion percolation patterns as shown in figure 1.8(B). The drying kinetics in the hydrophilic medium were characterized by a first period of faster evaporation, followed by a slower evaporation period. The evaporation rate remains significant throughout the drying process. On the other hand, in the hydrophobic medium, the invasion pattern is much more compact with no fingering as shown in figure 1.8(A). The drying kinetics were characterized by a first period of rapid evaporation, followed by an extremely slow evaporation period. The evaporation rate is significantly smaller than in the first period and remains almost zero during the slow evaporation period.

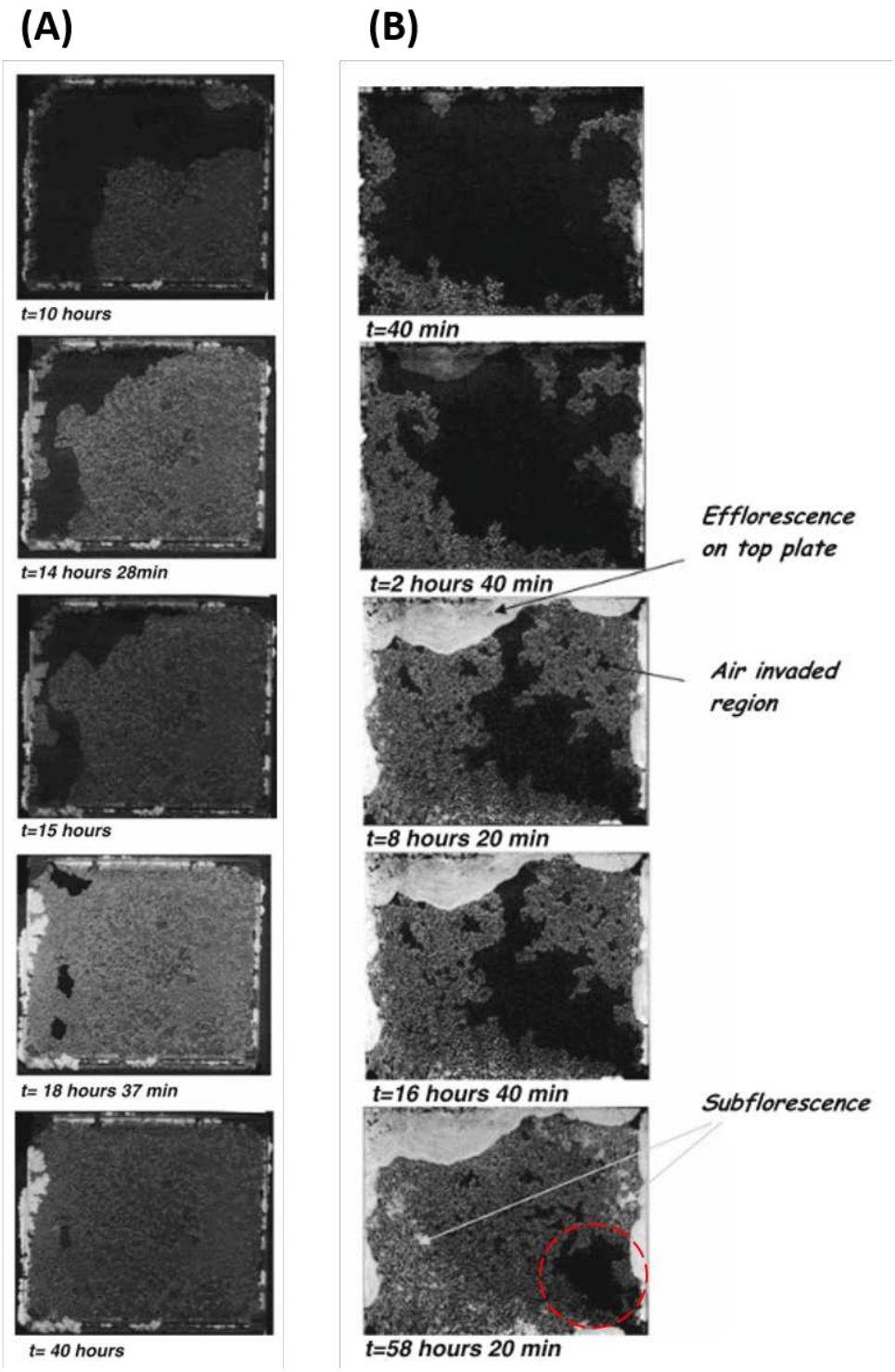

Figure 1.8: CCD camera results showing the drying of two systems where the white represents the NaCl accumulation, and the black represents the solution saturated regions: (A) the drying of the hydrophobic system, (B) the drying of the hydrophilic system [54]

The authors in [54] also investigated efflorescence formation and its impact on the drying kinetics of porous media due to the presence of dissolved NaCl. Efflorescence formation was observed during drying in both hydrophilic and hydrophobic media. However, the mechanisms underlying efflorescence formation differ between the two. In the hydrophilic medium, liquid films create pathways for salt transport, while in the hydrophobic medium, efflorescence is directly associated with a trapped liquid cluster. The drying process with efflorescence formation can be divided into three main periods: an initial pre-crystallization period, a subsequent stage marked by efflorescence growth and liquid capillary pumping, and a final period where the efflorescence dries out, acting as a resistance to diffusive transport. Initially, efflorescence formation enhances the evaporation rate due to its liquid capillary pumping effect. However, it later functions as a barrier to vapour diffusion, resulting in a reduced evaporation rate. Subflorescence was also observed, influencing the drying process in both hydrophobic and hydrophilic media. In the hydrophobic medium, subflorescence was directly related to a trapped liquid cluster, causing a zero drying rate. Conversely, in the hydrophilic medium, subflorescence did not involve a liquid cluster, leading to a slower drying process without a zero drying rate.

While the impact of sodium chloride on drying kinetics and salt accumulation under varying wettability conditions has been examined in the literature, the influence of both sodium sulfate and sodium chloride in bi-layered porous media with two distinct wettabilities remains an under explored area. In this thesis, we embark on an investigation of bi-layered porous media. Notably, our utilization of 4D X-ray tomography methodology enables us to attain time-resolved 3D insights into the effects of salt formation on drying kinetics as well as the effect of the assembled wettabilities on salt crystallization for both salts, sodium chloride and sodium sulfate.

Chapter 2

Notions on porous media and characterization methods

In this chapter, we delineated the fundamental properties of porous media that serve as the foundation for the subsequent chapters. Additionally, we provided an overview of the experimental methods employed to characterize the materials utilized throughout this thesis and the experimental setups used to create conditioned environments for salt weathering tests.

Contents

2.1 Definitions

2.1.1 Porous media

One way to define a porous media is to refer to materials characterized by a network of interconnected voids or pores, enabling the passage or storage of fluids or other substances within its structure. These voids allow for the transport, filtration, absorption, or adsorption of substances through the material, making porous media a crucial element in various scientific, engineering, and environmental applications [4].

2.1.1.1 Porosity

The porosity of a material is defined as the ratio of the void volume to the total volume of the material and is expressed by the equation 2.1. Figure 2.1 illustrates a schematic representation of a porous media displaying both the void and the grain structure.

$$\phi = \frac{V_{void}}{V_{ap}} \tag{2.1}$$

Where ϕ is the porosity, V_{void} is the volume of the void, and V_{ap} is the total volume of the material.

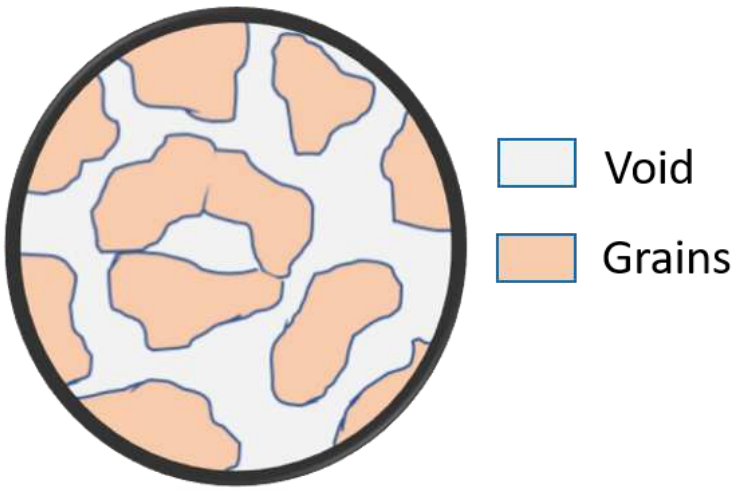

Figure 2.1: Schematic representation of a porous media showing the void and the grain structure

2.1.1.2 Saturation degree

In this thesis work, the porosity could be filled by 3 volume phases: brine, air, and salt. Saturation degree is defined as the ratio of the volume of the phase to the volume of the void as shown in figure 2.2, expressed by equation 2.2:

$$S_{phase} = \frac{V_{phase}}{V_{void}} \tag{2.2}$$

Where S_{phase} is the saturation degree of the phase, V_{phase} is the volume of the phase in $[m^3]$ and V_{void} is the volume of the connected pore space.
Where:

$$S_{salt} + S_{air} + S_{brine} = 1 \tag{2.3}$$

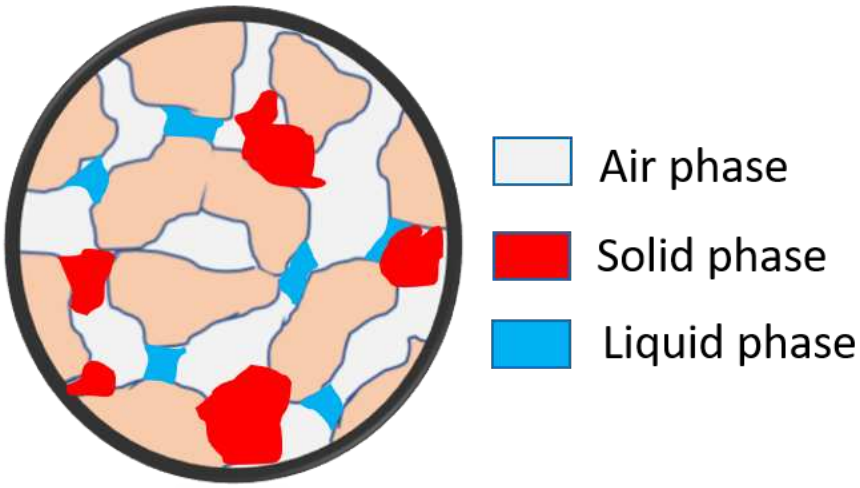

Figure 2.2: Schematic representation of the contained phases in the porous media

2.1.1.3 Capillarity

Capillary action in a pore filled with both water and air is driven by cohesive forces among water molecules, reduced cohesion upon interaction with air, and adhesive forces between water and air molecules and the pore wall. When a water meniscus makes contact with a pore wall, and the adhesion to the wall surpasses the attraction to air, the meniscus moves upward along the wall at an angle (ϑ) between 0 and 90°, known as the contact angle (figure 2.3A). This phenomenon is typical of hydrophilic materials. Conversely, if the adhesion to the wall is weaker than the attraction to air, the meniscus is repelled, resulting in a contact angle between 90 and 180° [28] (figure 2.3B).

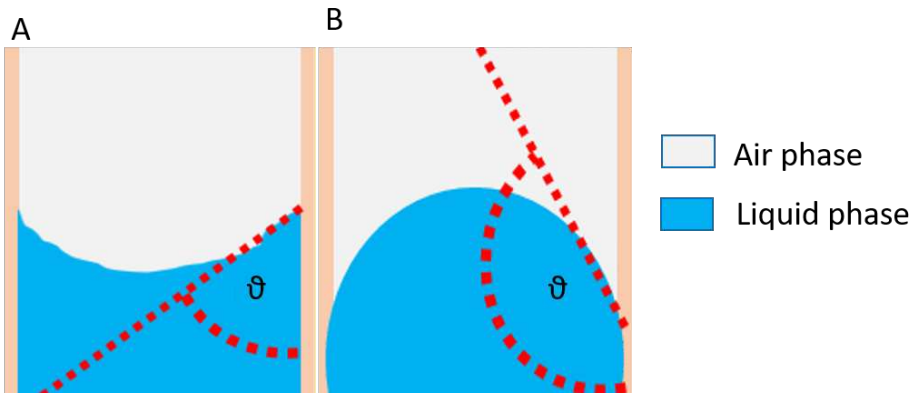

Figure 2.3: Schematic representation of contact of water and a pore wall

2.1.2 Environmental conditions

Temperature and relative humidity play a significant role in the damage caused by the presence of salts in porous materials. Changes in these factors affect the salt state (crystallization or deliquescence) and lead to deterioration. The presented experimental work was always carried out under isothermal conditions. In this section, we specifically investigate relative humidity related properties.

The ambient atmosphere is characterized by its moisture content, constituting a blend of dry air and water vapour. Given the absence of any chemical reactions between the dry air and water vapour, the air pressure can be accurately represented using Dalton's law, which states that the total pressure exerted by the mixture is the sum of the partial pressures of its individual components. Consequently, the air pressure can be expressed mathematically as follows in equation 2.4:

$$P_a = p_{da} + p_v \tag{2.4}$$

Where P_a is the air pressure in [Pa], p_{da} is the dry air pressure in [Pa], and p_v is the water vapour pressure in [Pa].

By making the assumption that both water vapour and dry air exhibit ideal gas behaviour [28], they adhere to the principles of the ideal gas law, which can be articulated as follows:

$$\rho_{da} = \frac{m_{da}}{V} = \frac{p_{da}}{R_{da}T} \tag{2.5}$$

Where ρ_{da} is the dry air density in [kg/m^3], m_{da} is the mass of the dry air in [kg], V is the total volume in [m^3], R_{da} is the gas constant for dry air (287.055 [J/kg.K] [28]); and

$$\rho_v = \frac{m_v}{V} = \frac{p_v}{R_v T} \tag{2.6}$$

Where ρ_v is the water vapour density in [kg/m^3], m_v is the mass of the water vapour in [kg], V is the total volume in [m^3], R_v is the gas constant for water vapour (461.52 [J/kg.K] [28]).
The saturated vapour density represents the maximum mass of water vapour that could be stored in a volume of air at a given air temperature. It is given by $\rho_{v,sat}$:

$$\rho_{v,sat} = \frac{m_{vsat}}{V} \tag{2.7}$$

Where m_{vsat} is the maximum mass of the vapour in the air in [kg] and V is the air volume. From the ideal gas law we have :

$$\rho_{vsat} = \frac{m_{vsat}}{V} = \frac{p_{vsat}}{R_v T} \tag{2.8}$$

(p_{sat}) is the saturated vapour pressure, and it can be represented by the following relationship [28]:

$$p_{sat} = 611. \exp \frac{17,08.\theta}{234,18 + \theta} \tag{2.9}$$

Where θ is the temperature in [C°]. Since the saturated vapour pressure represents the maximum vapour achievable in equilibrium, comparing it to the actual vapour pressure gives rise to the concept of relative humidity (RH). This can be expressed as follows: [28]

$$RH = 100\frac{\rho_v}{\rho_{v,sat}} = 100\frac{p_v}{p_{sat}} \tag{2.10}$$

Where $\rho_{v,sat}$ is the saturated vapour density. When we plot the saturated vapour pressure in function of the temperature, this later increases with the increase of the temperature. The corresponding curve is shown in figure 2.4.

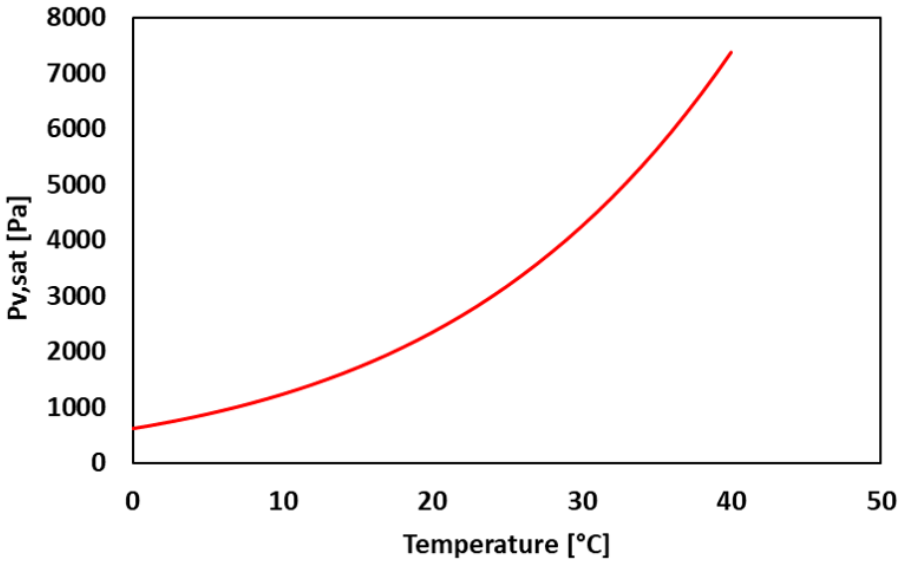

Figure 2.4: Variation of the saturated vapour pressure in function of the air temperature

2.2 Experimental methods

2.2.1 Characterization of the porous media

2.2.1.1 Tile samples preparation

The original tiles measure 15 x 15 cm. For the purposes of the experiments, glazed and unglazed samples were obtained from the original tiles. The tiles were first cut with a 2 mm thick saw into 2 x 2 cm or 6 x 6 cm square samples. The tiles were cut in the presence of water. The required samples were then polished to remove the glaze using a polishing machine with polishing characteristics of 100 µm.

2.2.1.2 Porosity and density characterization

Within this thesis, we employed the Archimedes density and porosity characterization method to assess the porosity and density of the samples adhering to the European standard EN ISO 10545-3 [31]. The process for determining density and porosity through the application of the Archimedes principle is elaborated below:

$$\rho_d = \frac{m_d}{V_d} \tag{2.11}$$

$$\phi = \frac{V_v}{V_{ap}} \tag{2.12}$$

Where ρ_d is the density of the sample in [kg/m^3], m_d is the dry weight of the sample in [kg] and V_d is the volume of the solid including only the solid part in the sample in [m^3]. ϕ is the porosity, V_v is the volume of the pore space in [m^3], and V_{ap} is the volume of the sample including the solid part in the sample and the pore space in [m^3]. The volume of the pore space is defined as :

$$V_v = \frac{m_{sat} - m_d}{\rho_w} \tag{2.13}$$

Where m_{sat} is the saturated mass of the sample in [kg] and ρ_w is the density of pure water in [kg/m^3]. The unknowns are the volume of the solid and the total volume of the sample where :

$$V_{ap} = V_v + V_d \tag{2.14}$$

Here we have 2 unknowns and only one equation, in this case, we need a second equation. That is when we use the Archimedes principle in order to solve our system of equations. When a body is immersed in fluid, it is buoyed up by a force equal to the weight of the fluid displaced. In this case :

$$\rho_w.V_d.g = m_d.g - m_h.g \tag{2.15}$$

Where g is the gravitational acceleration in [m/s^2] In the end, we get :

$$V_d = \frac{m_d - m_h}{\rho_w} \tag{2.16}$$

Where m_h is the measured mass of the sample when immersed in the pure water.

The experimental procedure is defined as follows: initially, the sample was subjected to a 24-hour drying process in an oven set at a constant temperature of 60°C. Upon completion of the drying procedure, the dry weight of the sample (m_d) was taken. Following the determination of the dry weight, the next step involved evacuating the air from the sample. This was achieved using a vacuum for 2h at 20 kPa. Subsequently, pure water was introduced into the vacuum environment. After completely covering the sample with pure water (a period of 15 min), the atmospheric pressure was restored allowing the sample to saturate for a period of 24 hours. Upon achieving full saturation, we conducted measurements to determine both the Archimedes' weight and the saturated weight of the samples. These measurements were carried out using a Mettler Toledo XRE205 DeltaRange balance with an accuracy of d=0.01 mg for masses below 81g. This balance is equipped to conduct this kind of measurement as shown in figure 2.5. Subsequently, we utilized these measurements to calculate the porosity and density of the sample. In our experiments, after 24 hours of saturation at atmospheric pressure, we measured the mass of the samples. Subsequently, an additional 24 hours of saturation were applied to the samples under atmospheric pressure. The weight of the samples remained stable after the additional 24 hours, indicating full saturation.

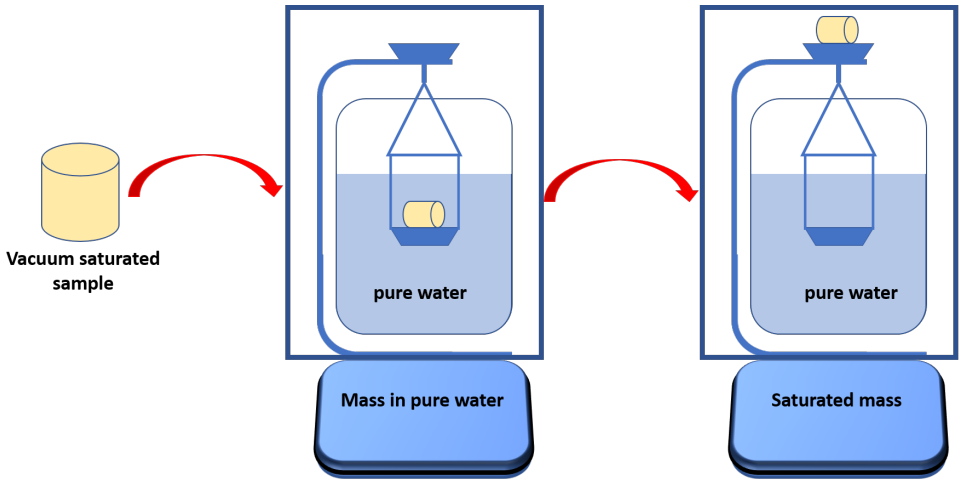

Figure 2.5: Archimedes density characterization

2.2.1.3 Pore size distribution characterization

Pore size distribution analysis was conducted through mercury intrusion porosimetry (MIP). The instrument employed for this purpose was the AutoPore IV unit. The interpretation of the Mercury Intrusion Porosimetry (MIP) measurements is grounded in an idealized view of the porous network. This network is envisioned as an assembly of cylindrical pores with varying diameters. The Laplace equation (also known as the Washburn equation) shown in equation 2.17 establishes a connection between the capillary pressure (P_c) of mercury and the radius of the pore (r) that it succeeds in filling. In this equation, γ = 0.485 N/m represents the surface tension of mercury in a vacuum, ϑ = 130° is the contact angle, and r denotes the pore radius. The distribution of pore sizes is then derived from the volume of mercury injected at a specific pressure.

$$P_c = \frac{2.\gamma.cos(\theta)}{r} \tag{2.17}$$

For the procedure, in the first stage, it is imperative that the sample is thoroughly dried. Following this, the sample is placed within the penetrometer and subjected to a vacuum to eliminate any air bubbles. Subsequently, the penetrometer is filled with mercury, and the injection pressure is incrementally increased in discrete steps. For low pressures, air pressure is employed to force mercury into the material, while for higher pressures, oil pressure is utilized for this purpose. As the injection pressure progressively rises, the mercury infiltrates increasingly finer pores within the sample. The volume of mercury injected into the material is measured at each pressure step after stabilization. For a given injection pressure (P_c), it is assumed that at the point of stabilization, all pores with a radius larger than r, where r = -2γcosϑ/P_c, are saturated with mercury. Injection pressures can range from a few bars to 4136 bars, thereby providing access to a spectrum of pore diameters ranging from 400 µm to 3 nm. The results of mercury porosimetry tests provide us with the volume of mercury infiltrated into the sample in relation to the applied pressure. Typically, the software outputs the mercury volume per unit mass of the material (mL/g). Upon completion of the injection steps, the test can be supplemented by a mercury extraction phase, involving pressure reduction steps until atmospheric pressure is reached. It is worth noting that the injection-extraction cycle of mercury porosimetry is generally not reversible, and a quantity of mercury often remains trapped within the sample at the end of the extraction process.

2.2.1.4 Compressive strength and elastic properties

The evaluation of the compressive strength of the tiles used in chapter 3 was carried out referring to the NF EN ISO 10545-4 [41] standard for ceramic tiles. A Zwick Z020 electromeca press machine with a capacity of 20kN was used. A downward displacement rate of 0.1 mm/s was applied until the maximum compressive strength was attained.

The elastic properties of the tiles were evaluated using the ultrasonic pulse velocity (UPV) technique. This method is based on the measurement of compressive and shear wave travel times through the clay body. The apparatus measures the travel time of two waves: the shear wave and the compressive wave. These waves are emitted from the transmitter, travel through the thickness of the sample, and are then received by the receiver. The time interval between the emission and reception of the waves is measured.

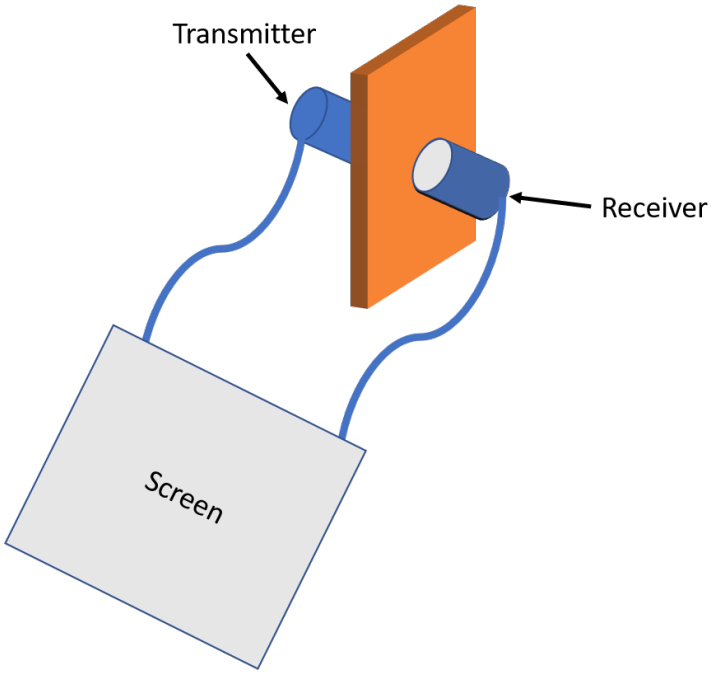

Figure 2.6: Schematic figure showing the principle of ultrasonic pulse velocity

2.2.1.5 3D and 4D X-ray computed tomography

X-ray computed tomography has seen increased application over the years, particularly in the study of porous materials. The principal advantage of this technique lies in its non-destructive nature, enabling a comprehensive investigation into internal structures and phenomena without inducing modifications or damage to the materials. 3D X-ray computed tomography allows complete volumetric reconstructions, offering a way to explore the material's internal structure without any damaging effects. X-ray computed tomography also allows 4D imaging, i.e., permitting real-time observation of dynamic phenomena by scanning the volume continuously or intermittently over time.

A conventional X-ray tomograph typically comprises two primary components: an X-ray source and a detector. The fundamental process of obtaining an X-ray scan involves emitting X-rays on the subject, where the detector captures the transmitted X-rays as shown in figure 2.7. When an X-ray beam interacts with matter, its intensity diminishes, a phenomenon known as attenuation. The amount of attenuation is primarily governed by two parameters: the linear attenuation coefficient (μ), closely related to the material's atomic number and its density[29], and the distance traversed by the X-ray photons within the material. The fundamental relationship between X-ray absorption and these two parameters for a homogeneous material can be mathematically expressed by Beer-Lambert's law in equation 2.18, where I_0 represents the initial X-ray intensity.

$$I = I_0 e^{-\int \mu \, dx} \tag{2.18}$$

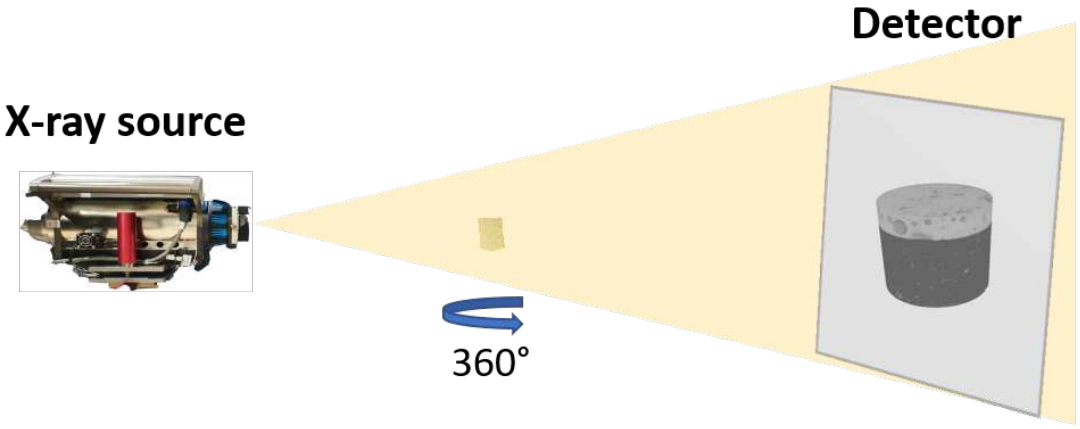

Figure 2.7: Scanning procedure using X-ray computed tomography

The emitted X-rays traverse the sample, and under the influence of three elements: the initial intensity, the linear attenuation coefficient μ of the material, and the thickness of the material x through which X-rays have travelled we obtain the transmitted X-ray intensity I. The detector captures these transmitted X-rays, generating a projection image, a radiograph. As the sample rotates, we obtain 2D projections of the entire sample. Through reconstruction, we achieve the 3D rendering of the sample, demonstrated in figure 2.8. The reconstruction process involves using these 2D projections to mathematically recreate the 3D structure of the sample.

This is typically achieved through techniques such as back projection in which the 2D projections are mathematically reversed and combined to create a 3D volume of the object's internal structure. Expanding the sample rotation beyond a full 360° introduces the concept of 4D continuous scanning in X-ray tomography. This extends beyond the spatial dimensions to include time, allowing the observation of dynamic changes within the studied samples. A dynamic monitoring is also achievable by performing 360° rotations with defined time intervals between each rotation.

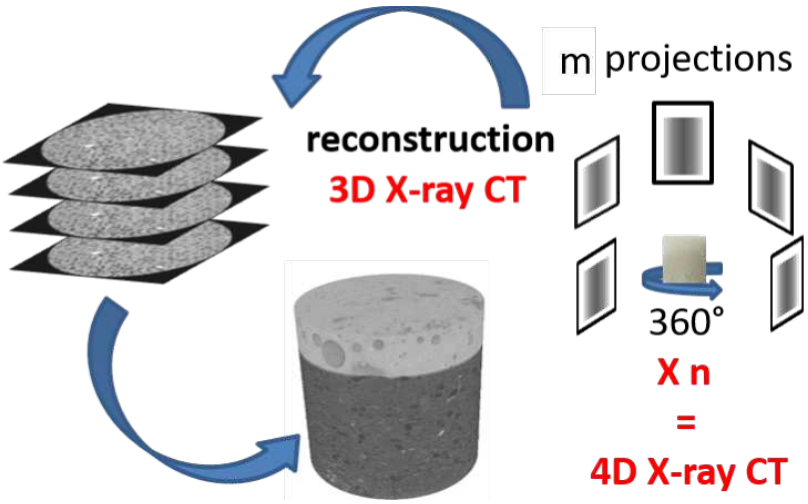

Figure 2.8: Schematic figure showing the reconstruction of 2D projection into a rendering of 3D volume

X-ray computed tomography (X-ray CT), like any experimental technique, is not without its limitations. One of the primary limitations pertains to spatial and temporal resolution. Depending on the research requirements, a compromise must be reached to achieve the desired scan. For instance, when imaging fast phenomena, spatial resolution may be compromised, while for improved contrast, temporal resolution might be compromised. Additionally, contrast resolution presents another significant limitation, especially for composite materials with similar attenuation coefficients. Distinguishing between such materials accurately using X-ray tomography remains a challenging task. Moreover, artifacts constitute a notable challenge in X-ray CT imaging. These artifacts stem from both the imaging device itself, such as ring artifacts which are presented usually as circles in the center of the reconstructed images and are due to a defect in the detector, as well as characteristics of the scanned object. For instance, in the case of the study involving tiles, the large difference in attenuation between the clay body (showing low attenuation) and the glaze (showing high attenuation) posed a significant challenge which is discussed in chapter 3 in section 3.2.3.1.

In this study, we employed two distinct scanning instruments, namely the ZEISS Xradia Versa 510 scanner and the TESCAN Unitom XL scanner, available at the DMEX Centre for X-ray Imaging at the University of Pau and Pays de l'Adour and depicted in Figure 2.9. The selection of scanning apparatus was dictated by the specific experimental requirements of each chapter, underscoring our adaptability to the characteristics of the phenomena under investigation. The ZEISS scanner was utilized in Chapter 3, where in-situ experiments were not required. The observed phenomena in this chapter displayed gradual slow changes, making continuous imaging impracticable. In contrast, Chapter 4 entailed the examination of phenomena characterized by a considerably higher rate of change, necessitating the need for continuous scanning capabilities. In this context, the TESCAN scanner, with its rapid scanning capabilities, was used. It enabled real-time data to be acquired and the dynamic evolution of the phenomena studied to be monitored accurately.

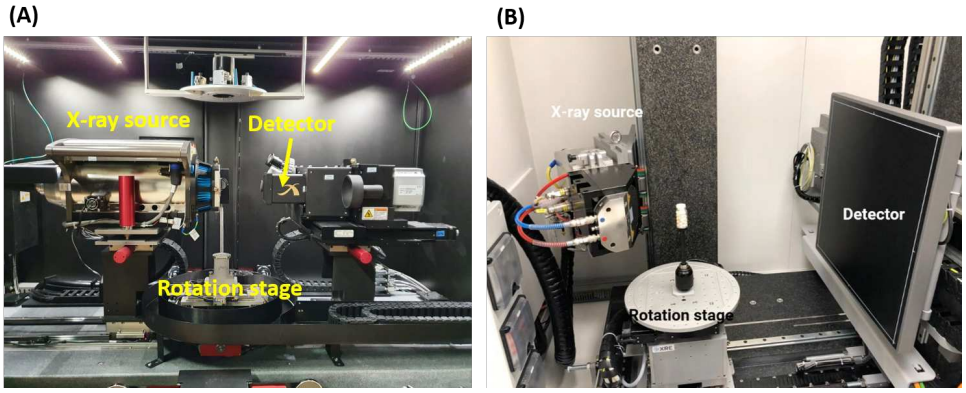

Figure 2.9: (A) ZEISS Xradia Versa 510 scanner, (B) the TESCAN Unitom XL scanner

2.2.1.6 Image analysis

Once 3D or 4D X-ray Computed Tomography (XCT) data is acquired, the subsequent phase involves image analysis to derive qualitative and quantitative understandings from the studied sample. An initial and fundamental step in this analysis often involves data filtering. This is essential as the acquired data may be noisy or contain artifacts resulting from either the imaging device or the intricate composition of the scanned materials. The filtering process is typically executed either during reconstruction or within the image analysis phase. In either approach, this operation serves to eliminate factors that could potentially distort the interpretation of the data, ensuring a more accurate and reliable analysis.

To distinguish between the different phases of the porous material, global thresholding was employed in this thesis work. Global thresholding involves the establishment of ranges of grayscale values covering the defined regions of interest within the distinct phases of the porous media. These grayscale values are determined by analyzing the image histogram, as explained by P.Iassonov in [30]. The thresholding will result in a binary image as shown in Figure 2.10. This process essentially assigns a distinct grey value to the part we're interested in understanding and gives everything else a different grey value. For instance, if we want to analyze the air inside a porous material, we might assign a grey value of 1 for the air and a grey value of 0 for everything else. This way, we can easily distinguish and study the air phase within the material.

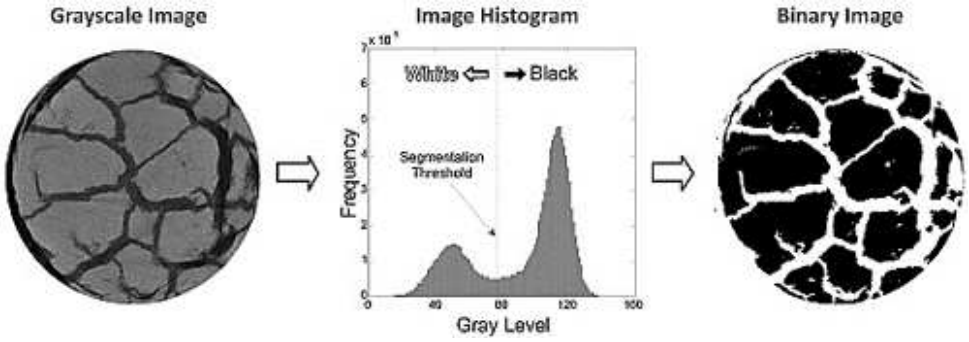

Figure 2.10: Illustration of histogram-based thresholding: the greyscale image was segmented based on the histogram to create the binary image representing the two phases solid in black and air in white [30]

For single scans, global thresholding was performed manually. In the case of dynamic scanning, an automated workflow was implemented to obtain time-resolved volumes of the desired phases. For a comprehensive understanding of the specific image analysis methodologies employed in each case study in this thesis, detailed information can be found in the respective chapters.

2.2.2 Climate Control Methods

2.2.2.1 WEISS climatic chamber

In this thesis, we employed a WEISS C34/40 climatic chamber for the drying experiments, as illustrated in Figure 2.11. The climatic chamber offers the advantage of providing a controlled environment with precise temperature and relative humidity regulation. This apparatus was used when we needed to store the samples in a controlled environment for an extended period of time.

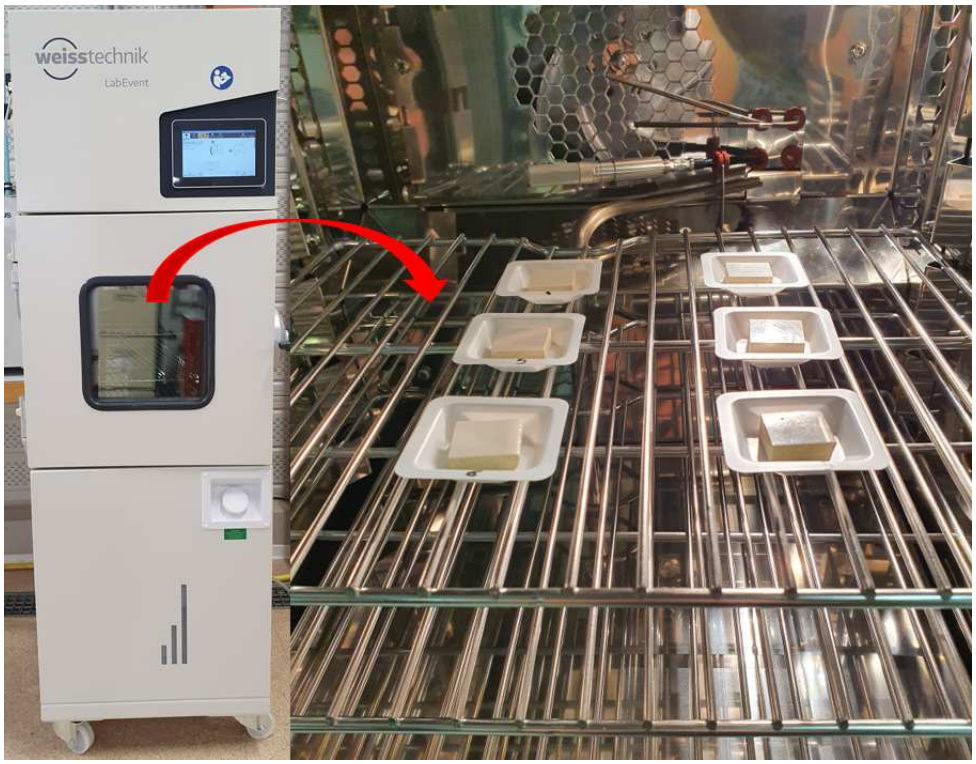

Figure 2.11: WEISS C34/40 climatic chamber

2.2.2.2 Humidity generator and conditioned chamber

In order to have a controlled humidity environment for the in-situ balance measurements and drying experiments inside the scanner conducted in chapter 4, we designed a custom chamber to address the specific requirements of the different used setups (balance and scanner) as shown in figure 2.12. The chamber was linked to an L&C RH-200 humidity generator.

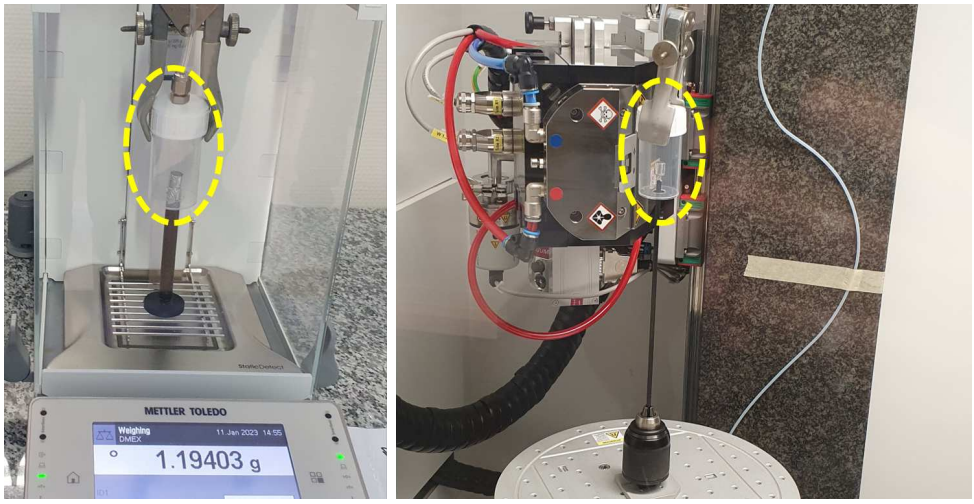

Figure 2.12: Custom-made chamber used in the in-situ experiments: yellow dotted

Throughout our experiments, we maintained a standardized air pressure of 10 psi, an evaporation temperature of 40°C, and a transfer line temperature of 40°C for the humidity generator. We consistently operated in high flow mode with an airflow rate of 500 cm^3/min. The humidity generator takes into account the parameters mentioned above, as well as the room temperature, to generate the desired relative humidity. Since the chamber was open at the bottom, the generated relative humidity was also influenced by the surrounding room's relative humidity. To account for this variation, a calibration procedure was conducted before each experiment. The actual relative humidity in the chamber was measured using a probe, and the desired generated relative humidity from the humidity generator was adjusted to achieve the target relative humidity.

Chapter 3

Material bi-layer: application on Dutch tiles

This chapter is based on the draft of a journal article on "Salt Weathering in Antique Dutch Ceramic Tiles", which is currently being prepared for submission. The article is the result of a strong collaboration between two PhD students involved in the CRYSTINART project, Tinhinane Chekai from UPPA and Rozeline Wijnhorst from UvA. Both students will share the first authorship of the journal article, reflecting their equal contribution.

Initially, the chapter delves into the structural properties of the tiles, employing X-ray tomography, performed by Tinhinane Chekai, and SEM (Scanning Electron Microscopy), performed by Rozeline Wijnhorst. The porosity and the density were characterized by Tinhinane Chekai using the EN ISO 10545-3 as well as the pore size distribution using mercury intrusion porosimetry. Moving on to the hygric properties of the tiles, Tinhinane Chekai contributed by characterizing the drying properties and performing capillary imbibition experiments. Additionally, mechanical properties are explored, with Tinhinane Chekai undertaking the characterization of compressive strength and elastic properties inherent to antique Dutch tiles. Subsequently, the focus shifts to an in-depth investigation of salt weathering in these tiles using different characterization techniques: Tinhinane Chekai utilized X-ray tomography, while Rozeline Wijnhorst employed SEM and a profilometer. The chapter concludes with a comprehensive discussion, presenting the joint reflective work by the two research teams on the results obtained, exploring the impact of the tiles' properties and salt types on the observed salt accumulation and resulting damage.

Contents

3.1 Introduction

During the 16th century, the Netherlands emerged as a prominent centre for ceramic manufacturing, giving rise to tin-glazed tiles. Initially conceived as decorative indoor architectural elements, these tiles were soon used in outdoor structures as well [6]. With time, these artifacts witnessed progressive deterioration, primarily attributed to the persistent influence of moisture and salt. The sources of moisture and salt intrusion include the capillary rise of groundwater, exposure to sea spray, and the presence of water and salt within mortar joints between tiles [23]. The degradation of these tiles manifests in two predominant patterns: glaze crazing, characterized by perpendicular cracks on the glaze that may penetrate the clay body, and shivering, the removal of glaze and sometimes portions of the clay body itself [6]. Prior research on tin-glazed tiles is found in the field of art conservation and has primarily focused on the manufacturing processes and chemical compositions, demonstrated, for example, by the works of [6] and [9]. They unravel the original recipes used in manufacturing antique Dutch tiles in order to derive information that will aid in the interpretation of chemical and material analysis, possibly placing issues of susceptibility to deterioration within a clearer historical context. Few studies focus on the impact of salt weathering on antique Dutch tiles. A better understanding of this deterioration risk would assist conservators in defining preservation methods for historically valuable tiles. In addition, the durability of reused antique tiles is a primary interest of actors involved in the circular economy in the construction industry.

Assessing the durability of building materials with respect to salt weathering is not always straightforward. There is currently no unified approach among researchers that defines one single test protocol [42]. The RILEM Technical Committee ASC-271 (active between 2016 and 2022), attempted to tackle this problem by developing a generally applicable salt weathering (TC) test procedure [37]. The method acknowledges the importance of a certain salt accumulation level to initiate damage and characterizes salt-induced damage as a two-stage process involving an accumulation and a propagation phase. Two distinct weathering protocols were implemented for sodium chloride and sodium sulfate, each protocol having a duration of 9 weeks for sodium chloride and 8 weeks for sodium sulfate. In both cases, the accumulation stage involved saturating the samples with the respective salt solution through capillary action, followed by drying at 40°C and 15±5% relative humidity until 80% of the absorbed water had evaporated. The propagation stage entailed pure water rewetting and drying cycles of the samples in the case of sodium sulfate and hygroscopic adsorption at 95% relative humidity and drying in the case of sodium chloride. However, the new test procedure was developed focusing on single building materials only.

There are only limited studies on salt weathering of bi-layered materials, such as ceramic tiles. Previous studies in this field, as conducted by Lurdes Esteves [22], have primarily focused on the examination of Portuguese tiles known as "Azulejos." These studies typically involved testing samples of tiles that had previously been contaminated with salts. It is important to note that even though the samples were desalinated before testing, the desalination process itself could introduce some level of damage, as observed during their testing. Their weathering protocol consisted of 5 sets of 15 cycles of imbibition and drying on tile samples (typically 5 by 5 cm), resulting in an extended test duration of 17 months and 29 days, and using only sodium chloride. In our study, we expand our focus to include the effects of sodium sulfate. In contrast to previous lengthy ageing tests, we introduce a faster method to induce damage in Dutch tiles. Notably, many prior samples had already deteriorated before testing, while our investigation includes a wider range of samples, including undamaged ones and those exhibiting a specific type of weathering known as crazing, that is, when a map of almost perpendicular cracks is created on the glaze, sometimes shallow and sometimes going all the way to the clay body. Additionally, our research addresses the absence of 3D analyses of salt accumulation patterns and salt damage in tin-glazed tiles. We employ X-ray computed tomography (CT) to provide a comprehensive perspective on this aspect.

In this paper, we will start by presenting an in-depth examination of the structural, hygric, and mechanical properties inherent to antique Dutch tiles. Subsequently, we investigate the details of salt weathering in those tiles, followed by a comprehensive discussion on the results obtained and the impact of the tiles' properties as well as the salt type on the observed salt accumulation and damage.

3.2 Materials and Methods

3.2.1 Materials

Samples were purchased from the company Regts - Antieke Tegels (The Netherlands) which collects and resells antique Dutch tiles. The square white tiles, 13 cm x 13 cm in size, date from the era 1780 – 1900 and come in two different states: with craquelure (crazed) and with intact glaze as shown in figure 3.1. The tiles have an average height of 8 mm, including the glaze layer of 0.3 mm. Sub-samples were cut from these tiles for the different characterization methods, characterizations were done on two-layered samples (that is, including the glaze and the clay body), or on the clay body only. To that extent, the glaze was removed using a polishing machine. Two salts were selected, sodium chloride (NaCl) and sodium sulfate (Na_2SO_4), known to be highly damaging to building materials [42]. At temperatures above 0°C, sodium chloride crystallizes in its anhydrous form known as halite, while sodium sulfate can crystallize in various hydrated or anhydrous phases, depending upon temperature and relative humidity conditions. Sodium sulfate has been observed to be particularly damaging during laboratory weathering testing at room temperature, primarily due to the transition between thenardite (Na_2SO_4) and mirabilite (Na_2SO_4·10H_2O), which generates high crystallization pressures [42, 19].

For the experiments detailed in this paper, salt solutions with concentrations equivalent to 90% of the saturated concentration at room temperature were employed, that is a 5.5 molal solution of sodium chloride and a 1.26 molal solution of sodium sulfate. The choice of these concentrations allows the samples to reach capillary saturation with the salt solution, thus reducing the risk of salt crystallization during the saturation process, which could lead to pore blockage and prevent the samples from reaching capillary saturation.

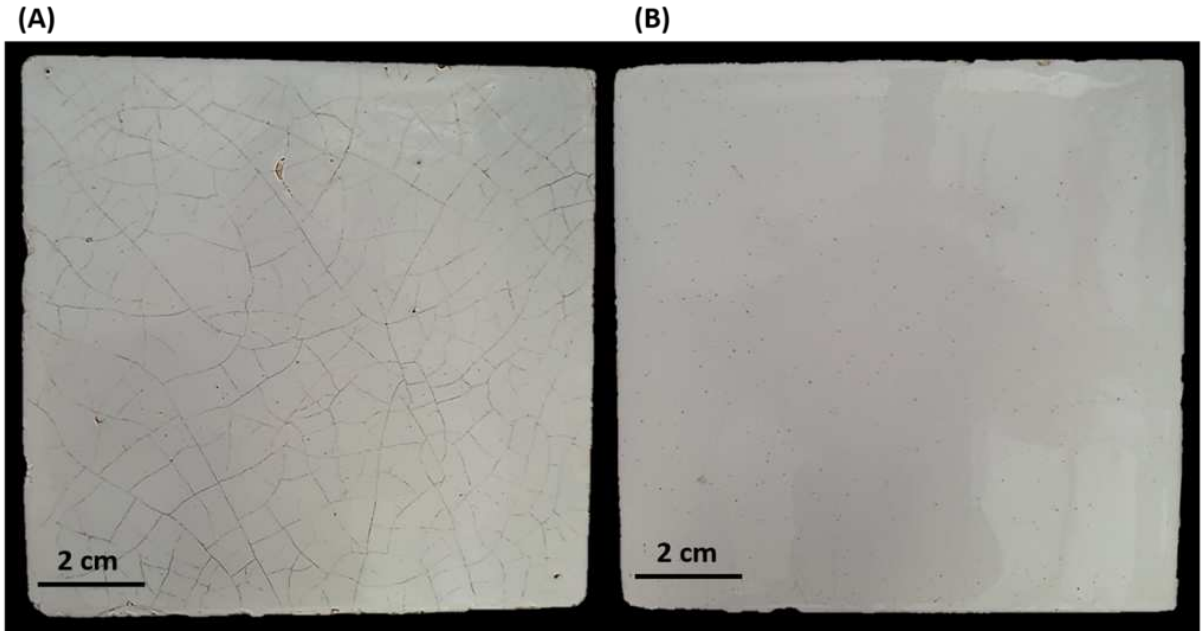

Figure 3.1: Photographs showing: (A) a crazed tile, (B) an intact tile

3.2.2 Microstructural, hygric and mechanical characterization

3.2.2.1 Microstructural characterization

Microstructural analysis of the tiles involved X-ray computed tomography (XCT) and scanning electron microscopy (SEM). High-resolution scans at 5.25 µm resolution were conducted on four small samples (5 mm in diameter), with two samples extracted from intact tiles and two from crazed tiles, using a ZEISS Xradia Versa 510 scanner. Given the substantial attenuation differences between the glaze and clay body layers in the tin-glazed tiles, a two-step scanning approach was defined. The initial scan was optimized to efficiently capture both the glaze and the upper section of the clay body, followed by a second scan that solely targeted the clay body to enhance contrast as explained in section 3.2.3.1. SEM imaging and energy dispersive X-ray spectroscopy (EDX) were performed using a Hitachi TM3000 Tabletop electron microscope. Additionally, X-ray diffraction (XRD) analysis was conducted on 1 cm3 of powdered clay body, manually ground and sieved at 100 µm, utilizing a BRUKER D2 PHASER with a 160-channel linear SSD detector at a 4° opening in 2 theta.

3.2.2.2 Hygric characterization

The porosity and density of the clay body of the intact and crazed tiles were assessed employing the European standard EN ISO 10545-3 [31]. Five samples were characterized for each clay body type, each measuring 2 cm x 2 cm x 7 mm. The pore size distribution analysis of the clay body of both intact and crazed tiles was conducted through mercury intrusion porosimetry (MIP). For this purpose, two samples of 2 cm x 2 cm x 7 mm were extracted from an intact tile and two from a crazed tile. Subsequent to glaze removal, the samples were dried in an oven at 45°C and 20% relative humidity (RH) for a duration of 72 hours. Once dried, the samples were carefully fragmented using a pincer and thereafter subjected to a vacuum environment of 14 Pa and 80°C for a period of 24 hours. Two fragments were utilized from each sample, each fragment weighing around 1.8 g. Employing a micrometrics AutoPore IV unit, mercury intrusion measurements were executed on the selected fragments, spanning from atmospheric pressure up to 4136 bar to comprehensively capture the pore structure characteristics.

Capillary imbibition experiments were furthermore conducted manually in order to capillary saturate the tested samples before beginning the drying experiments. This operation included three distinct scenarios: (i) imbibition of pure water on crazed and intact tiles, (ii) imbibition of a 5.5 molal NaCl solution, and (iii) of a 1.26 molal Na2SO4 solution on intact tiles. Ten samples measuring 2x2 cm and 0.8 cm in height were extracted from a crazed tile. Among these, five samples retained the glaze layer, while the remaining five were subjected to polishing to eliminate the glaze. Furthermore, thirty-eight samples, with the same dimensions, were obtained from two intact tiles. Among these, twenty were polished to remove the glaze layer, and the rest remained with the glaze. Following 24-hour oven drying at 60°C, the samples were sealed along the sides using aluminium tape. Positioned in a grid-equipped container, at laboratory conditions of 40% relative humidity (RH) and a temperature of 20°C, the samples were oriented with the glaze facing upward for the samples that kept the glaze layer, and the polished side of the samples upwards for the samples that were subjected to glaze removal, allowing the bottom of the samples to be exposed to the respective fluids.

The samples were periodically weighed until a stable weight was reached. These capillary saturated samples were then used to assess the drying kinetics of the tiles. Using aluminium tape, the capillary-saturated samples were sealed at the bottom and subsequently subjected to drying within a WEISS C34/40 climatic chamber. The drying process occurred under controlled conditions of 25% RH and 21°C. Periodic weight measurements were recorded throughout the drying process. Additionally, to gather supplementary understandings into the drying behaviour of these tiles when exposed to sodium sulfate or sodium chloride, two samples with an intact glaze layer contaminated with each salt solution were scanned at the end of the drying process to understand the correlation between structural changes and the measured drying curves. Using a TESCAN UniTOM XL scanner, these scans provided valuable additional information regarding the effect of the salts on the drying kinetics of the tested samples.

3.2.2.3 Mechanical characterization

The evaluation of compressive strength for both the clay body of crazed and intact tiles was carried out referring to the NF EN ISO 10545-4 [41] standard for ceramic tiles. To assess this property, ten cylindrical samples measuring 3 mm in diameter and 7 mm in height were extracted from each tile category (crazed and intact). Zwick Z020 electromeca press machine with a capacity of 20kN was used to measure the compressive strength of the samples. A downward displacement rate of 0.1 mm/s was applied until the maximum compressive strength was attained. Meanwhile, the elastic properties of the clay body in the intact Dutch tiles were evaluated using the ultrasonic pulse velocity (UPV) technique. This method is based on the measurement of compressive and shear wave travel times through the clay body. For this experiment, eight square samples of 6x6 cm were extracted from two intact Dutch tiles. Following 72-hour oven drying at 45°C, the samples were subsequently measured individually using a Proceq Pundit® 200 UPV device. The calculation process for determining Young's modulus and Poisson's ratio is explained as follows:

$$E = 3K(1 - 2\nu) \tag{3.1}$$

$$\nu = \frac{3K - 2G}{2(3K + G)} \tag{3.2}$$

Where E is Young's modulus, ν is Poisson's ratio, G and K are the shear and bulk modulus, respectively where:

$$G = (V_s)^2.\rho \tag{3.3}$$

Where ρ is the density of the material and V_s represent the shear wave velocity, where:

$$V_s = \frac{L}{T_s} \tag{3.4}$$

Where L stands for the length travelled by the sample, T_s represents the travel times of the shear waves.

$$K = (V_p)^2.\rho - \frac{4}{3}G \tag{3.5}$$

where :

$$V_p = \frac{L}{T_p} \tag{3.6}$$

Where V_p represents the compressive wave velocity, T_p represents the travel times of the compressive waves.

3.2.3 Salt weathering and assessment of crystallization damage

Within this study, a salt weathering protocol was developed. This protocol involved exposing samples to repeated wetting and drying cycles, employing 5.5 molar sodium chloride and 1.26 molar sodium sulfate solutions. A total of eight samples were employed, evenly distributed between intact and crazed Dutch tiles.
To accommodate various assessment techniques, two distinct sample shapes were used: four square samples measuring 2 x 2 cm with a height of 0.8 cm (comprising two intact and two crazed tiles, with one set per salt type), and four cylindrical samples with dimensions of 0.5 cm in diameter and 0.8 cm in height (comprising two intact and two crazed tiles). Each wetting and drying cycle followed a precise sequence: (i) initial sample preparation involving drying in an oven at 60°C for 24 hours, followed by weighing; (ii) introduction of a saline solution into the samples through capillary absorption from the sample's bottom for 10 minutes, conducted under laboratory conditions at 20°C and 50% relative humidity; and (iii) complete sealing of the samples with aluminium tape, excluding the glaze surface. Subsequently, the samples were transferred to a controlled climatic chamber, maintained at 21°C and 25% relative humidity, for the drying phase. The drying phase was initially set at a duration of 7 days. However, at the end of the first cycle, it became evident that the drying process was considerably slower than anticipated.

In response to this observation, the drying phase was extended and continued until the samples reached a fully dry state, at which point it was stopped. The weight of each sample was noted before and after each cycle, allowing for the monitoring of drying and salt quantity introduced into the samples. A total of three wetting and drying cycles were executed over a four-week period.

For the assessment of salt crystallization and damage to the glaze, a confocal profilometer (Keyence VK-X1100) was used to scan the surface of the 2 by 2 cm tiles. This technique makes it possible to create a detailed image of the surface of the tile and to make a height map of its surface. By comparing the initial maximum height differences within one sample with the maximum height differences over time it is possible to follow changes in the structure of the glaze before extra cracks and damage are observed. The scans were made at a 5x magnification under ambient conditions on the squared samples. The Keyence software was used to create height maps and analyze height differences. Profilometer scans were performed before the first weathering cycle and after each weathering cycle (4 times in total).

Scanning electron microscopy (SEM) was used to get a better understanding of the microstructure of the tiles, glaze and the forming salt crystals. After each cycle, SEM images were made to study the evolution of salt crystallization on top of the glaze, next to the glaze and growing out of the cracks in the glaze.

Unlike preceding methodologies which primarily assessed surface salt-related effects, X-ray CT facilitated comprehensive insights into both internal salt accumulation and associated deterioration. To optimize results, as detailed in section 3.2.3.1, cylindrical samples were selected for this technique, as previously described in section 3.2.2.1. At the beginning of the process, an initial scan labelled "scan0" was performed on the dried sample prior to exposure to the saline solution. This scan served as a reference, capturing the sample's initial state. Two subsequent scans followed, "scan1" after the first cycle and "scan3" after the third cycle. In pursuit of further information, two extra cycles were introduced to the process. During these additional cycles, adjustments were made to the wetting procedure. Following the third cycle, the non-sealed bottom of the samples was exposed to the salt solution for a duration of 20 minutes. Subsequent to wetting, samples contaminated with sodium chloride were transferred to a climatic chamber under conditions similar to the controlled settings of the initial three cycles. Conversely, samples contaminated with sodium sulfate underwent a different procedure. These samples were maintained at laboratory conditions of 21°C and 42% relative humidity for 24 hours, after which they were transferred to the climatic chamber, and exposed to the same controlled climatic conditions of the preceding cycles. This particular step was performed to facilitate the thenardite-mirabilite phase transition of sodium sulfate, a crucial factor in inducing damage within porous materials. Further insights were gained through subsequent scans after the 4^{th} ("scan4") and 5^{th} ("scan5") cycle. To maintain consistency, all scans were conducted using identical scanning parameters and reconstruction protocols.

3.2.3.1 Scanning procedure: cylindrical samples: d=5mm, h=8mm

Due to the high attenuation of the glaze layer, and the low attenuation of the clay layer with respect to the glaze, the scanning of the tile samples was challenging. Scanning the glaze layer requires high energy, whereas going high in energy sacrifices the contrast in the clay body. We therefore opted to scan the samples in two steps. In the first step, we performed a scan that covers the glaze and the interface between the glaze and the clay body, which requires a sufficiently high energy to obtain sufficient transmission of X-rays.

In order to reduce streak artifacts created because of the difference in attenuation between the clay body and the glaze, the glaze-clay body interface was placed in the centre of the field of view (figure 3.2) during the first scan. In the second step, we performed a scan on the clay body only, with a lower energy to obtain a higher contrast. Here, the glaze was placed outside of the field of view as shown in figure 3.2.

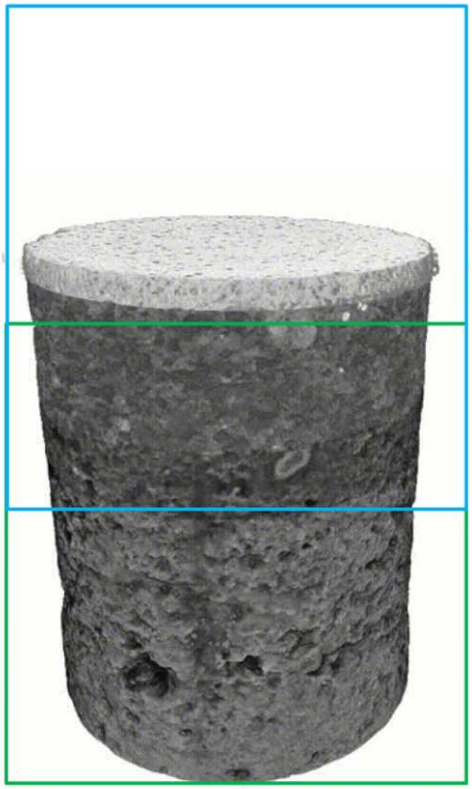

Figure 3.2: 3D rendering of the cylindrical sample showing the 80Kev scan's field of view in the blue square and the 50Kev scan's field of view in the green square.

The samples were scanned in a ZEISS Xradia Versa 510 with simple single 360° rotation scans. For each 360° rotation, an energy of 80keV and a power of 7W were applied in the first step scan and an energy of 50keV and a power of 4W for the second scan to acquire 1024 projection radiographs with a 5.25µm voxel size. The projection radiographs were taken with an exposure time of 4s for the 80KeV scan, and 9s for the 50KeV scan. The source-detector distance was set at 140.55mm, and the source-object distance was 10.75 mm for all of the scans. An optical magnification of 0.4 and a LE4 filter were used. Subsequently, the acquired scans were reconstructed using Reconstructor Scout and scan software specific to ZEISS Xradia Versa 510, using a filtered back-projection algorithm, including correction for beam hardening and ring artefacts. The total scanning time for one sample, including the top and the bottom scan, was 8 hours.

3.2.3.2 Scanning procedure: square samples: 20X20mm

As discussed in Section 3.2.3.1, the difference in attenuation between the glaze and clay body introduces streak artifacts. One method to mitigate these artifacts is to place the sample on a holder that rotates the sample base by 45°, as depicted in Figure 3.3. In a TESCAN UniTOM XL, a simple single 360° rotation scan was performed on the sample that got damaged during the drying experiment shown in figure 3.9. An energy of 100 keV and a power of 14W were applied to acquire 4283 projection radiographs.

An average of 5 projection images, taken with an exposure time of 235ms. The source-detector distance was set at 800 mm, and the source-object distance was 61.33. The used detector and magnification resulted in projection radiographs of 2856x2856 pixels with an 11.5 µm pixel size. A 1.5 mm aluminium filter was used during the scan. With the given parameters, the duration of a 360° rotation was 1h and 29 mins. Subsequently, the acquired scans were reconstructed using Panthera software specific to TESCAN UniTOM XL, using a filtered back-projection algorithm, including correction for ring artifacts and beam hardening.

Figure 3.3: Scanning of the 20X20mm sample: sample holder.

Image analysis was conducted using the Dragonfly (ORS) software (version 2022.1 and 2022.2 for [Linux]. Comet Technologies Canada Inc., Montreal, Canada; software available at https://www.theobjects.com/dragonfly). The initial step involved filtering the raw scans using a median filter to eliminate any present noise. The next procedure was registration, where all the scans of the same sample were superposed to align with one another. Manual registration was initially applied, followed by automatic rigid registration using mutual information similarity metrics with linear interpolation. To obtain insights into the salt accumulation within the porous structure and to complement the data acquired from balance measurements, the air content in each scan was segmented using manual thresholding. This technique involves selecting the greyscale interval corresponding to the air phase from the histogram of the image stack. The resulting binary images were then subjected to a cleanup process, wherein segments smaller than 20 voxels were considered noise and were removed. The identification of salt accumulation within the structure during cycling was accomplished through differential image treatment. This method involves arithmetic operations to distinguish differences between two images by calculating the arithmetic difference between pixel grey values from the compared images. Salt segmentation within the differential images was accomplished using manual thresholding, resulting in the creation of binary images. The binary images underwent further refinement, eliminating segments smaller than 20 voxels. A quantitative analysis of salt accumulation across sample height was conducted by analyzing the binary images using the slice analysis tool within Dragonfly ORS. Additionally, salt efflorescence was characterized by performing a subtraction operation between the mask of the scanned sample after each cycle, i.e., a binary image representing the complete volume of the sample, and the mask obtained from the reference scan (scan0). The reference scan's mask was generated via manual segmentation, wherein the grey scale values of the grains were selected. Utilizing morphological operations such as "fill holes," "dilate," and "close" within the Dragonfly software, a mask covering the entire structure was attained. The same procedure was repeated for each cycle, with the inclusion of both the grey scale values of the grains and the salt. The deformation during each cycle was acquired through non-rigid registration in the Dragonfly software. The Diffeomorphic Demons algorithm, sourced from the SimpleITK Demons registration library [5, 61, 36], was employed for this purpose, allowing to calculation of the displacements within each sample with respect to its reference state (scan0). As the nature of this registration is elastic, its applicability is constrained to the elastic deformation regime, i.e., prior to the occurrence of structural damage. It is important to note that the outcomes are primarily qualitative in nature; nevertheless, they offer valuable insights into the locations with potential susceptibility to damage initiation.

3.3 Results and discussion

3.3.1 Microstructural characterisation

Figure 3.4 illustrates cross-sections of both the glaze layer and the clay body, as observed in X-ray and SEM images. Within the glaze layer, for both tiles crazed and with an intact glaze we observed well-defined circular pores of varying sizes. The size variations observed in these circular pores can be attributed to the manufacturing process, particularly the formation of gas bubbles during the glaze firing stage [6]. In addition to the circular pores, SEM images also provided further confirmation that the glaze layer is essentially non-porous, with no discernible pore structures present (3.4(E)). On the other hand, the clay body exhibited a remarkable degree of heterogeneity. We observed numerous inclusions within the clay matrix, and it featured pores of diverse shapes and sizes, as clearly illustrated in 3.5. Notably, larger pores were found to be more present in the clay body of the intact tile when compared to the crazed tile as shown in 3.5. Furthermore, X-ray diffraction (XRD) analyses confirmed that the clay body of Dutch tiles consists of a mixture of calcium-rich clays. The XRD results are shown in 3.6. Soluble salts are found to be absent within the tile structures, indicating that the tiles did not contain any salt at the time of their purchase.

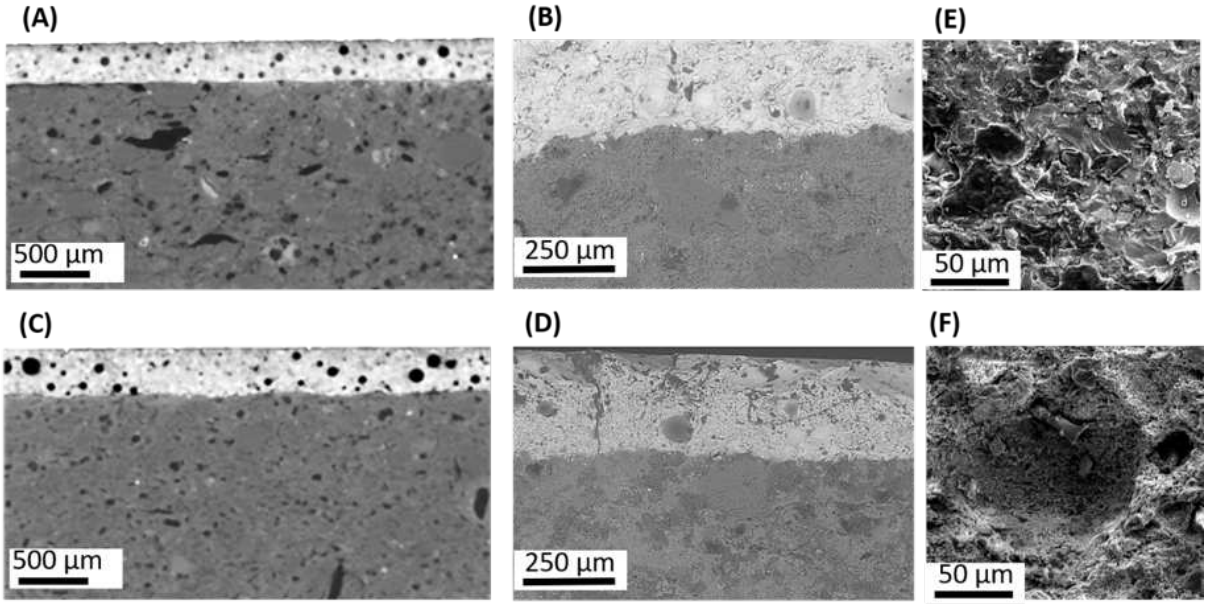

Figure 3.4: Vertical cross section of the: (A) intact tile, (C) crazed tile using XCT, (B) intact tile (courtesy of Rozeline Wijnhorst), (D) crazed tile using SEM (courtesy of Rozeline Wijnhorst), (E) a zoom in the glaze layer (courtesy of Othmane Darouich), (F) a zoom in the clay body using SEM (courtesy of Othmane Darouich).

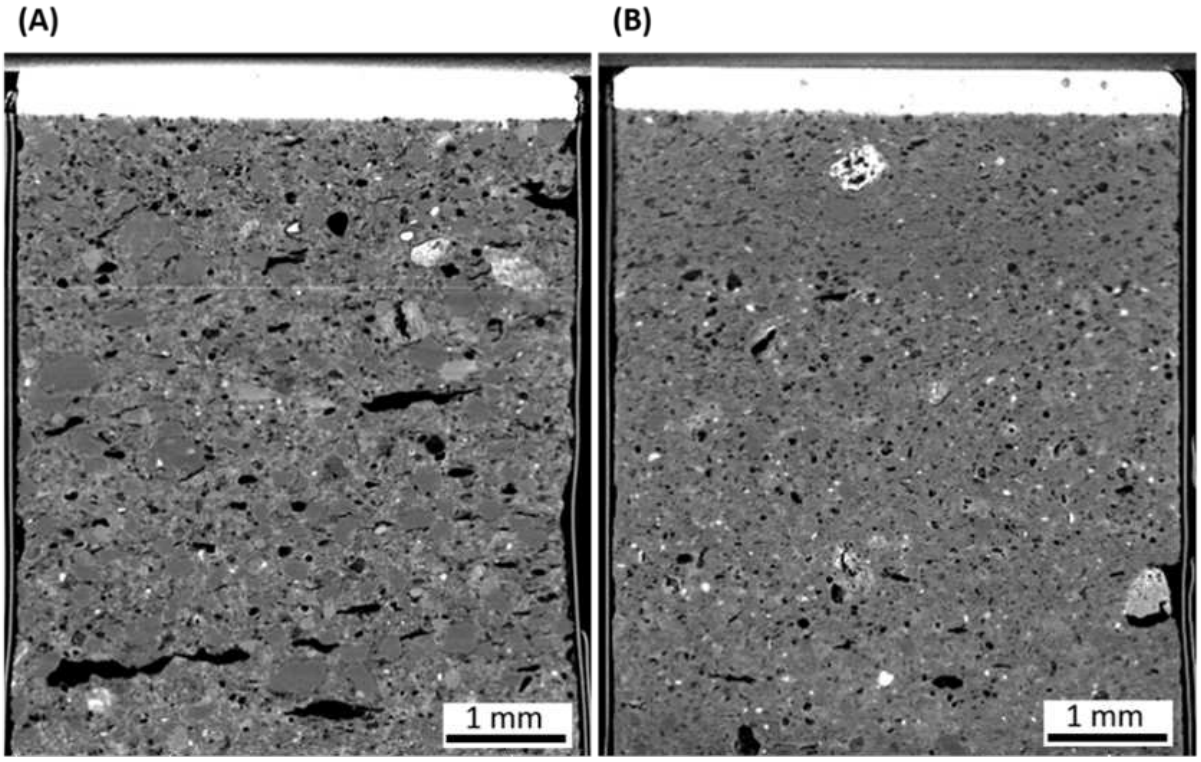

Figure 3.5: Vertical cross sections obtained from XCT scans showing (A) the intact tile, (B) the crazed tile

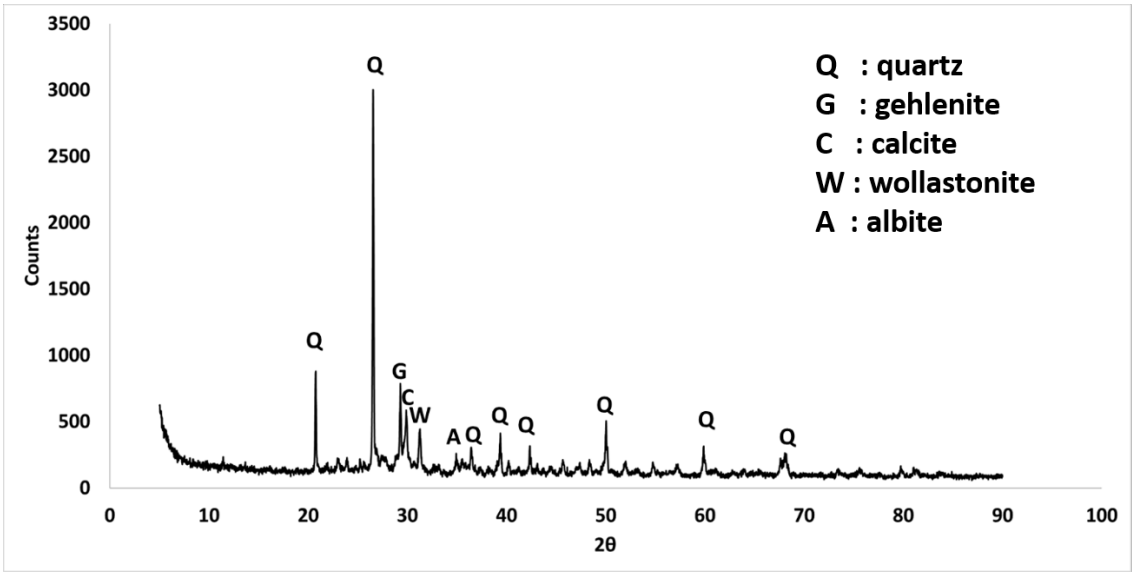

Figure 3.6: XRD characterization of the clay body of the Dutch tile (same XRD for the intact and for the crazed tile).

3.3.2 Hygric behaviour

Pore size distributions obtained from mercury intrusion analysis and from XCT image analysis of the clay body of intact and crazed tiles are presented in 3.7. Both clay bodies exhibited a bimodal pore size distribution. Analysis of the XCT scans on the intact and crazed Dutch tiles indicated the presence of larger pores, particularly in the intact tile, suggesting the presence of ink-bottle pores interconnected by smaller throats, which are characterized by the mercury intrusion technique [53].

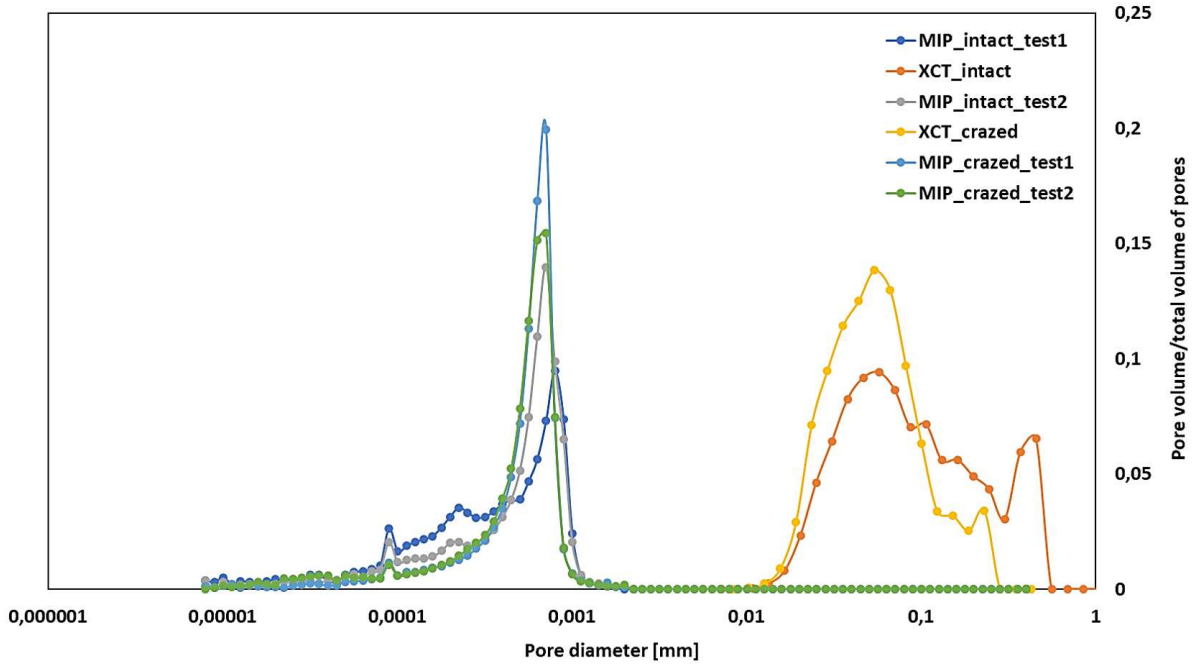

Figure 3.7: Pore size distribution of the clay body of the crazed and of the intact tiles provided from MIP measurements and from XCT image analysis.

Table 3.1 shows the open porosity and density of clay bodies for both crazed and intact tiles, as determined by EN ISO 10545-3 [31]standard testing and mercury intrusion analysis. The results indicate that the clay bodies of the tiles, regardless of their glaze condition, showed similar porosity and density.

Table 3.1: Porosity and density analysis of the clay body of the Dutch tile

Technique	EN ISO 10545-3 standard		Mercury intrusion porosimetry
Tile	Mean porosity (Std)	Mean density	Mean porosity (Std)
Clay body of crazed tiles	32.4% (1%)	1.71 (0.02)	34% (0.87%)
Clay body of intact tiles	34% (1%)	1.62 (0.02)	30% (1.35%)

The drying kinetics of the Dutch tiles, as illustrated in figure 3.8, revealed interesting insights. When saturated with pure water, there were no notable distinctions between the clay bodies of the two types of tiles (crazed or intact). Also, the two types of samples with intact glaze and those with crazed glaze showed similar behaviour when saturated with pure water. The drying process can be described in two phases: in the first phase, the drying rate is relatively high (regime 1). This is primarily due to the drying front being situated at the surface of the samples, making the drying rate dependent on external climatic conditions. Later, in the second phase, the drying rate gradually decreases. In this stage, the drying front moves to the lower regions of the samples, and the drying process is mainly governed by diffusive vapour transport through the upper dry zone. This is similar to the typical drying behaviour of a porous media as discussed by Coussot [15]. Importantly, the presence of crazing in samples from crazed tiles does not seem to significantly impact the drying behaviour of the tiles. However, the presence of the glaze considerably slows the drying of the samples which is due to the impermeability of intact glaze and the often shallow or low-permeability nature of glaze crazing as discussed in the work of Pereira [44] When a wall tile is drying, it typically occurs through the joints between the tiles due to the impermeable glaze [39]. In our case, drying takes place through the spaces between the sample and the aluminium sealing, which makes the drying pattern in our experiment resemble the natural drying process of tiles installed on a wall. On the other hand, when examining the drying behaviour of clay bodies saturated with salt solutions, a distinct pattern occurs. These samples exhibited a slower drying rate compared to those saturated with pure water. Additionally, the formation of a salt crust on the sample's surface as shown in Figure 3.9(A)1 and 3.9(B)1 further delays fluid transport, contributing to the overall slower drying of these samples. The observed efflorescence in the case of sodium chloride was stiff and sticky, whereas in the case of Na_2SO_4 the efflorescence was fluffy and easy to remove as shown in figure 3.10. In the presence of the glaze, an interesting observation was made with samples saturated with sodium sulfate. The 5 samples presented an unexpectedly high slope in the drying that was even higher than the drying slope when the samples were only saturated with pure water. An X-ray CT scan (3.9(B)4) revealed a substantial accumulation of Na_2SO_4 efflorescence that displaced the aluminium sealing, along with cracks in the Na_2SO_4 crust, increasing the drying area and explaining the faster drying. In contrast, the samples saturated with sodium chloride showed a very slow drying behaviour. An X-ray CT scan revealed that the NaCl crust was covering the surface of drying, and that drying only occurred through the crust as shown in Figure 3.9(A)4. An additional SEM image in Figure 3.9(A)5 and Figure 3.9(B)5 shows the morphology of the efflorescence for both salts, sodium chloride and sodium sulfate. It is worth noting that 2 of the dried samples contaminated with sodium chloride showed macroscopic damage during the drying process.

The damage manifested as glaze detachment and elevation from the clay body. An X-ray CT scan (Figure 3.9(C)) revealed a crack extending from the glaze to the clay body, parallel to the clay body-glaze interface. In the work of L.Esteves et al.[23], it was mentioned that during the manufacturing of the tiles, the presence of discontinuities and voids inside the clay body can lead to the formation of weak spots in the tile, making it more susceptible to degradation over time. In the damaged sample shown in Figure 3.9(C), the crack follows the large pores present in the clay body near the interface which could suggest that the damage was influenced by the already present defect i.e. the large pores.

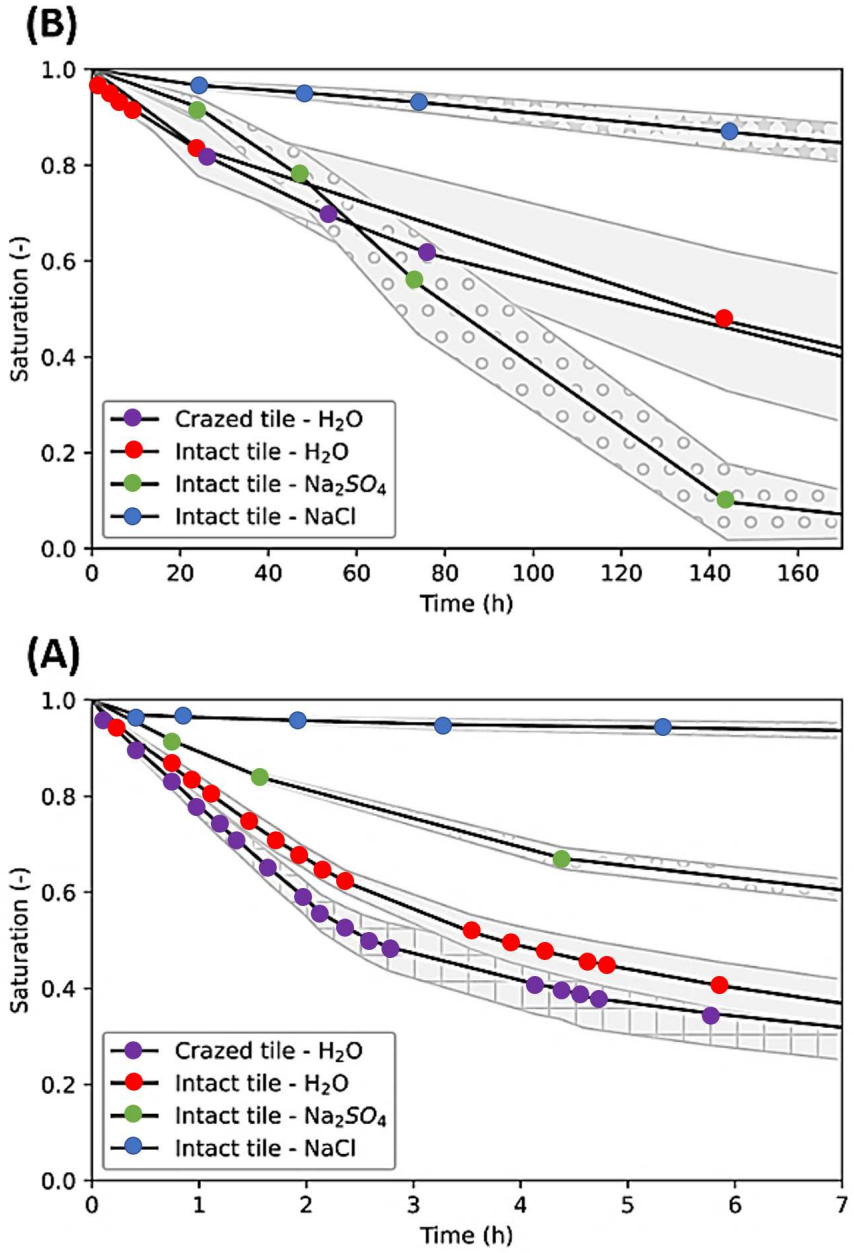

Figure 3.8: Drying kinetics of the 2X2 cm Dutch tiles: (A) represents the drying kinetics of the clay body of intact and crazed tile when contaminated with pure water and clay body of intact samples when contaminated with sodium chloride or with sodium sulfate, (B) represents the drying kinetics of the crazed and intact samples when contaminated with pure water, and intact samples when contaminated with sodium chloride or with sodium sulfate. Dots represent the averaged values and hatched areas are the standard deviation.

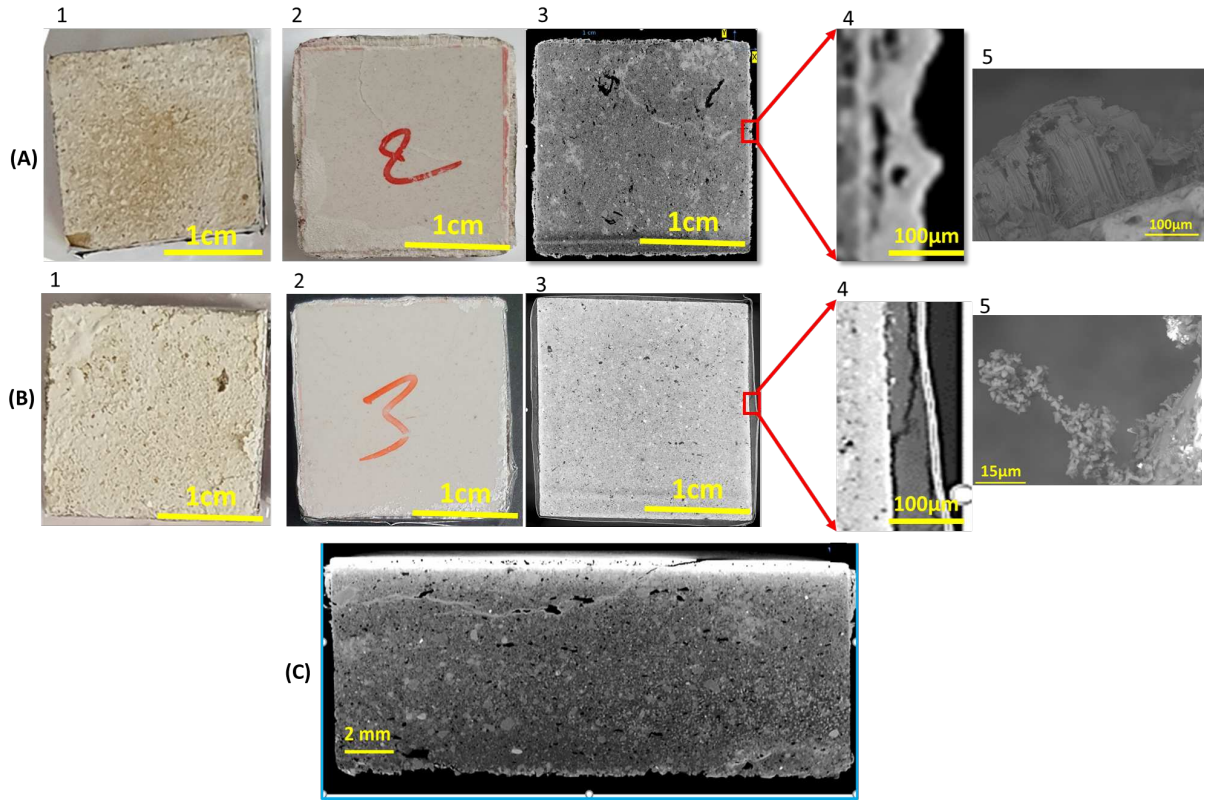

Figure 3.9: Results of the drying experiments: (A) sodium chloride experiments, and (B) sodium sulfate experiments, where (1) photographs of the clay body are shown and (2) photographs of samples with an intact glaze, (3) horizontal cross section within the clay body of the reconstructed XCT scan, (4) the salt crust from XCT (4) and (5) the salt crust from SEM (courtesy of Rozeline Wijnhorst). (C) vertical cross section of XCT 3D reconstruction showing the damaged sample during the drying experiment in the presence of NaCl.

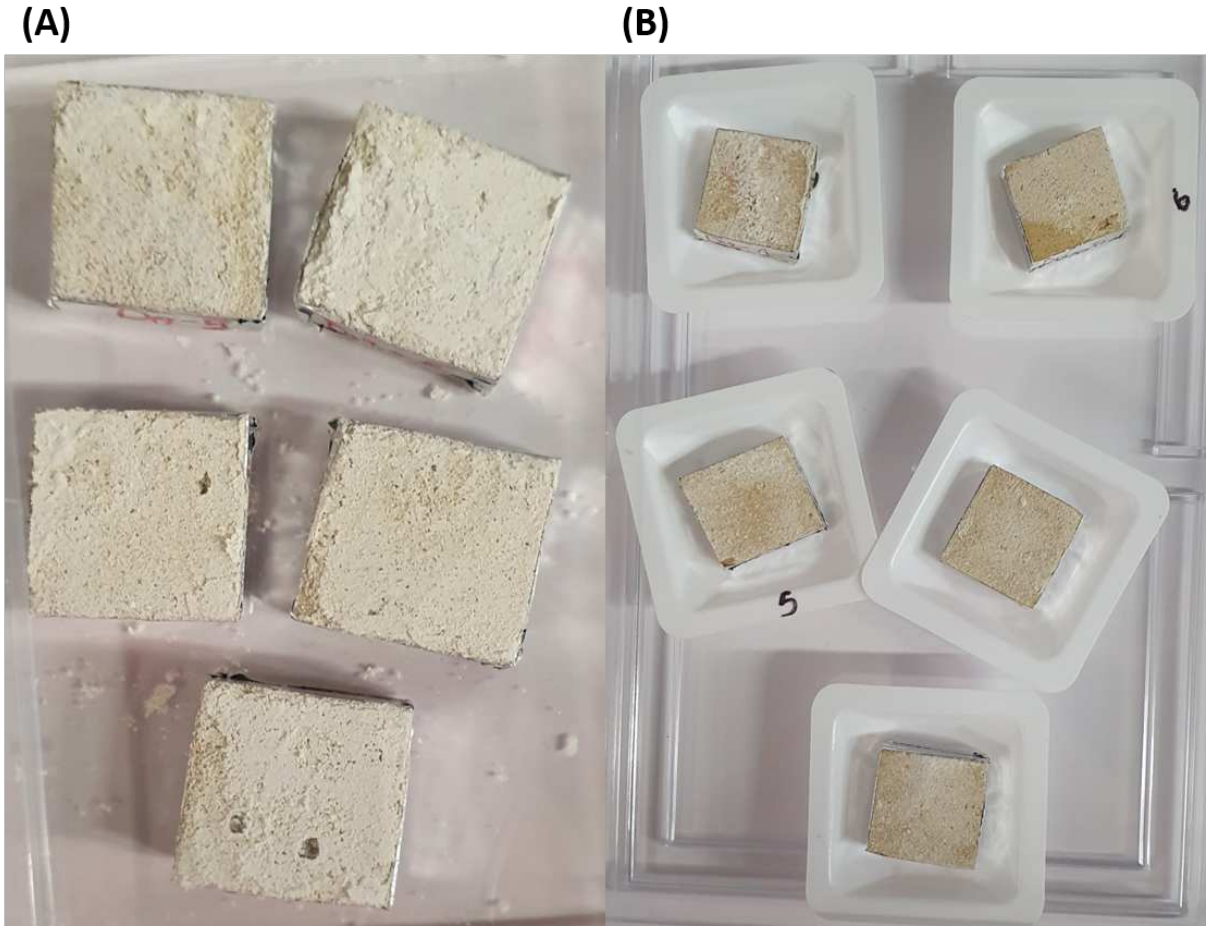

Figure 3.10: Salt efflorescence manifesting in the non glazed samples after drying: (A) Na_2SO_4 contamination, (B) NaCl contamination

3.3.3 Mechanical characterization

The compressive strength of the clay body of the crazed tiles as well as the clay body of the intact tiles is presented in table 3.2. The clay bodies of all tiles showed similar compressive strength.

Table 3.2: Compressive strength of the Dutch tile

Tile	Compressive strength (MPa) (Std)
Clay body of crazed tile	20.45 (0.51)
Clay body of intact tile	21.57 (0.71)

The ultrasonic measurements showed homogeneous elastic properties when measuring them on intact tiles with values of 16,8 GPa (std=5,44E+08) and 0,26 (std=7,81E-03) for the Young's modulus and the Poisson ratio respectively.

While the tensile strength was not measured during this study due to the complexity of performing such measurements on the tiles, given their height of less than 10 mm, the resulting pore size distribution of the clay bodies in the two types of samples could suggests that the clay body of the crazed tiles has a higher tensile strength compared to the clay bodies of the intact tiles. This hypothesis is based on the observation that the clay body of the intact tiles contains more large pores than the clay bodies of the crazed tiles, which could potentially result in a lower tensile strength, as discussed by M. Heap et al. [27].

3.3.4 Salt weathering

Weight monitoring of the samples consistently indicated salt accumulation throughout all cycles of the weathering test as shown in figure 3.11. Throughout all cycles, we observed a consistent accumulation of salt in all samples except for intact samples in cycle 2. The minor increase in salt accumulation in the intact samples during the second cycle can be attributed to the non-dryness of the samples. Initially, we aimed for a 7-day duration for each cycle in the weathering test. However, after slow drying in the samples following the second cycle, we adjusted our approach. Subsequent cycles were initiated only when the samples had dried. Only the crazed sample underwent five cycles, as the intact sample contaminated with sodium sulfate was damaged during the fourth cycle. Additionally, the intact sample contaminated with sodium chloride exhibited slow drying kinetics, limiting the experiment to four cycles.

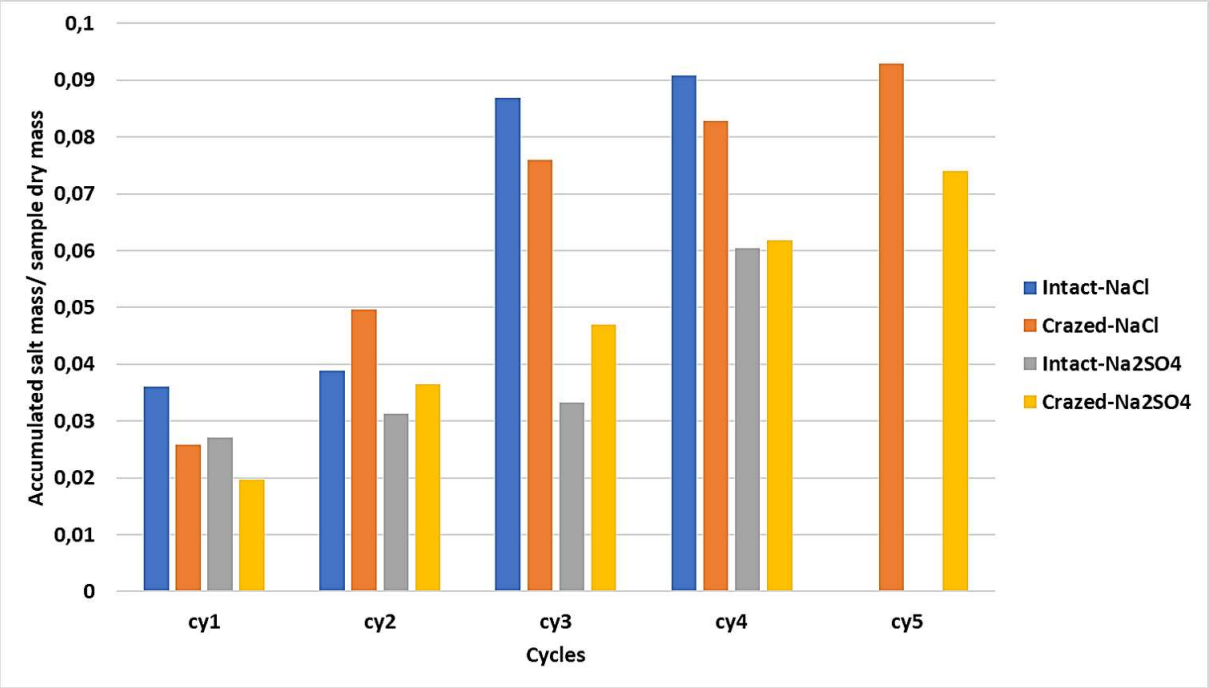

Figure 3.11: Representative figure of salt content increase during the cycling of the samples.

In the context of weathering in the presence of sodium chloride, X-ray CT scans revealed efflorescence in both intact and crazed samples, as shown in Figure 3.12(C). Figure 3.12(D)

illustrates the drying kinetics of the cylindrical samples, where the crazed sample dried faster than the intact sample.

This drying kinetics supports the notion that drying took place via the space between the sealing and the sample and that the crust significantly delayed the sample's drying process. SEM images in Figure 3.12(A) demonstrated salt growth within the craquelures of crazed samples, indicating that the crazing may not have been shallow. While this did not impact drying kinetics, salt accumulated within the cracks of the crazed surface. Figure 3.12(B) also displayed SEM images revealing salt spreading over the glaze in the intact sample.

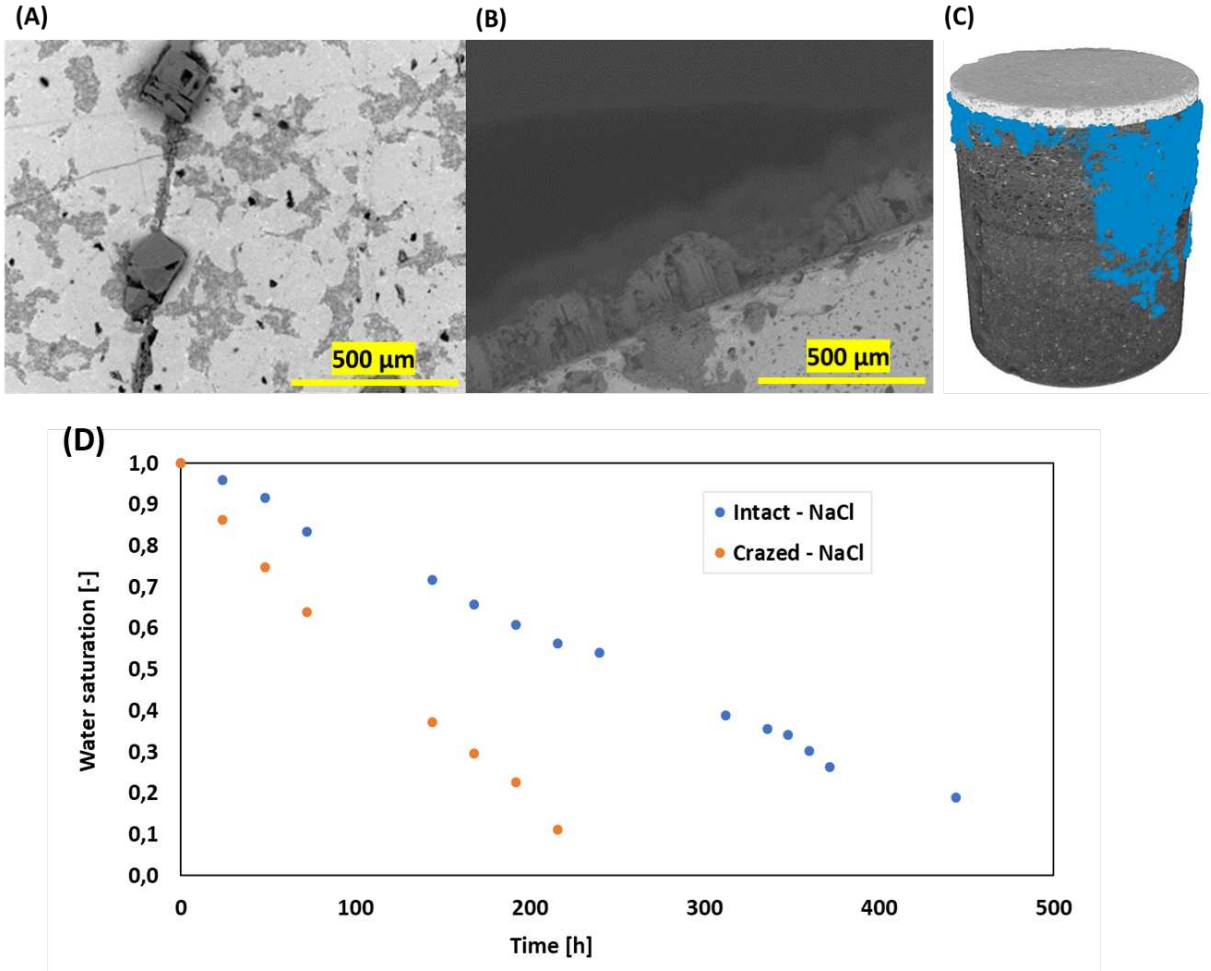

Figure 3.12: NaCl efflorescence in the weathered samples: (A) SEM image showing NaCl growth through the crazing of the sample (courtesy of Rozeline Wijnhorst), (B) SEM image showing NaCl creeping up the glaze in the intact sample (courtesy of Rozeline Wijnhorst), (C) 3D rendering of XCT scan showing NaCl efflorescence in the weathered intact sample. (D) Drying kinetics of the cylindrical samples at the fourth cycle.

The observation of the X-ray CT scans revealed salt accumulation in patchy patterns within the clay body's volume.

Figure 3.13 shows differential images obtained by subtracting the images resulting from the scan in cycle 5 from those of the initial scan before salt contamination. These differential images clearly show salt patches (the white patches). The crazed sample exhibited more subflorescence than the intact sample, consistent with our earlier findings where the intact tile displayed higher efflorescence than the crazed tile.

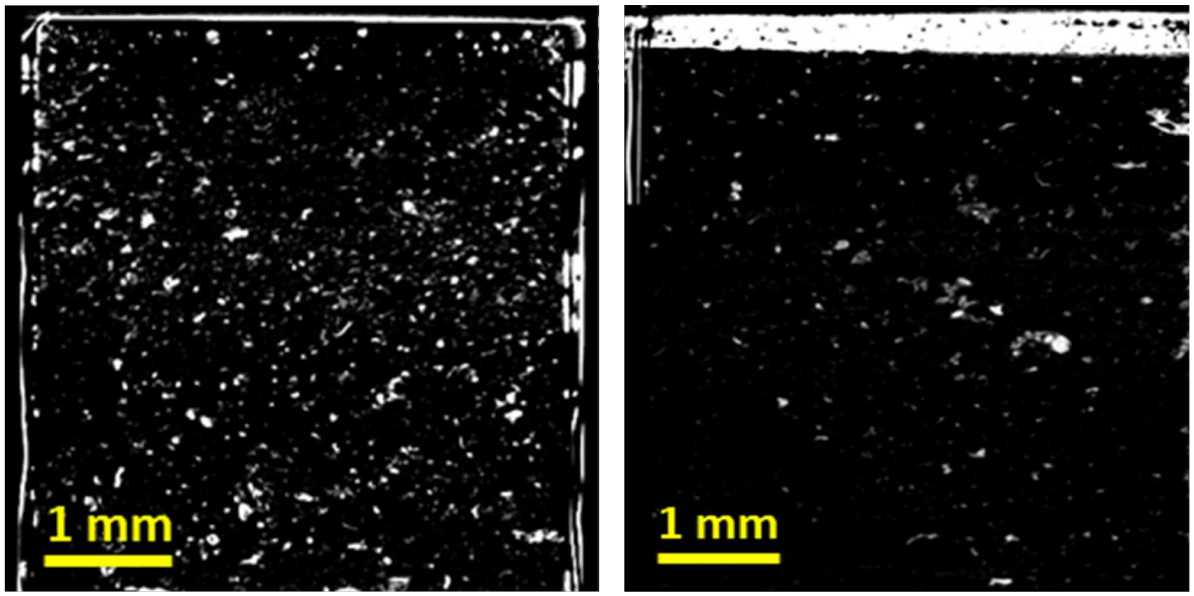

Figure 3.13: Differential images showing the distribution of NaCl inside the clay body of the cylindrical samples (white patches): (A) accumulation in the clay body of the crazed sample, (B) accumulation in the clay body of the intact sample.

The profilometer height maps revealed elevated glaze levels in both intact and crazed 2x2 cm samples, primarily near the evaporation area, which is along the sides (Figure 3.15(A)). Microcracks resulting from crystal growth were also observed in the crazing of the weathered samples. It is worth noting that, despite the absence of macroscopic damage in the case of sodium chloride exposure for the weathered cylindrical samples, an examination of the displacement profiles showed greater deformation in the intact sample, as shown in Figure 3.15(B). Although the cylindrical crazed sample initially exhibited more subflorescence, implying an expectation for deformation, the displacement profiles did not indicate any deformation in the clay body of the crazed sample, as demonstrated in 3.14.

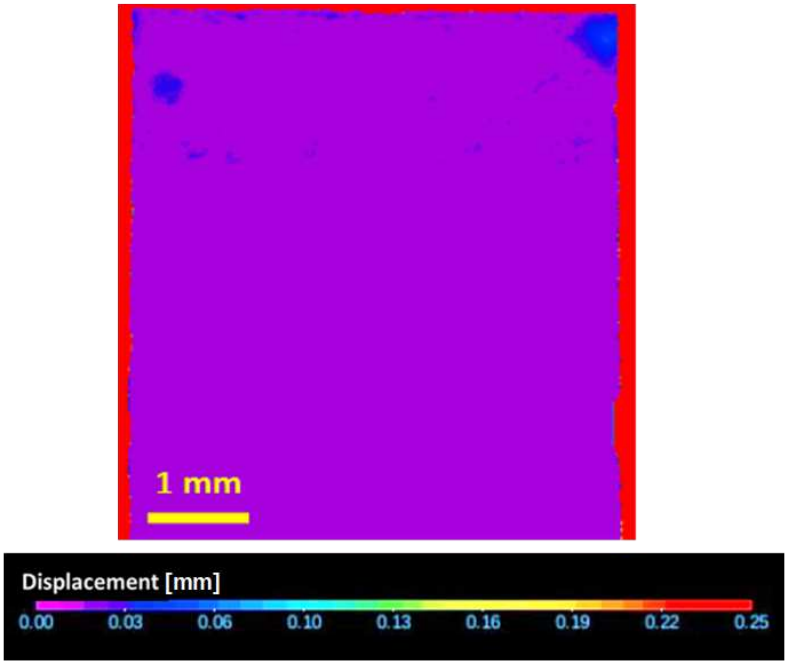

Figure 3.14: Weathering in the presence of NaCl: displacement profile of the clay body of the cylindrical weathered crazed sample.

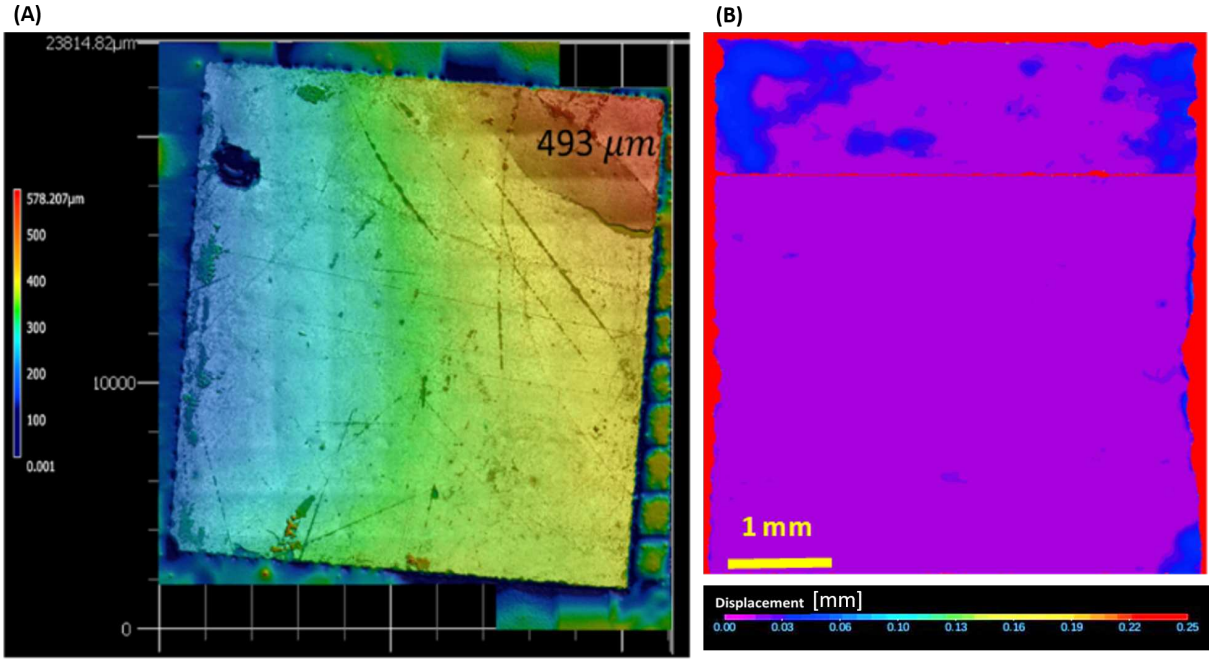

Figure 3.15: (A) Height map showing elevation in the weathered 2X2cm crazed sample (courtesy of Rozeline Wijnhorst), (B) Displacement profile of the clay body of the weathered cylindrical intact sample showing displacement near the interface between the glaze and the clay body of an order of magnitude of 0.03 to 0.06mm.

In the context of sodium sulfate weathering, minimal or no efflorescence was detected in any of the tested samples. Figure 3.16(A) displays the drying curves of the cylindrical test sample during cycle 4. In the presence of salt, we can observe that the drying kinetics exhibit similar behaviour between the intact and crazed samples. This observation further supports our earlier assertions regarding the influence of the crust on drying kinetics. In this specific case, since efflorescence was not observed, the drying kinetics appeared similar for both sample types. SEM images showed salt growth through the crazing of the 2X2cm weathered samples as shown in figure 3.16, this again indicates that the crazing was not shallow in these samples.

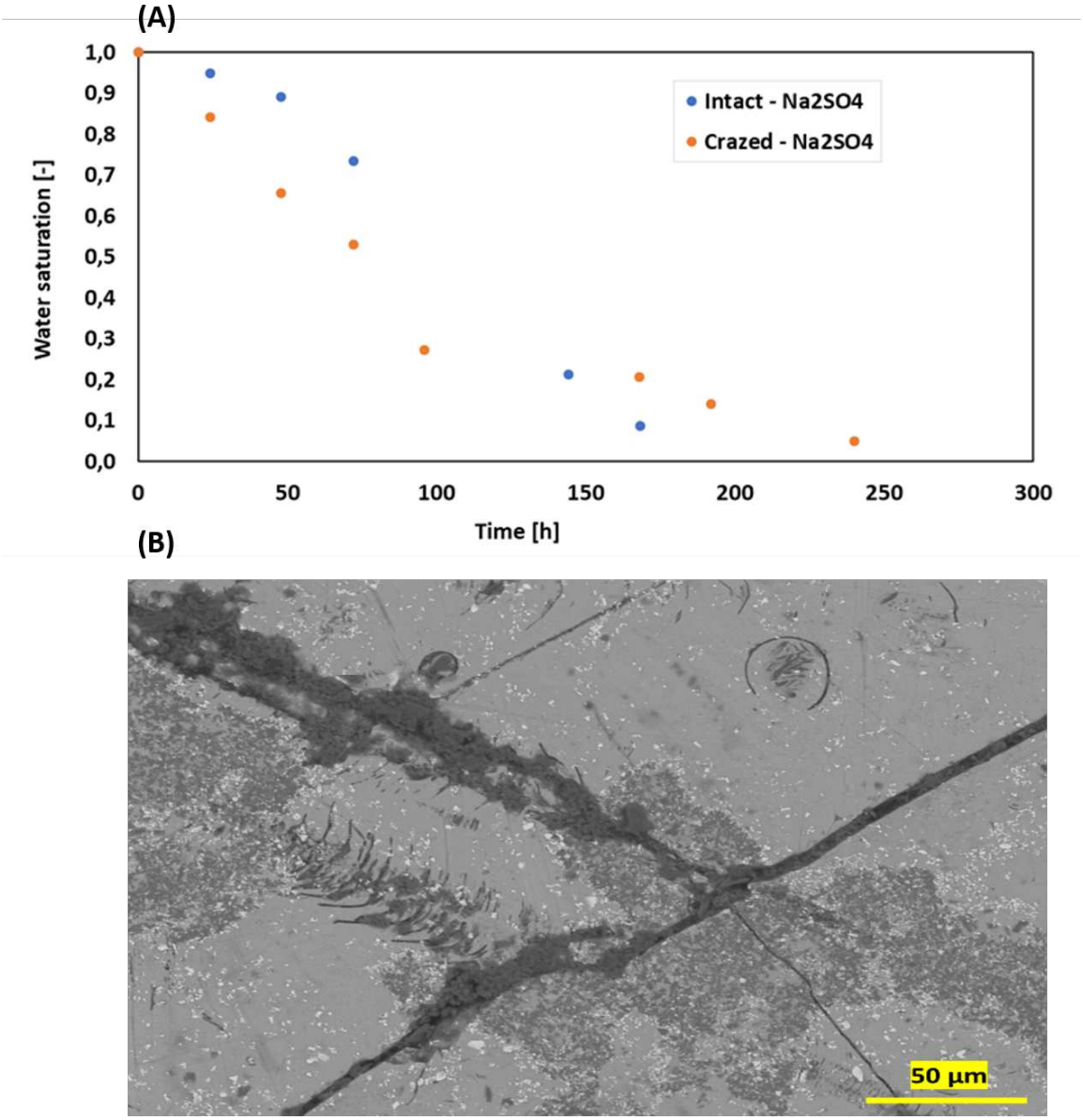

Figure 3.16: (A) drying kinetics of the cylindrical weathered samples, (B) Na2SO4 growth in the crazing of the weathered 2X2 crazed sample (courtesy of Rozeline Wijnhorst).

The X-ray CT differential images showed salt clustering near the interface between the clay body and the glaze, occurring as large salt clusters as shown in Figure 3.17. The absence of remarkable efflorescence in the case of sodium sulfate did not block the drying as we saw earlier for sodium chloride, which might explain the clustering of salt accumulation near the interface.

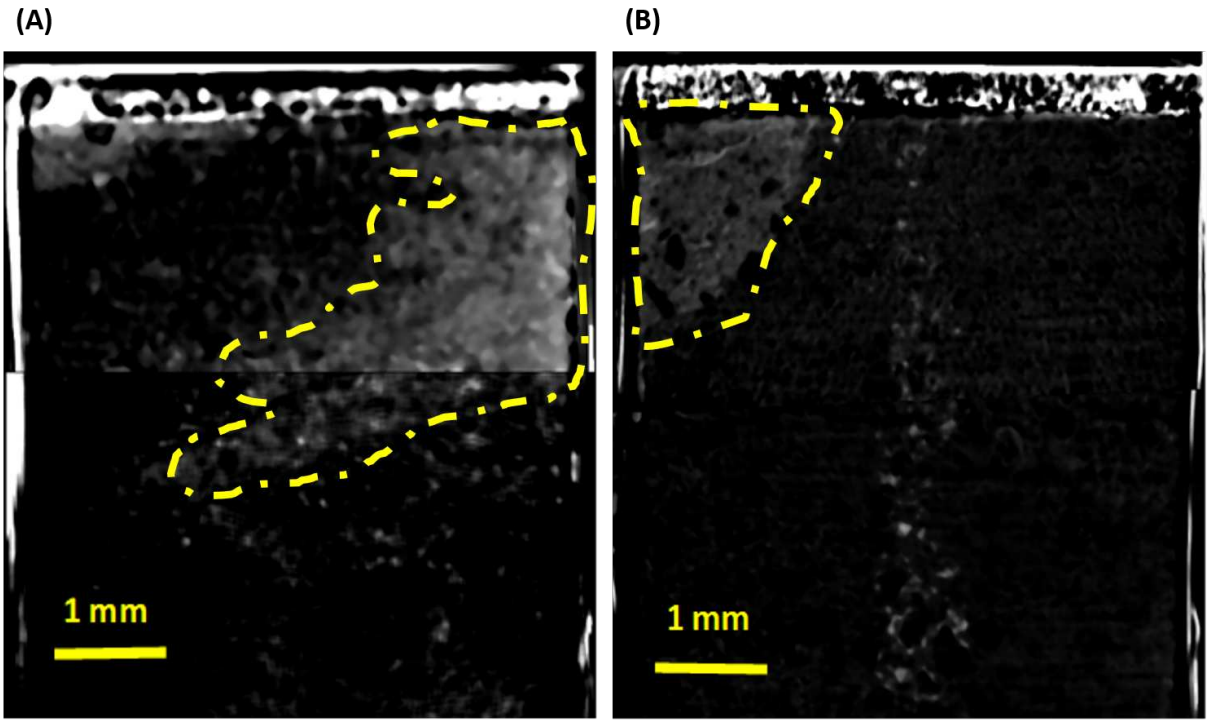

Figure 3.17: Differential images showing the distribution of sodium sulfate inside the clay body of the cylindrical sample (yellow dotted areas): (A) accumulation in the clay body of the crazed sample, (B) accumulation in the clay body of the intact sample.

All of the weathered intact samples showed macroscopic damage (the 2X2 sample and the cylindrical sample). The damage manifested in the loss of the glaze and parts of the clay body in the 2X2cm sample as shown in figure 3.18(A), and it manifested as straight cracks in the glaze of the cylindrical sample as shown in figure 3.18(B).

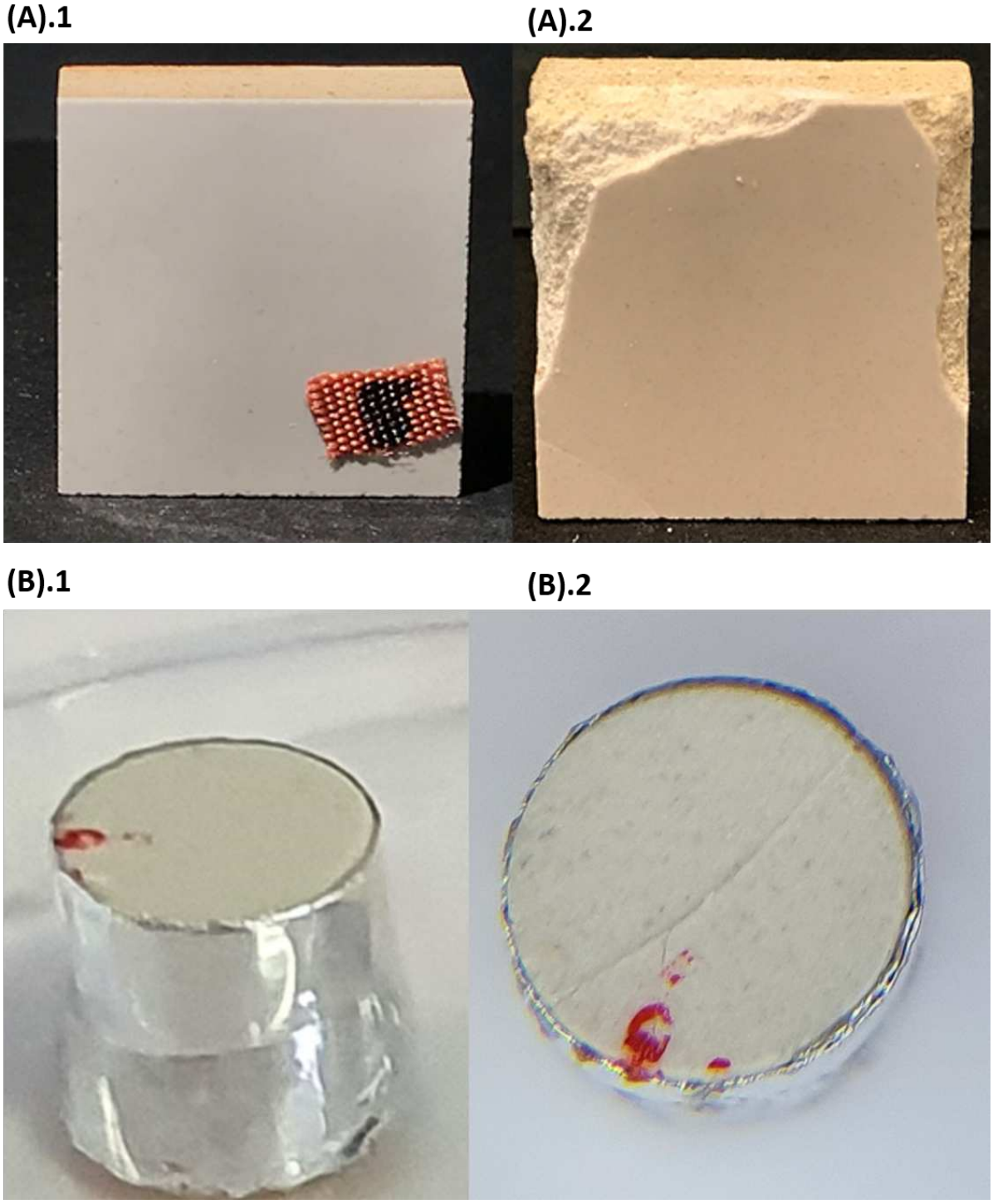

Figure 3.18: Weathering in the presence of NaCl: (A) photographs of the 2X2cm sample before weathering (A).1 and after 3 cycles of weathering (A).2 (courtesy of Rozeline Wijnhorst). (B) photographs of the cylindrical sample before weathering (B).1 and after 4 cycles of weathering (B).2.

Interestingly, although the accumulation patterns were similar in intact and crazed samples, only weathered intact tiles exhibited macroscopic damage. The height maps indicated glaze detachment in areas of increased height as shown in figure 3.19(A), while X-ray CT images identified damage in the region where displacements were already detected in the previous cycle as shown in figure 3.19(B), with damage extending through the glaze, primarily in zones where salt accumulated as we saw in the differential image above.

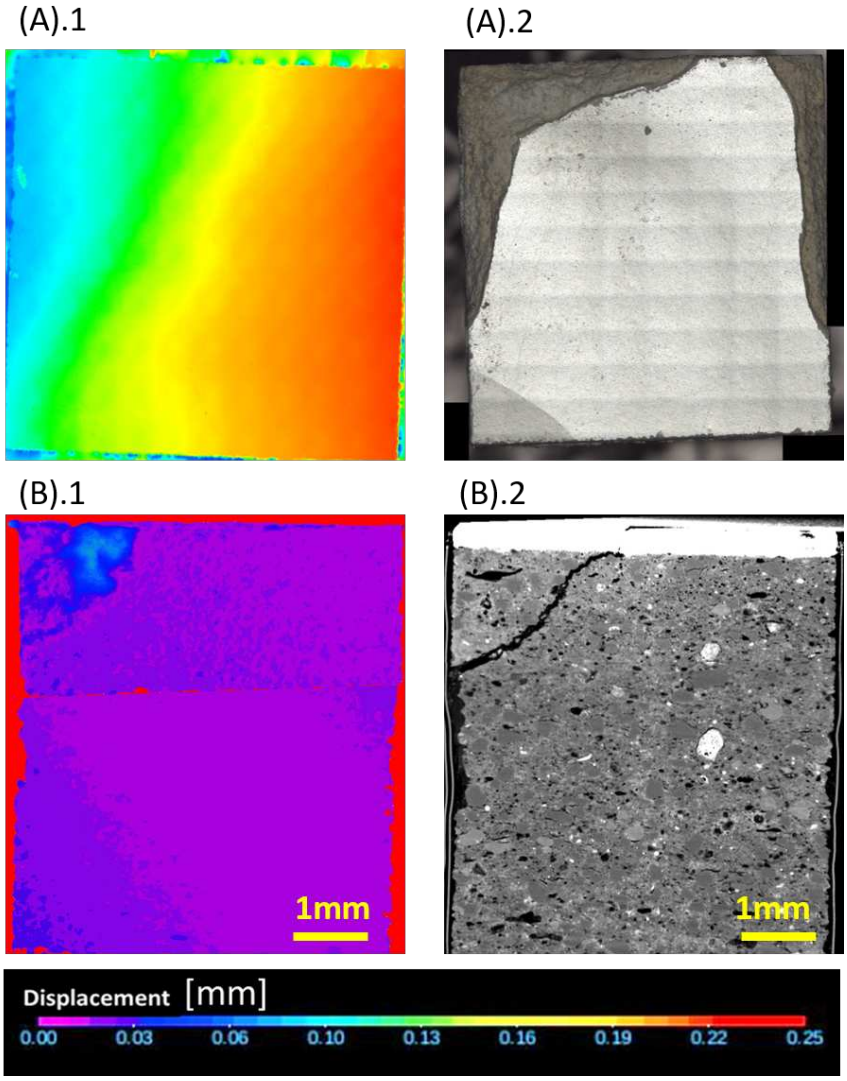

Figure 3.19: Weathering in the presence of Na_2SO_4: (A).1 height map of the 2X2cm sample after the 2^{nd} cycle (courtesy of Rozeline Wijnhorst), (A).2 height map showing the damage of the 2X2cm sample after the 3rd cycle of weathering (courtesy of Rozeline Wijnhorst). (B).1 displacement profile showing deformation in the zone where salt accumulation was detected after the 3rd cycle of weathering, (B).2 vertical cross section of the scan of the intact cylindrical sample showing damage in the zone where deformation was detected after the 4^{th} cycle of weathering.

Although the crazed samples did not manifest macroscopic damage, the height maps indicate elevations in the glaze as shown in figure 3.20(A). Also, deformation was detected in the cylindrical samples as shown in figure 3.20(B).

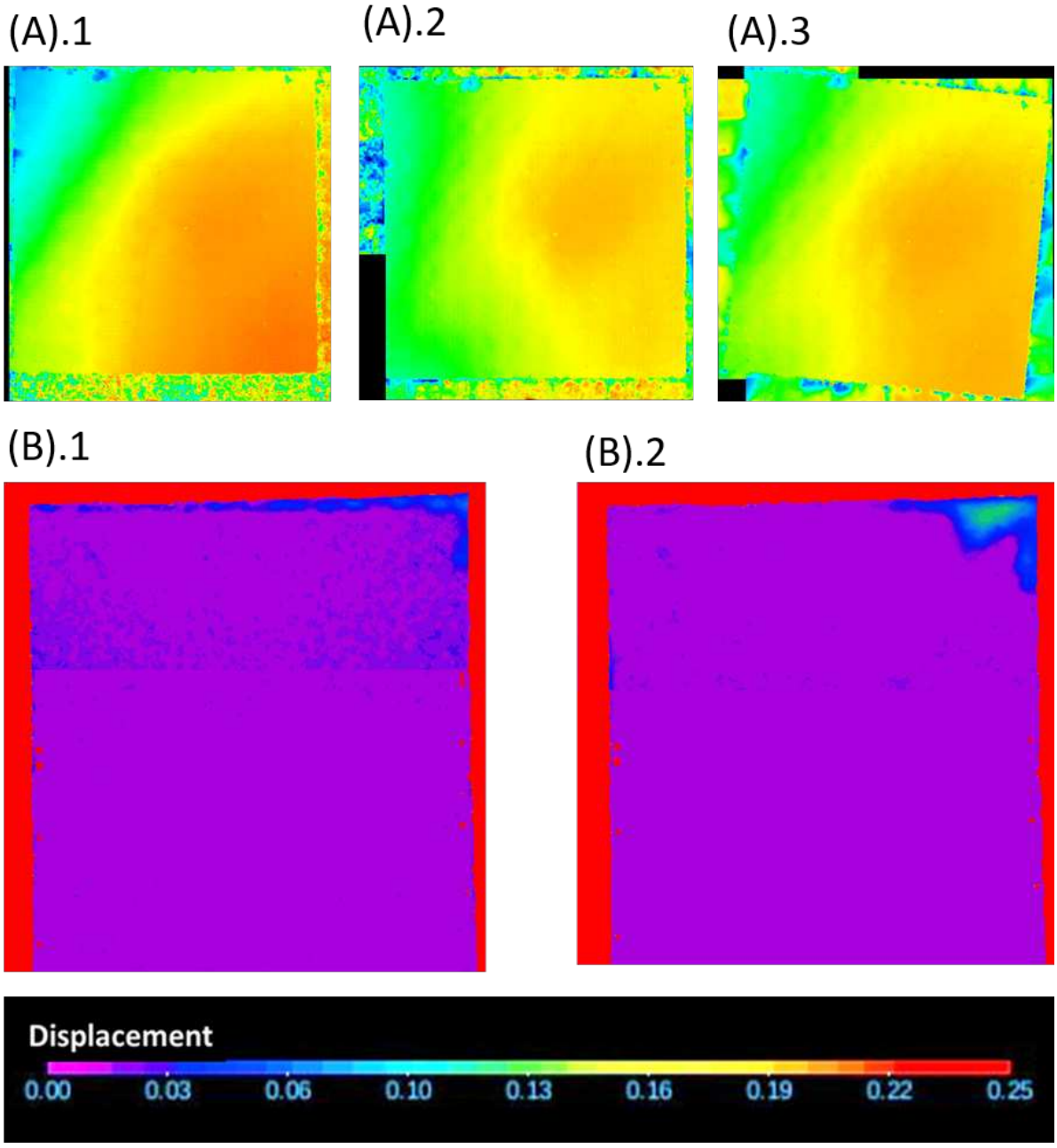

Figure 3.20: Weathering in the presence of NaCl: (A) height maps of the 2X2cm crazed sample through cycling (courtesy of Rozeline Wijnhorst), (B) displacement profiles of the crazed cylindrical sample through cycling

These results suggest that more cycling could induce macroscopic damage in these samples. Notably, not only the overall quantity of salt accumulation within the porous material, as discussed in the RILEM TC protocol, is essential for damage, but also a high localized concentration of salt in the porous media is required. In this weathering test, neither the cylindrical samples nor the 2x2 samples displayed macroscopic damage during the weathering protocol. As discussed already in the literature by Flatt [51], sodium sulfate causes damage when we have the development of high supersaturation with respect to mirabilite during the dissolution and reprecipitation process of thenardite. This explains the damage seen in the cylindrical intact samples where we intentionally kept the sample at room temperature in the 4th cycle of weathering to prolong this mechanism. This is also supported by the results of the additional experiment, where we rewetted the 2X2cm sample containing sodium sulfate with pure water, and this resulted in cracks forming quickly after rewetting the sample with water and before the recrystallization is completely finished. If we only considered this factor for damage as it was considered in the RILEM testing protocol, we would have expected macroscopic damage in the crazed samples as well when weathering with sodium sulfate. However the obtained results suggest other factors that influence the damage in these tiles. This is also true when weathering with sodium chloride, salt accumulation alone could not be the only factor for inducing damage. One other factor that could be considered is the difference in the expansion behaviours of the glaze and of the clay body. The clay body is a porous structure mainly composed of a mixture of baked clays [39, 6], so when subjected to moisture it expands, while the glaze layer is impermeable [44] and does not expand, so when the clay body expands the glaze tries to compensate by cracking [6, 14, 39, 23, 44]. This suggests that the crazed tiles are less prone to damage if only moisture expansion would be the damaging factor. Another factor that could play a role is the difference in the micro-structure of the clay bodies, where, as we saw in section 3.3.3, the fact that the clay body of the intact samples contains larger pores compared to the clay body of the crazed samples suggests a higher tensile strength for the crazed tiles, which makes the intact tiles more prone to damage.

3.4 Conclusion

This study introduced an accelerated weathering protocol that induced damage in Dutch tiles in a relatively short period (less than a month) using two types of salt, sodium chloride and sodium sulfate, a combination that was not previously achieved in the existing literature. The tested objects included tiles without macroscopic defects, and tiles with a crazed glaze, no salt was present inside the samples prior to the weathering test. The weathering test conducted in this study revealed that both sodium chloride and sodium sulfate contamination led to the accumulation of salt in the Dutch tiles over multiple cycles before showing macroscopic damage. This accumulation indicates that the designed weathering test is adequate with the previous recommendations in the literature, where in [25] the authors introduce a conceptual model for salt-induced damage in building materials, based on "induction" (salt accumulation) and "propagation" (damage) phases for defining relevant weathering protocols. The tested salts showed different accumulation patterns. Sodium sulfate showed little or no efflorescence, whereas sodium chloride showed efflorescence for all of the tested samples. The use of X-ray tomography in this work provided crucial 3D information about the spatial distribution of salt within the tested samples. Sodium chloride exhibited a pattern of accumulation in small patches throughout the samples and was distributed throughout the entire clay body volume, whereas sodium sulfate showed a clustered accumulation pattern near the interface between the glaze and the clay body. Even though the accumulation patterns are different between the two salts, the accumulation of each salt was consistent in all of the samples whether it comes from a tile with an intact glaze or a tile with a crazed glaze. This result could suggest that the type of the tile does not affect the accumulation pattern of sodium chloride and of sodium sulfate, but that rather the nature of the salt itself makes the difference. Both sodium sulfate and sodium chloride, despite their different accumulation patterns, caused damage to the Dutch tiles during the weathering protocol, damage that affected the glaze and the clay body. This shows that as we accumulate enough salt in these tiles eventually they get damaged. This is enforced by the observations made from the deformation profiles, where it showed that even when we did not get macroscopic damage, there were increasing displacements inside the tiles throughout the cycling in the region close to the interface between the glaze and the clay body. This suggests that more cycling on these samples could eventually induce damage. Damage in these tiles is a coupled problem where other factors than salt alone, like the state of the glaze, the pore size distribution of the clay body, or its hygric expansion, play a role. When coupled with salt accumulation, this makes understanding the damage in these materials complex. One perspective experimental study to simplify this complexity is the use of model porous media where we could isolate the factors that are influencing the damage and define a key factor or key factors that trigger damage in these tiles. The characterization of the material properties as well as the weathering patterns presented in this study are instrumental for designing physical and computational models, which can be utilized for in-silico studies and serve as validation for research concerning salt crystallization in building materials [16]. This type of models could be used by conservators seeking to develop more efficient conservation methods to mitigate salt crystallization damage in bi-layered porous materials such as historic tin-glazed tiles.

Chapter 4

Wettability bi-layer: application to a 3D sintered glass beads porous media

The objective of this chapter is to study fluid and salt distribution during a one-dimensional (1D) drying process of an artificially designed three-dimensional (3D) porous medium initially saturated with a salt solution. The porous medium was partially treated with a hydrophobic treatment to study the impact of the wettability difference on the drying and salt accumulation process. This study complements a parallel study conducted by PhD student Rozeline Wijnhorst at UvA, involving a 2D version of the sintered glass beads media, which comprises a single layer of glass beads confined within a rectangular glass capillary [34]. The final aim, beyond this thesis, is to allow for a comparison between the 2D and 3D processes observed, within the framework of the CRYSTINART collaboration.

Contents

4.1 Materials and methods

4.1.1 Materials

Four cylindrical samples with dimensions of 0.8 cm in diameter and 0.9 cm in height were cored from larger cylinders composed of sintered glass beads with a diameter of 250 µm. To add hydrophobicity, a treatment involving a mixture of 99% (by volume) of toluene and 1% (by volume) of n-octyl trichlorosilane was applied in order to cover approximately one-third of the volume of the samples. The samples were saturated with pure water to determine the necessary volume for achieving saturation. Subsequently, one-third of that volume, representing the hydrophobic treatment, was placed in a Petri dish. The dry sample was then placed on top to introduce the treatment through capillarity. The resulting hydrophobicity was evaluated by measuring the contact angle, which increased from 38.7° to 89.9°. The preparation of the samples as well as the silanization was performed at the University of Amsterdam by technician Gertjan Bon and PhD student Rozeline Wijnhorst. The process of the sample preparation is shown in figure 4.1.

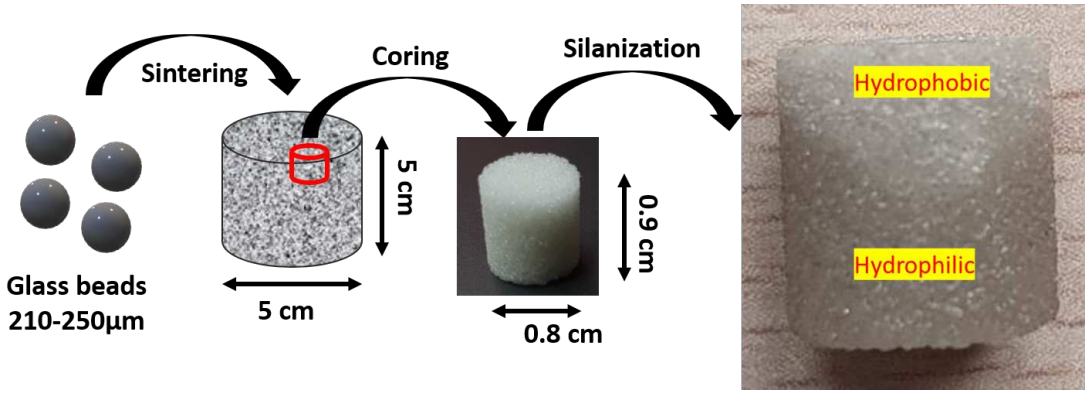

Figure 4.1: 3D artificial porous medium preparation process

4.1.2 Saturation procedure

Four samples were vacuum-saturated with different salt solutions. To achieve saturation in the 2D sample, vacuum saturation was chosen due to the fact that the hydrophobic portion cannot be saturated by capillary suction. The vacuum saturation process was employed on the 3D porous media as well. Two samples were saturated with a 5.9 molal sodium chloride solution, labeled as S1-Cl and S2-Cl. The remaining two samples were saturated with a 1.26 molal sodium sulfate solution, labelled as S1-SO and S2-SO. The saturation process involved three imbibition cycles conducted under vacuum conditions. Initially, the dry samples were subjected to a vacuum of -90 kPa for 15 minutes (refer to Figure 4.2). After this period, the respective solutions were introduced, fully immersing the samples. After 15 minutes, the vacuum was released, allowing the samples to saturate for an additional 20 minutes under restored atmospheric pressure. This process was iterated twice more due to the samples' incomplete saturation following a single cycle. Subsequently, the samples underwent weighing after each cycle, achieving a

stable weight after three cycles, thus verifying complete saturation. The concentration of the salt solutions was selected to ensure the full saturation of the samples while avoiding instantaneous crystallization, which would complicate the saturation process. On the other hand, by using undersaturated solutions, sufficient time was provided to observe the drying kinetics of the samples without encountering salt blockage.

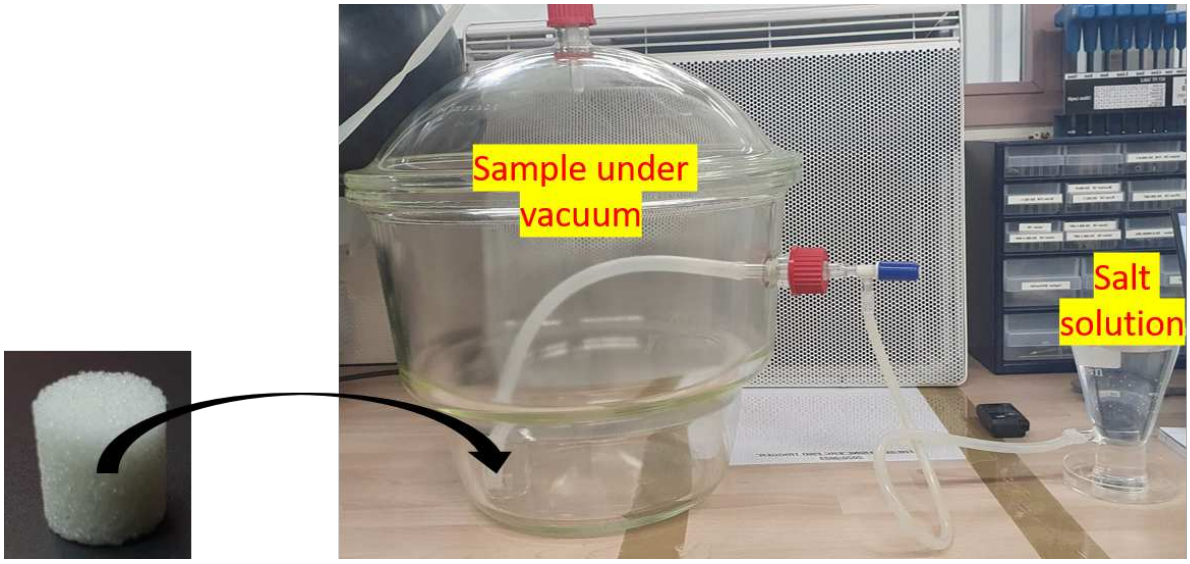

Figure 4.2: Vacuum saturation process for the four experimental samples

4.1.3 X-ray scanning procedure

In the TESCAN UniTOM XL presented in chapter 2, the initial dry state of the samples, prior to saturation, as well as their final state after drying were scanned with simple single 360° rotation scans with a voxel size of 5µm and 10µm, while the drying of the samples was scanned using continuous and time-lapse scans with a voxel size of 10µm. For each 360° rotation, an energy of 60keV and a power of 14W were applied to acquire 2879 projection radiographs with a 5µm voxel size and 1440 projection radiographs with a 10µm voxel size. An averaging of 2 projection images, taken with an exposure time of 360ms for the 5µm voxel size, and 180ms for the 10µm voxel size, was applied for each projection radiograph. The source-detector distance was set at 1000 mm, and the source-object distance was 34 mm for all of the scans. Two detector modes were used, the first resulting in projection radiographs of 1920x1896 pixels for sample S1-Cl, and the second mode producing projection radiographs of 2856x2856 pixels for the rest of the samples. No filters were required for any of the scans. The chosen parameters were selected after optimization tests, focusing on those that maximize the contrast between the different phases (air, brine, glass beads, and salt) while minimizing the scanning time, enabling us to monitor the drying and crystallization kinetics. With the given parameters, the duration for each 360° rotation was 11 minutes for a voxel size of 10µm and 38 minutes for a voxel size of 5µm. Subsequently, the acquired scans were reconstructed using Panthera software specific to TESCAN Unitom XL, using a filtered back-projection algorithm, including correction for ring artifacts and beam hardening.

4.1.4 Drying procedure

After the saturation procedure, the samples were sealed with aluminium tape, leaving only the hydrophobic upper surface open. The samples were then subjected to a 1D drying process by placing them in a controlled environment, for which different types of setups were employed as described below. The drying history of each sample, detailing which setups were used with which sample, is summarized in section 4.1.4.4.

4.1.4.1 X-ray micro-tomography - in-situ drying

After saturating the samples with the salt solutions, they were placed in the conditioned chamber inside the TESCAN Unitom XL scanner as explained in chapter 2, as shown in Figure 4.3. A constant temperature of 25°C and a relative humidity of 50% is maintained.

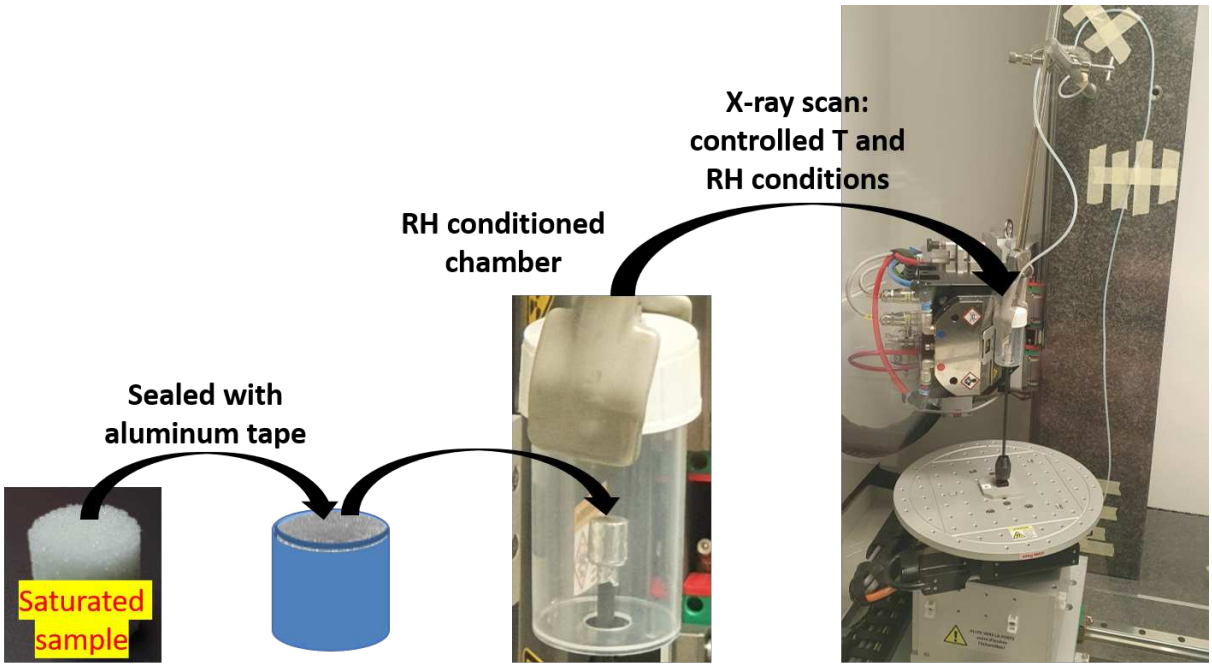

Figure 4.3: Conditioned chamber inside the scanner

4.1.4.2 Balance - in-situ drying

The saturated samples were placed on a Mettler Toledo XRE205 DeltaRange balance with an accuracy of d=0.01 mg for masses below 81g to continuously measure their mass while drying, capturing data at a rate of three measurements per second. The samples were kept in the conditioned chamber to ensure controlled relative humidity during the drying process. The apparatus is shown in figure 4.4.

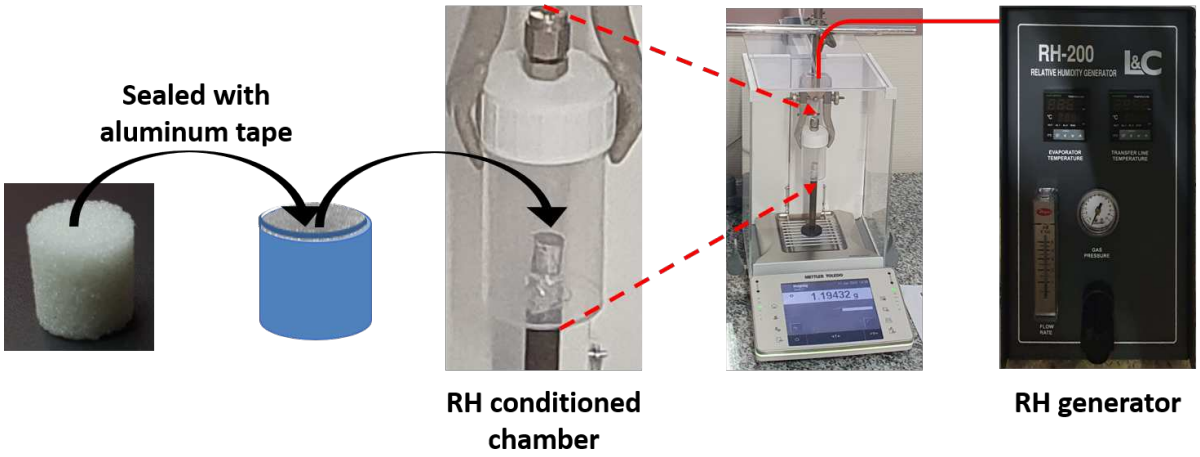

Figure 4.4: Conditioned chamber - balance apparatus

4.1.4.3 Climatic chamber - drying

Using a WEISS C34/40 climatic chamber, the samples were allowed to dry in controlled conditions of relative humidity and temperature. Since this drying apparatus does not permit continuous weighing of the samples, the weight of the samples was measured outside the climatic chamber using the Mettler Toledo XRE205 DeltaRange balance at least three times throughout the day to monitor the drying progress.

4.1.4.4 Drying configuration of each sample

Sample S1-Cl:
The sample S1-Cl was vacuum saturated with a 5.9 molal sodium chloride solution. Subsequently, the sample was dried in the scanning drying apparatus using 50% relative humidity. It was continuously scanned for 2 hours and 30 minutes, totaling 18 scans. Then, it was scanned in time-lapse mode for 22 hours and 30 minutes, comprising 50 scans with a 7-minute pause between each rotation. Following this, the sample was left in the conditioned chamber but outside the scanner to complete the drying process at 50% relative humidity and laboratory temperature of 22°C.
Sample S2-Cl:
The sample S2-Cl was initially vacuum saturated with pure water. It was then dried continuously in the balance apparatus at 50% relative humidity and a laboratory temperature of 22°C. Subsequently, the sample was vacuum saturated with a 5.9 molal sodium chloride solution and allowed to dry in the same balance apparatus. The drying process was intermittently interrupted for a scan in the TESCAN scanner. These scans consisted of a single rotation and were conducted under the scanner's conditions. The scanning frequency was determined based on the sample's drying kinetics. In total, 10 scans were performed with a frequency of three scans per day, with approximately three hours between each scan.

Sample S1-SO:
The sample S1-SO was initially vacuum-saturated with pure water. It was then dried continuously in the balance apparatus at 50% relative humidity and a laboratory temperature of 19°C. The change in laboratory temperature occurs as a result of energy-saving measures, with temperatures shifting from 22°C in the summer season to 19°C in the winter season. Subsequently, the sample was vacuum-saturated with a 1.26 molal Na_2SO_4 solution and left to dry in the scanner apparatus at 50% relative humidity and the scanner's temperature. It was continuously scanned for three hours, totalling 20 scans. Then, it was scanned in time-lapse mode initially for 21 rotations with a 7-minute pause between each rotation, followed by 10 rotations with a 35-minute pause between each rotation, and finally, 20 rotations with a 90-minute pause between each rotation, totalling 48 hours of time-lapse scanning. At the end of the scanning period, the sample was transferred to the WEISS climatic chamber apparatus, where it was allowed to dry under the same conditions of 50% relative humidity and 25°C. During this phase, weight measurements were taken intermittently until the sample was completely dry.
Sample S2-SO:
The sample S2-SO was initially vacuum saturated with pure water. It was then dried continuously in the balance apparatus at 50% relative humidity and a laboratory temperature of 22°C. Subsequently, the sample was vacuum saturated with the 1.26 sodium sulfate solution and allowed to dry in the same balance apparatus. The drying process was intermittently interrupted for a scan in the TESCAN scanner. These scans consisted of a single rotation and were conducted under the scanner's conditions. The scanning frequency was determined based on the sample's drying kinetics. In total, 8 scans were performed with a frequency of three scans per day, with approximately three hours between each scan.

As will be presented in section 4.2, different drying behaviour was observed between samples S1-SO and S2-SO, prompting us to assess the experiment's repeatability. For the S1-SO sample, a vacuum cleaning process was performed using pure water at 50°C. Multiple cycles were performed on the sample, with water being replaced for each cycle. The sample's weight was monitored, and the cycling process was terminated once a stable weight was attained. Subsequently, the sample was placed in a 250ml beaker on a heat source and left immersed in 50°C water overnight. Following this step, the sample was dried and then saturated with a 1.26 molal sodium sulfate solution. The sample was then positioned on the balance apparatus at 39% relative humidity and 22°C and dried continuously. A scan was conducted immediately after saturation and at the end of the drying process. At the end of the drying process, the sample underwent a second cleaning using the same procedure as the previous cleaning step. It was then saturated with pure water and allowed to dry on the balance apparatus at 50% relative humidity and 22°C to investigate whether the cleaning process had any impact on the drying behaviour of the sample. Following this, the sample was saturated once again with the same salt solution (1.26 molal sodium sulfate) and subsequently dried continuously on the balance apparatus under conditions of 50% relative humidity and 22°C. A scan was performed immediately after saturation and at the end of the drying process.

4.1.5 Image analysis

The data obtained from the X-ray computed tomography was analysed using Dragonfly software (Version 2022.1 and 2022.2 for [Linux]. Comet Technologies Canada Inc., Montreal, Canada; software available at https://www.theobjects.com/dragonfly). The primary focus was to extract both qualitative and quantitative information on structural properties of the samples, on drying kinetics, and on salt accumulation.

4.1.5.1 Structural properties

The porosity of the samples was determined through image analysis. The 5µm initial scan of each sample was first filtered using the median filter in order to remove any potential noise in the images as shown in figure 4.5. After that, the grey value interval of the glass beads and the air phase was determined through the histogram of the images as shown in figure 4.6. The air phase was then segmented through global thresholding as already explained in chapter 2 in section 2.2.1.6, resulting in binary images that allow the creation of a mask on the air space and a mask on the glass beads as shown in figure 4.6. Next, the morphological closing operation was applied to the mask of the glass beads in order to include all of the porosity. Upon completion of this operation, we were left with a mask that covered the entire sample, as depicted in the figure. 4.7. In order to determine the porosity of each sample, the volume of the masks was calculated in the software, then the porosity was calculated using equation 4.1.

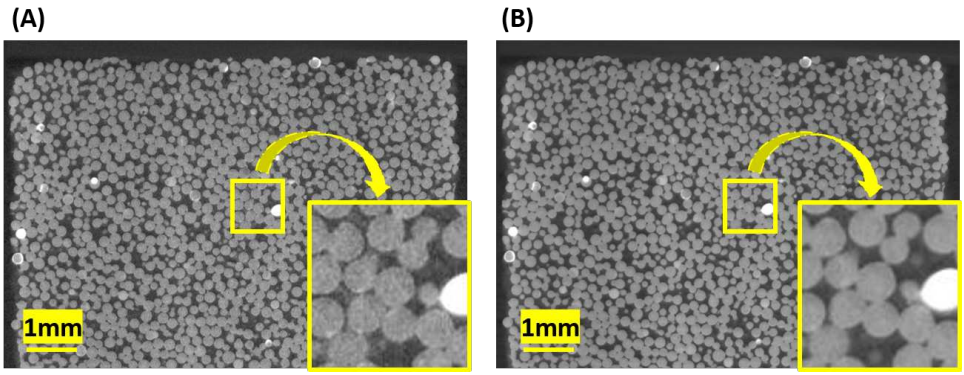

Figure 4.5: Vertical cross sections of the sample S1-Cl: (A) raw image, (B) filtered image

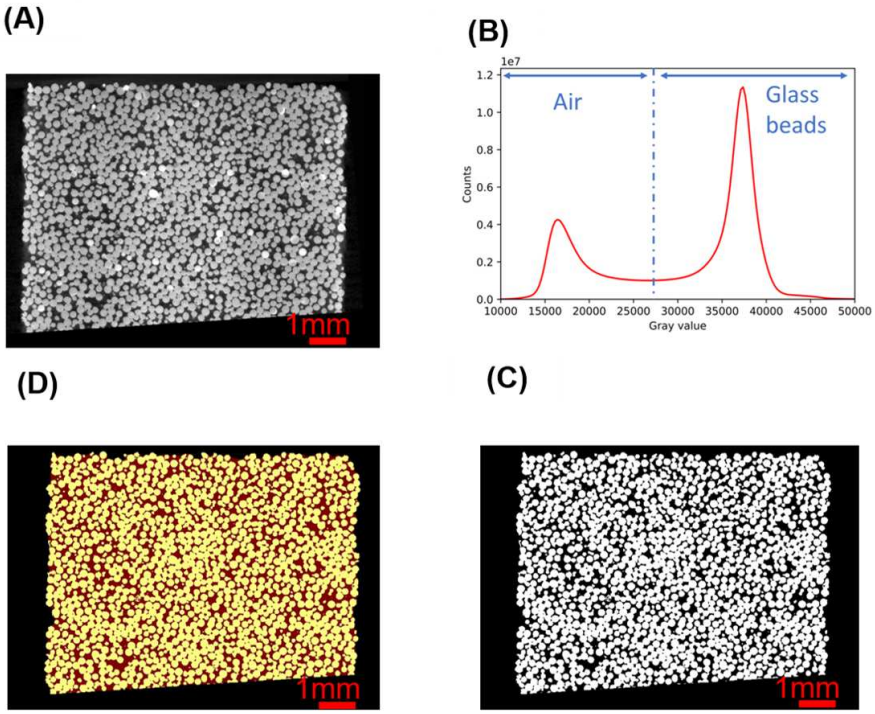

Figure 4.6: Vertical cross sections of the sample S1-Cl: (A) filtered image, (B) global thresholding from the histogram, (C) binary image resulted from global thresholding, (D) masks on the pore space in red and on the glass beads in yellow created from the binarization of the filtered image

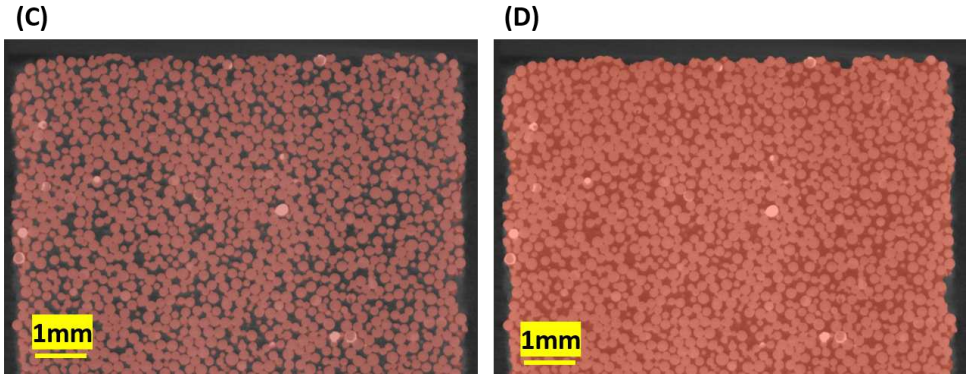

Figure 4.7: Vertical cross sections of the sample S1-Cl: (A) mask on the glass beads, (B) mask encompassing the glass beads and the pore space created using the morphological operations

$$\phi = \frac{V_{air}}{V_{total}} \tag{4.1}$$

Where ϕ is the porosity, V_{air} is the volume of the air phase, and V_{total} is the total volume of the sample, corresponding to the mask defined above.

To distinguish between the hydrophobic and hydrophilic parts, we employed the following method: The samples underwent capillary saturation with pure water, being immersed in water and periodically weighed until a stable weight was achieved. Subsequently, the sample was completely sealed with aluminium tape and scanned using the TESCAN UniTOM XL in a single 360°C rotation, using parameters identical to the initial scans on the dry sample, with a voxel size of 10µm. The resulting images were analyzed. The water volume within the sample was segmented using morphological operations. Similar to creating the mask for the entire sample volume, a mask for the volume containing water (representing the hydrophilic part) was generated. The hydrophobic part's volume was defined by subtracting the hydrophilic part's mask from the total sample volume's mask.

For sample S1-Cl, the approach to defining the hydrophobic and hydrophilic parts differed. This variation arose due to the absence of a scan during capillary saturation before contaminating the sample with the salt solution. The hydrophobic volume was linked to the section of the sample that dried first when saturated with the salt solution. This assumption was supported by results obtained from 2D porous media, where, in the case of saturation with a sodium chloride solution, the hydrophobic part dried first.

4.1.5.2 Drying kinetics and subflorescence

To assess changes in brine volume and subflorescence volume during drying experiments in the scanner apparatus for samples S1-Cl and S1-SO, an automated procedure was devised to handle the substantial volume of acquired data. All of the scans acquired during the drying of S1-Cl and S1-SO were first filtered using a median filter in 3D with a kernel size of 3. After that, a workflow was developed to process individual scans. This workflow was then applied in an iterative way to all acquired scans to acquire the complete salt and brine volume change over the entire scanning period. The implementation was facilitated through the use of the macro builder tool, which enabled the creation of a code to analyze all acquired scans and extract the requisite data. The selection of the base scan for constructing the individual analysis workflow involved scans that captured both brine, accumulated salt, and air. In the case of sample S1-Cl, the contrast was sufficiently pronounced, primarily attributable to the attenuation characteristics of sodium chloride, enabling clear differentiation between the brine phase and the air phase.

However, distinguishing between the glass beads and the accumulated salt was not possible as shown in figure 4.8. To address this limitation, a mask was generated to isolate the pore space from the rest of the system, focusing the analysis solely within the pore space. This approach streamlined the analysis, making it easier to distinguish between precipitated salt, brine, and air phases within the pore space. The corresponding histogram is presented in figure 4.9. To quantify the volumes of the subflorescence and the brine, global thresholding was used. Initially, the grey value interval corresponding to the brine and to the salt was determined from the histogram. Subsequently, a binary image was generated and its volume was calculated. This process was then incorporated into the created code to obtain the brine and the subflorescence volumes throughout the scanning duration. It is important to mention that the image analysis of the brine drying and the salt subflorescence considered only what is present inside the mask created on the pore space.

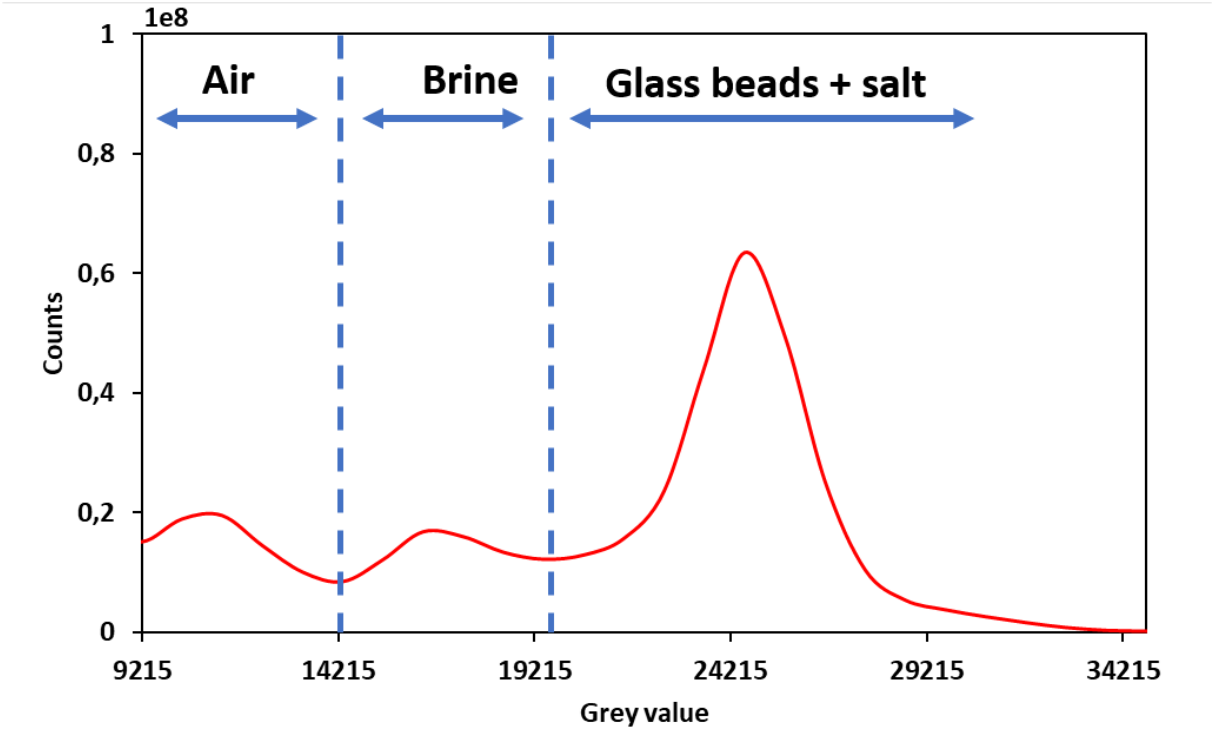

Figure 4.8: Histogram of reconstructed volume of the sample S1-Cl at a late stage of drying

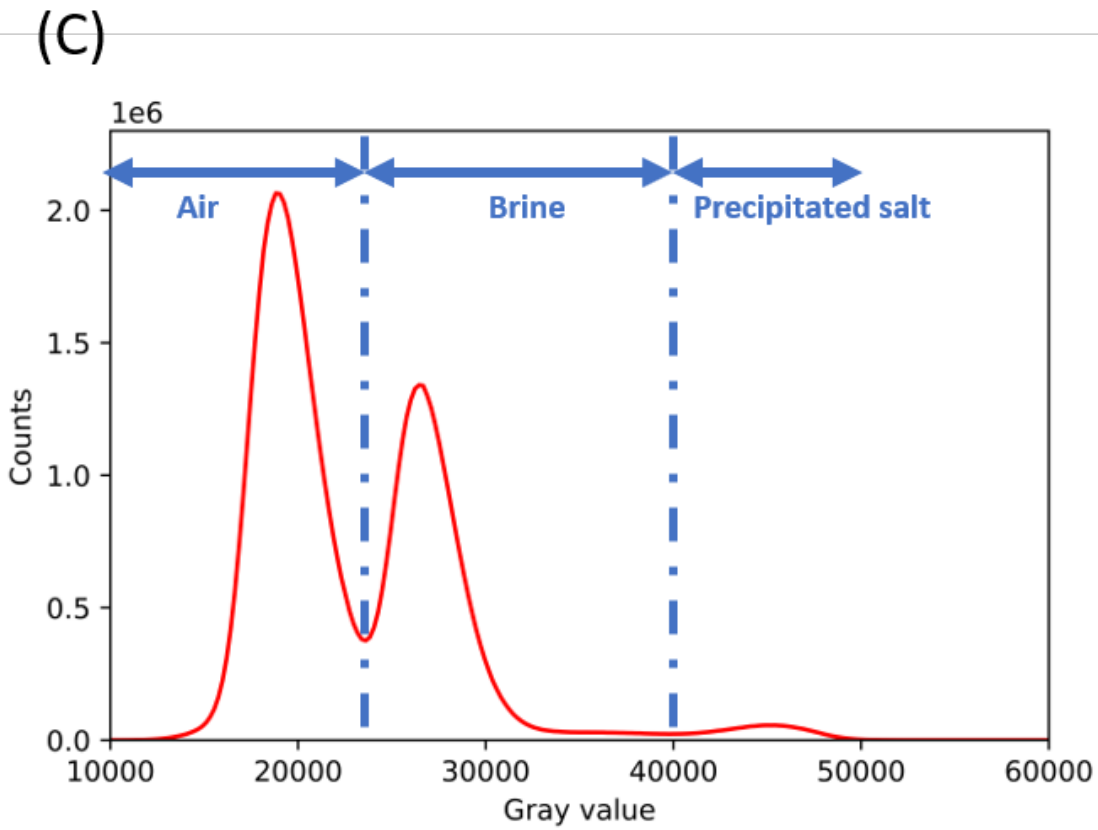

Figure 4.9: Histogram of the pore space of the sample S1-Cl

In the case of sample S1-SO, the low attenuation properties of sodium sulfate prevented differentiation between the brine and precipitated salt phases, as depicted in figure 4.10. In this case, we opted for the use of differential imaging to obtain quantitative data on the change in brine and subflorescence volumes during the drying process. The initial step in this analysis involved quantifying the initial brine volume. To achieve this, we segmented the brine in the first saturated scan using a global thresholding technique since we could successfully distinguish between the brine and air phases. Subsequently, within the analysis workflow, we subtracted the filtered data set obtained from the initial saturated scan at time t_0 from the filtered data set obtained from a scan at a later time t, where t > t_0. The resulting differential image was further refined by applying a median filter to reduce potential noise artifacts, using a kernel size of 5. The histogram of the resulting differential image is shown in figure 4.11. From these differential images, we were able to quantify both the brine and potential precipitated salt through also global segmentation. Negative values in the differential images indicated the disappearance of brine, while positive values indicated the presence of precipitated salt. The brine volume was determined by subtracting the segmented disappearing volume from the initial brine volume.

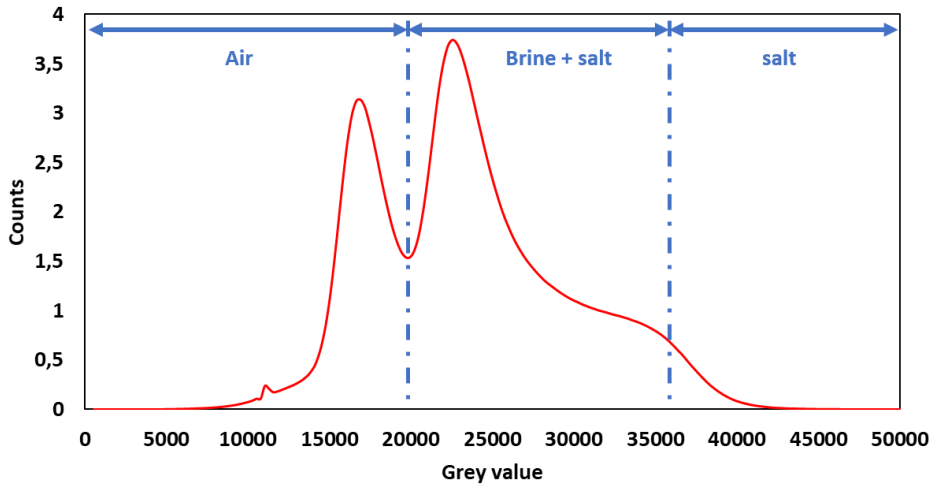

Figure 4.10: Histogram of the pore space of the reconstructed volume of the sample S1-SO at a late stage of drying

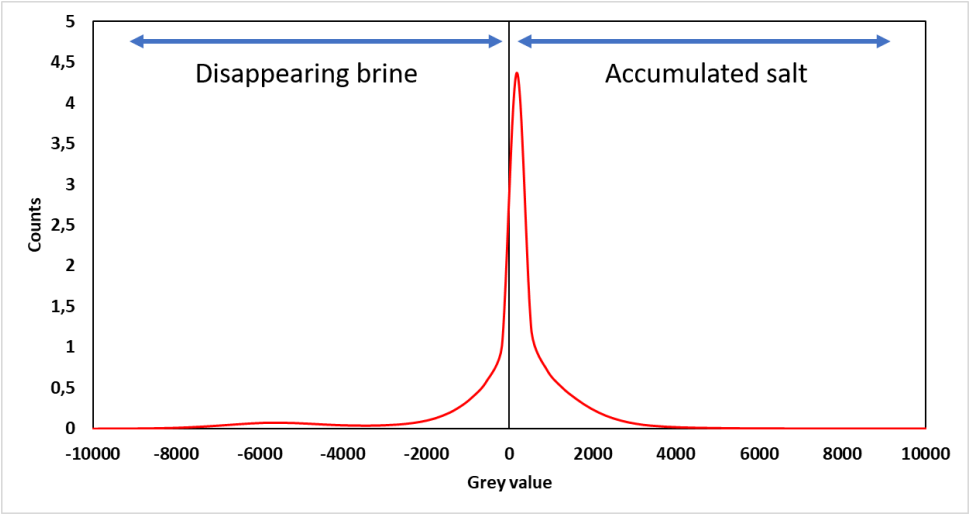

Figure 4.11: Histogram of the differential image showing the accumulated salt and the disappearing brine inside the sample S1-SO

4.1.5.3 Efflorescence

To quantify the efflorescence volume variation throughout the drying process, a mask was generated using the initial scan of the sample structure, covering both the glass beads and the pore space. Subsequently, additional masks were created to cover the sample and the efflorescence in subsequent scans during the drying process. The efflorescence volume was determined by subtracting the volume of the initial scan mask from the volume of the masks at time t.

4.2 Results and discussion

4.2.1 Structural analysis

The average porosity of the four samples was determined to be 24% ±3%. The calculated porosity was observed to be lower than the theoretical expectation for a pack of spheres, which is typically assumed to be around 36% according to [32]. The deviation from this expected porosity level can be attributed to the presence of debris within the created porous media, as illustrated in figure 4.12. This debris, located within the pore space, is assumed to be responsible for the observed lower porosity.

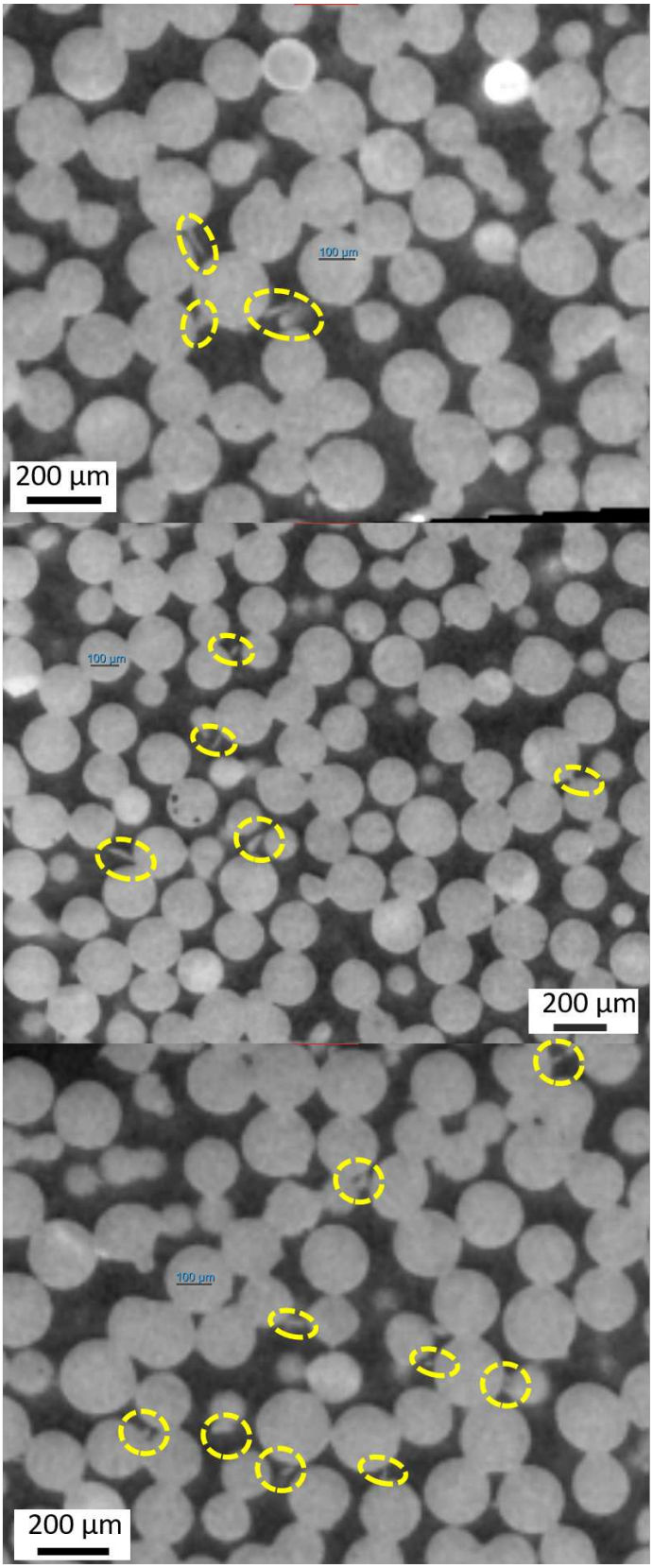

Figure 4.12: Vertical cross section of the reconstructed volume of the model porous media showing debris in the pore space

4.2.2 Drying and accumulation in the presence of NaCl

4.2.2.1 Drying kinetics and salt accumulation - sample S1-Cl

Through image analysis of the scans conducted on the S1-Cl sample, which was saturated with a 5.9 molal sodium chloride solution, we were able to track the evolution of the brine volume over time. This analysis enabled us to quantify the changes in brine volume for both the hydrophobic and hydrophilic regions of the sample separately. In the case of this sample, it's important to note that our scanning covered only 62% of the total sample volume. When examining the final scan at the end of the time-lapse scanning, we observed that the lower part of the scanned volume was not dry yet as shown in figure 4.13. In light of this observation, we made the assumption that the non-scanned portion of the sample retained its saturation with brine at that specific time point.

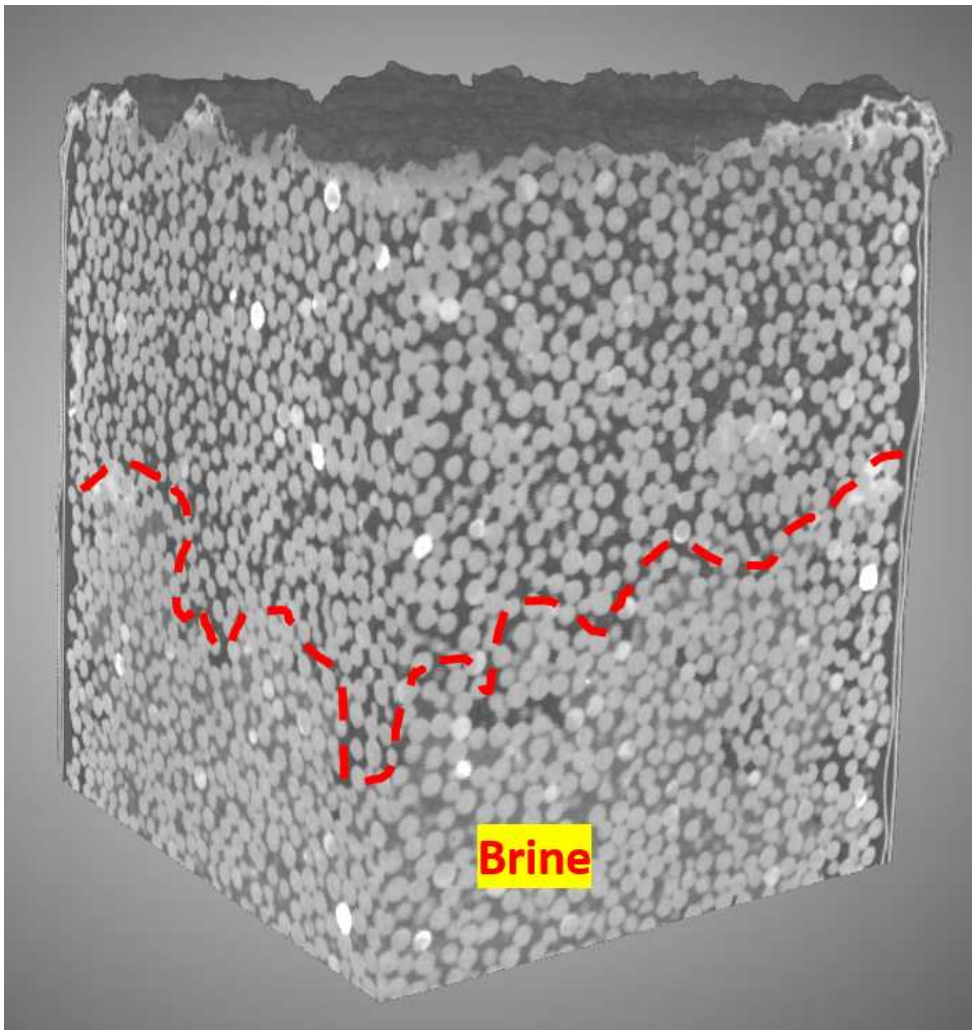

Figure 4.13: 3D reconstructed volume of the sample S1-Cl at the end of the time-lapse scanning

Figure 4.14 provides a comprehensive depiction of the temporal evolution of brine variation in the hydrophobic part, hydrophilic part, and the overall drying process of the sample. The graph illustrates how the saturation of each considered volume changes over time, with saturation values calculated as detailed in equations 4.2, 4.3, 4.4. To differentiate between the two regions and facilitate their analysis, a two-step process was employed. Firstly, a mask was generated to cover the pore space within what was considered the hydrophobic part of the sample, and secondly, another mask was created for the hydrophilic part, covering its pore space.

$$S_{bic} = \frac{V(t)_{bic}}{V(total)_{bic}} \tag{4.2}$$

$$S_{lic} = \frac{V(t)_{lic}}{V(total)_{lic}} \tag{4.3}$$

$$S_{sample} = \frac{V(t)_{sample}}{V(total)_{sample}} \tag{4.4}$$

Here, S_{bic} represents the saturation of the hydrophobic portion, while V(t)bic denotes the brine volume at the time (t) in the hydrophobic section, and V(total)bic signifies the initial total brine volume introduced into the hydrophobic part. Similarly, S_{lic} signifies the saturation of the hydrophilic region, and S_{sample} denotes the overall saturation of the sample. These saturation values were calculated following the same methodology used for determining the saturation of the hydrophobic part.

The drying process can be divided into three distinct stages based on the change in the drying slope: the initial phase (A) characterized by a steep drying slope, where we had the exclusive drying of the hydrophobic part; stage (B), with no discernible changes in the drying curves and drying slopes of zero for both the hydrophobic and hydrophilic parts; and stage (C), which marks the commencement of drying for the hydrophilic part and is characterized by a low drying slope. The hydrophobic part was not dried completely, this observation will be explained further in chapter 5. The sample was completely dry after approximately 60h.

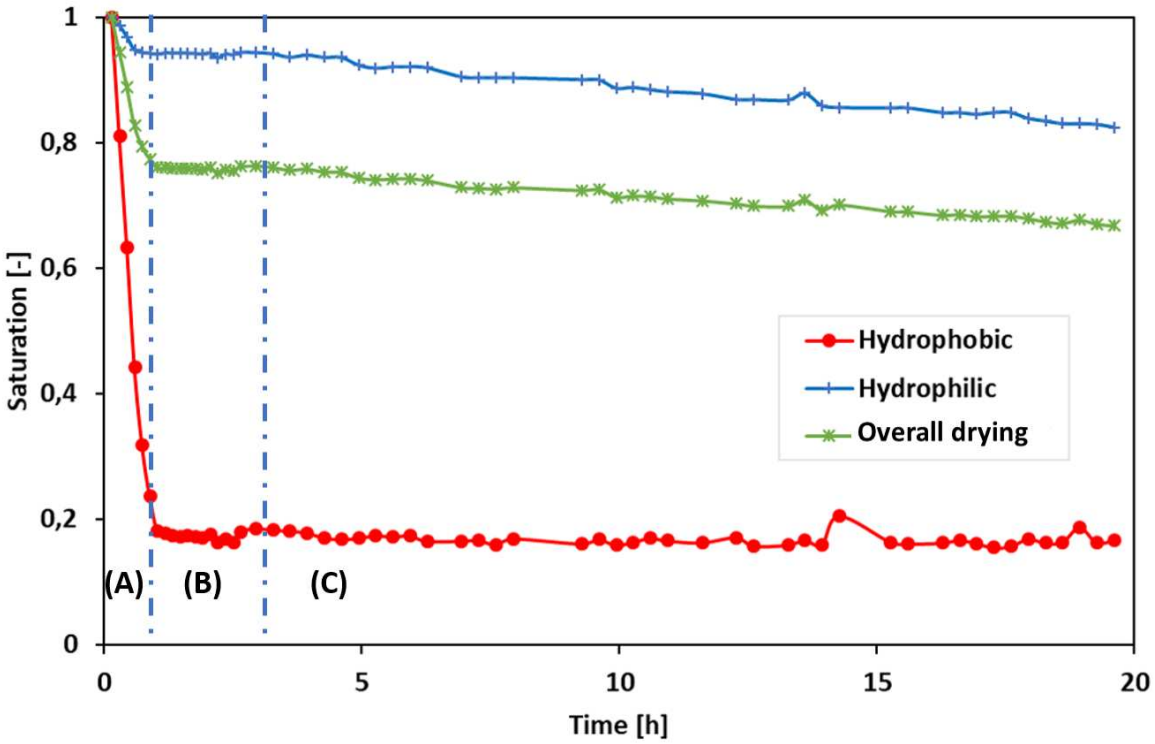

Figure 4.14: Drying kinetics of the sample S1-Cl - scanner apparatus

The evolution of accumulated salt volume over time was closely examined through image analysis, allowing for detailed quantification of changes in the accumulated salt inside the sample as subflorescence and outside the sample as efflorescence. Figure 4.15 offers a visual representation of this analysis, showing the evolution of salt efflorescence, salt subflorescence, and brine saturation throughout the scanning period. Salt accumulation represents the volume of salt accumulated at time t divided by the total volume of salt accumulated at the end of the scanning period. During the initial drying stage (A), we observed the formation of efflorescence and accumulation just below the surface of drying which represents the accumulation shown as subflorescence in figure 4.15 during this stage. In stage (B), there was a notable absence of salt accumulation in the two forms, efflorescence and subflorescence. Subsequently, at stage (C), subflorescence began to form while efflorescence stopped developing. The subflorescence was mainly formed at the interface between the hydrophobic and the hydrophilic part as shown in figure 4.16. However, at the end of the drying, it was observed that there was some salt creeping from the hydrophilic part to the hydrophobic part as shown in figure 4.17.

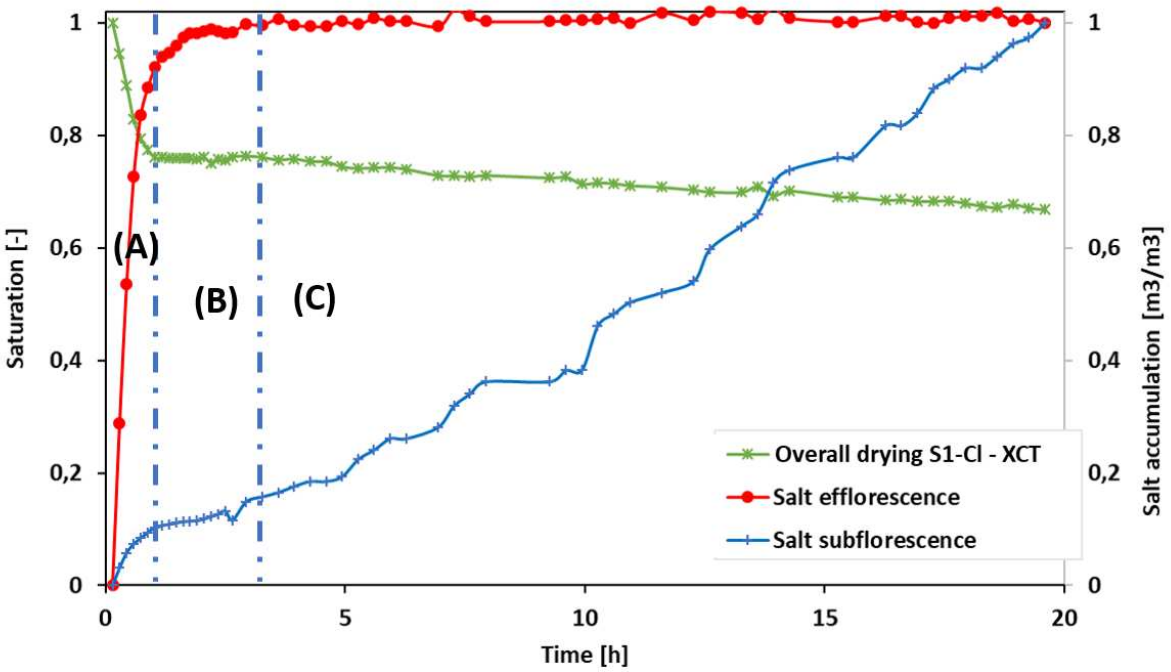

Figure 4.15: Salt accumulation kinetics of the sample S1-Cl - scanner apparatus: efflorescence represents accumulation outside the sample, subflorescence represents accumulation inside the sample

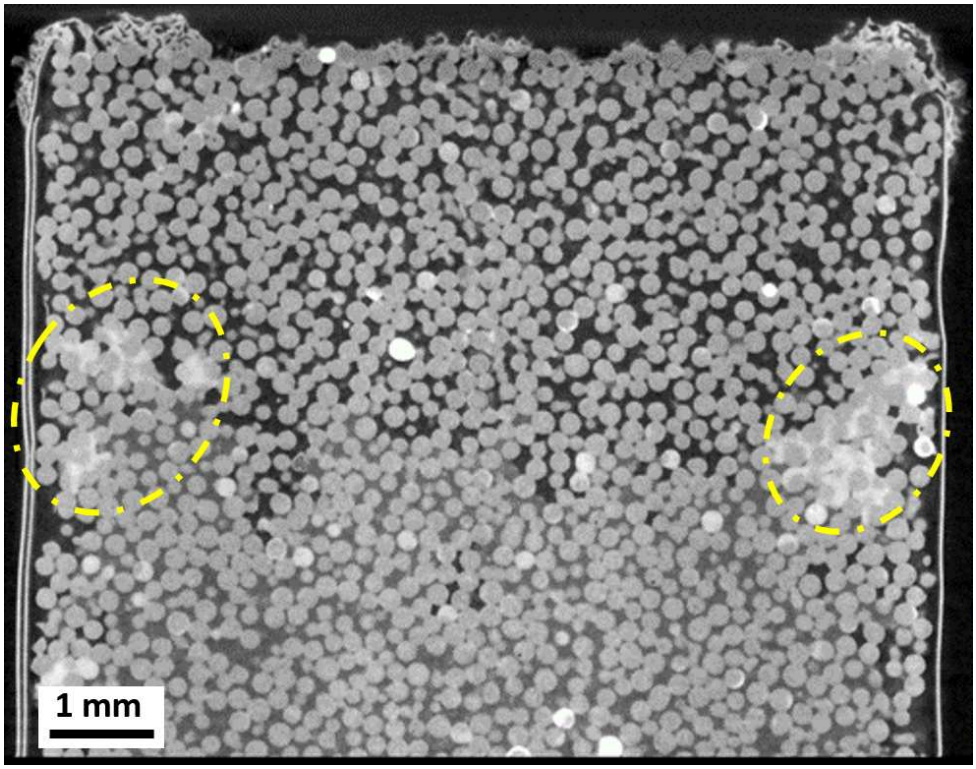

Figure 4.16: Vertical cross section of the reconstructed volume of the sample S1-Cl showing salt accumulation in the sample

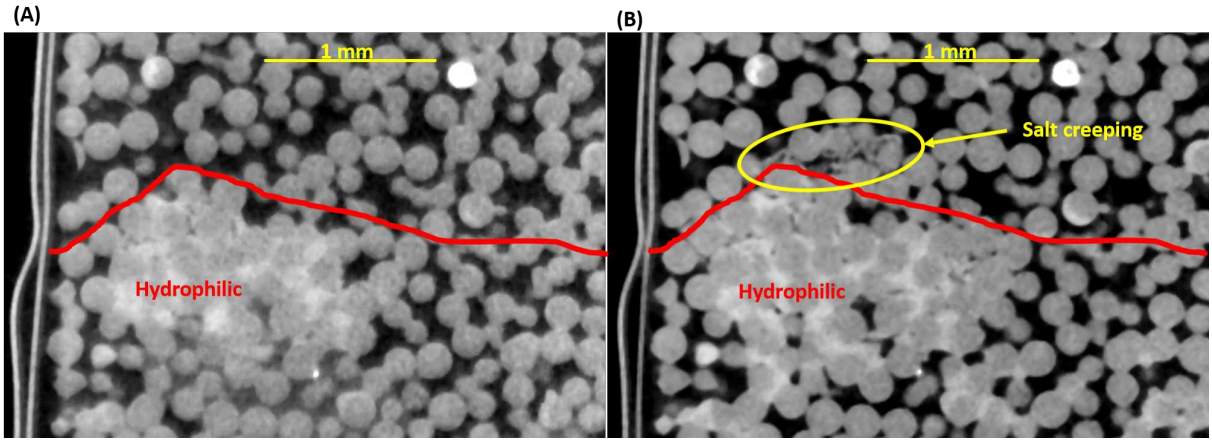

Figure 4.17: Vertical cross section of the sample S1-Cl showing subflorescence in the hydrophobic and hydrophilic parts: (A) After 45 hours of drying (liquid saturation = 0.41), (B) at the end of drying (liquid saturation = 0)

Several studies have been conducted to understand the drying kinetics of porous media in the presence of chlorides. Various factors, including evaporation rates, and wettability of the porous materials, have been investigated to study the drying patterns and associated phenomena. Notable studies by [17, 54, 56] have explored these factors. The impact of efflorescence on drying kinetics has also been discussed in the literature as already shown in chapter 1.3 of this thesis. Intuitively, a large amount of efflorescence implies slower drying in porous media. However, in our results, we observed that the S1-Cl sample, exhibited fast drying in the first stage of drying (A) although we had observed a large amount of efflorescence. To gain a deeper understanding of these findings, we can analyze the images in conjunction with the drying curves. We observed that the efflorescence remained wet during the first stage of drying (A) and that there was a hydraulic connection to the surface of drying. We saw that there was brine inside the structure of the efflorescence as shown in figure 4.18. During stage (B) where we did not detect any drying inside the sample, we saw that the brine inside the structure of the efflorescence was drying out. Another observation that we made is that at this stage of drying the hydraulic connection to the surface of drying was lost. In Figure 4.19, we present a slice analysis conducted on the scan representing the end of stage (B). The sample volume was divided into slices, each 10 micrometres thick, horizontally. For each slice, the brine present in each slice was segmented and its area was quantified, i.e., segmented area in figure 4.19(A), and then plotted against the height of the sample. As we move to stage (C) the brine inside the efflorescence was dried out completely and as we saw earlier the drying rate slowed down significantly at this stage.

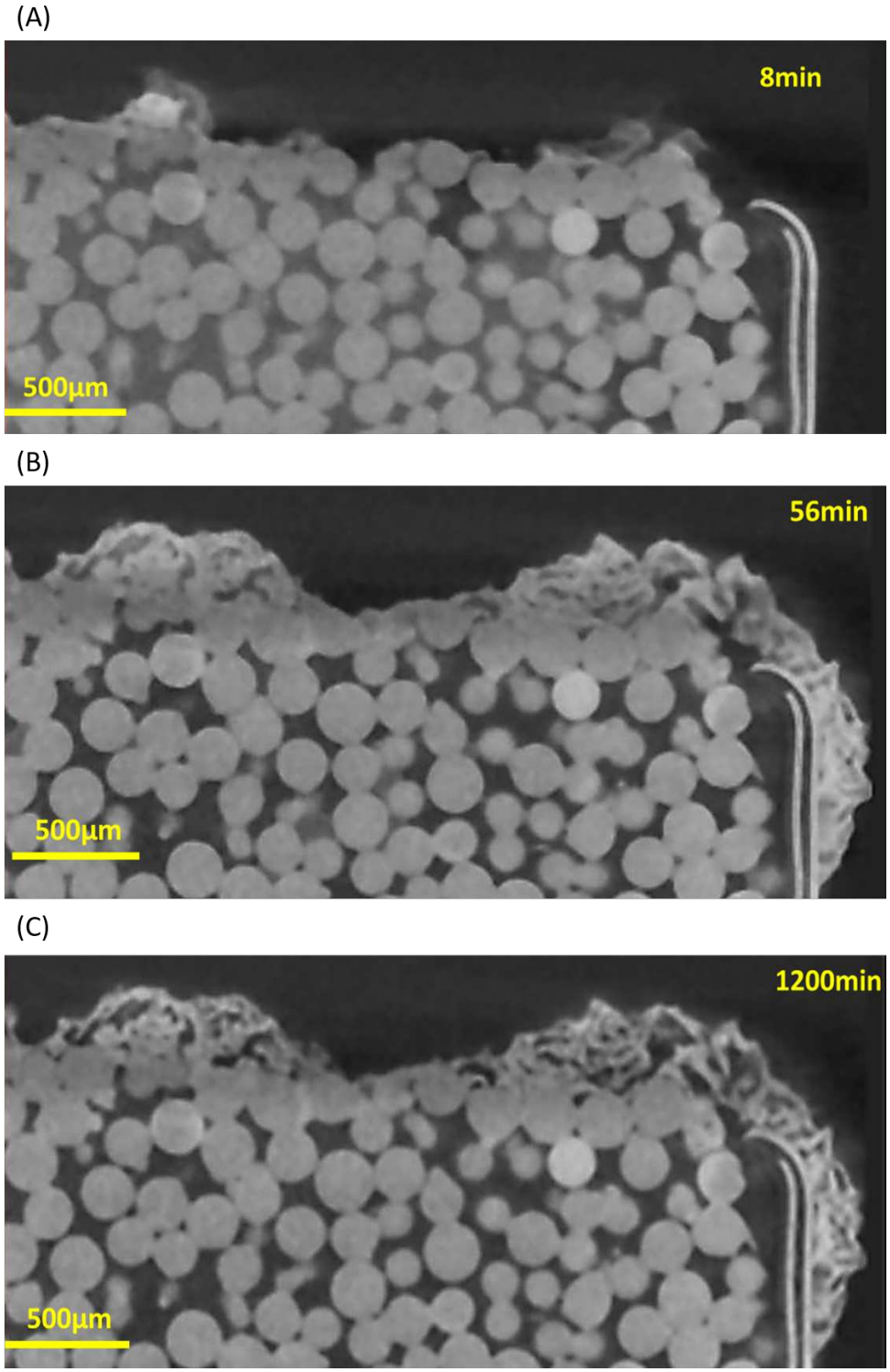

Figure 4.18: Efflorescence evolution during the drying of sample S1-Cl: (A) at the beginning of the drying, (B) at the end of the first stage of drying, (C) at the end of the drying

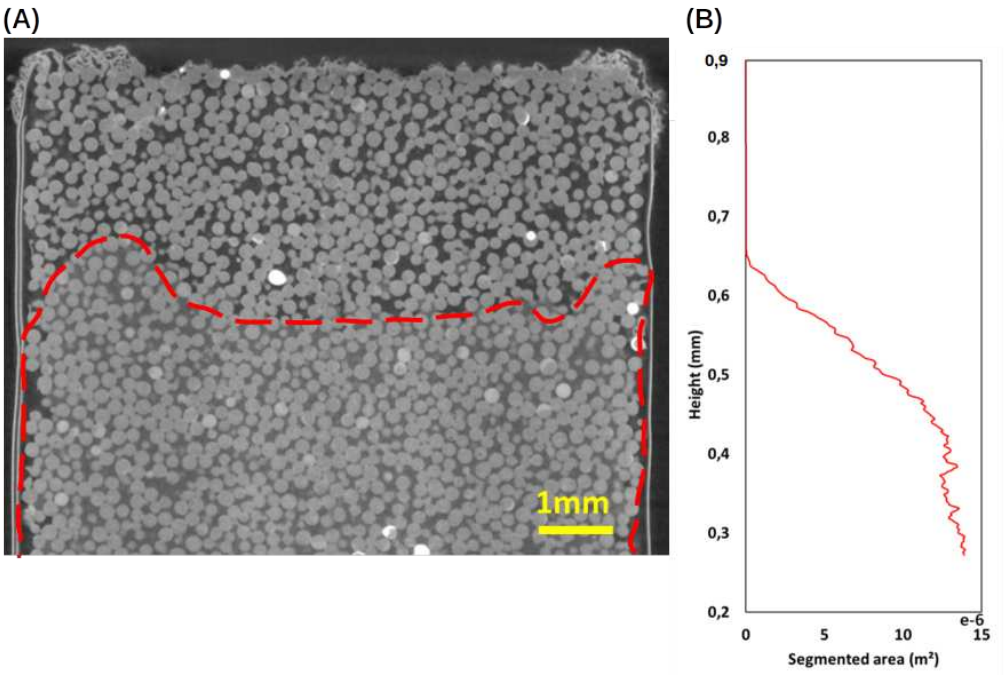

Figure 4.19: Brine evolution through the height of the sample S1-Cl at end of stage (B): (A) quantified brine in the red area, (B) slice analysis of the segmented brine

To explain this, we can refer to the work of N.Sghaier et al. [54, 18] where the influence of efflorescence on the drying kinetics has been discussed. [54] demonstrated that wet efflorescence has a pumping effect. This occurs when the brine in the sample, in contact with the efflorescence, is pumped through the efflorescence and evaporates at the outer periphery. The concentration gradient of the dissolved salt in the liquid plays a role in this capillary pumping effect. As the liquid evaporates, the salt concentration increases near the liquid-air interface. This concentration gradient creates a driving force for the salt ions to move towards the growing structure. The higher salt concentration near the liquid-air interface leads to a higher mass flux of salt, which contributes to the growth of the structure. Therefore, the concentration gradient of the dissolved salt in the liquid is a key factor in the capillary pumping effect. It facilitates the transport of the solution through the efflorescence and contributes to the overall drying kinetics of the porous medium. This explains the faster drying observed in stage (A). In stage (C), the drying rate significantly decreases, which can be attributed to the less porous nature of the efflorescence acting as a barrier for vapour diffusion; as explained by J.Desarnaud et al.[19], the presence of a salt efflorescence with small pores reduces the speed of capillary flow through the porous medium. This capillary flow is insufficient to overcome the evaporation rate at low relative humidity. As a result, the wetting films at the outer surface rupture, and the drying kinetics are controlled by the diffusive transport of vapour through the small pores.

Figure 4.20 shows distinct differences in the morphology of accumulated salt between efflorescence and subflorescence, as well as between the accumulation in the hydrophobic and hydrophilic regions. This variation can be attributed to the influence of wettability on the growth of NaCl crystals. The chlorides adopted a more compact structure that envelopes the glass beads

when accumulated in the hydrophilic part. However, when accumulated in the hydrophobic part as we saw earlier the creeping at the end of the drying, it adapts a "skeleton" shape confirming what was studied before as discussed in [55]. These studies highlight that sodium chloride tends to adopt a "skeleton" shape when growing in a non-polar environment such as air or a hydrophobic medium, which aligns with the observations made in our experiments.

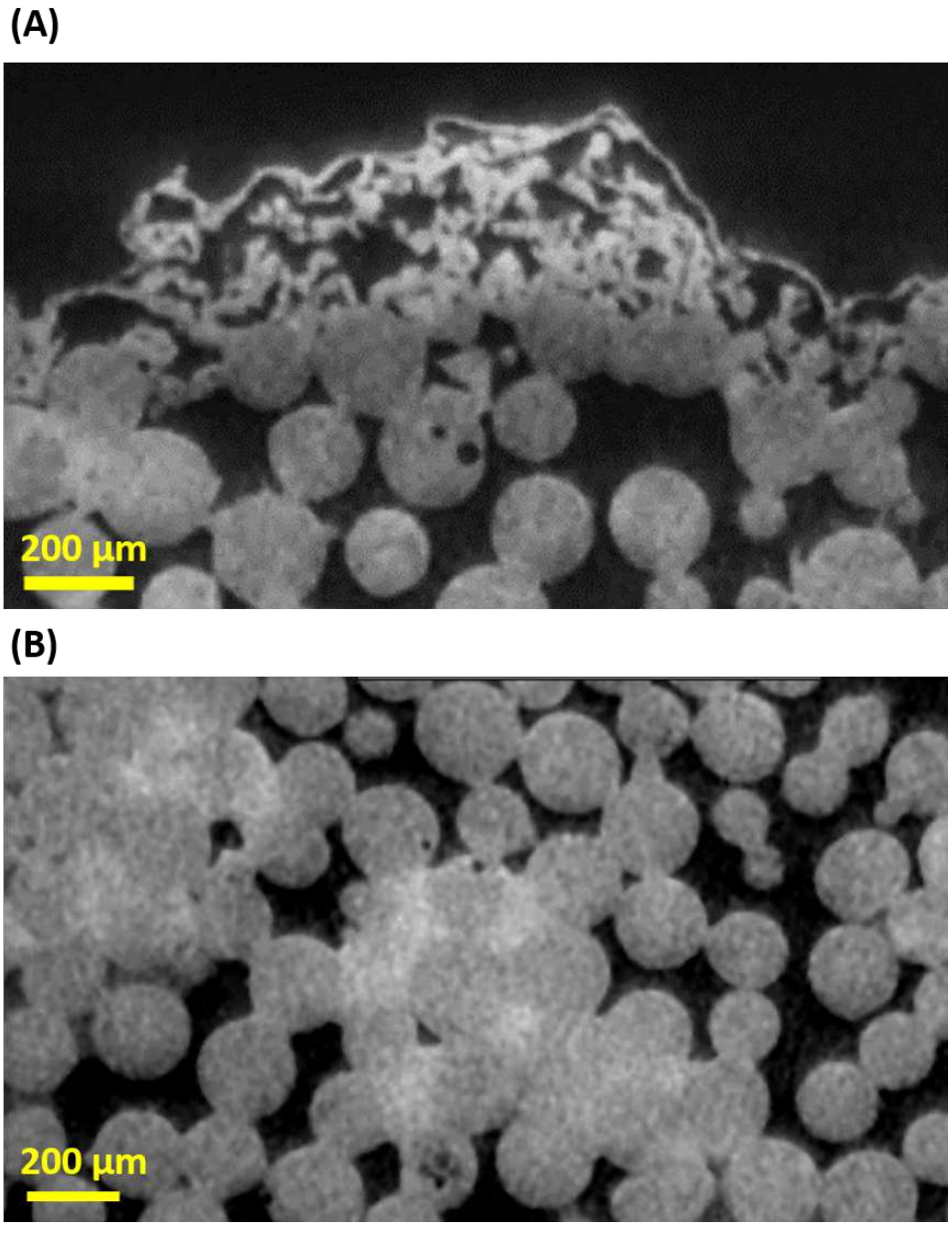

Figure 4.20: Morphology of the accumulated efflorescence and the accumulated subflorescence

4.2.2.2 Drying kinetics and salt accumulation - sample S2-Cl

Figure 4.21 presents the temporal evolution of brine variation in sample S2-Cl during the drying process in the balance apparatus. These curves illustrate how the saturation in water changes over time, with saturation values calculated according to equation 4.5.

$$S_{sample} = \frac{m(t)_{sample}}{m(total)_{sample}} \tag{4.5}$$

Where S_{sample} is the saturation, $m(t)_{sample}$ is the mass of the water content at time t, and $m(total)_{sample}$ is the total mass of water content.

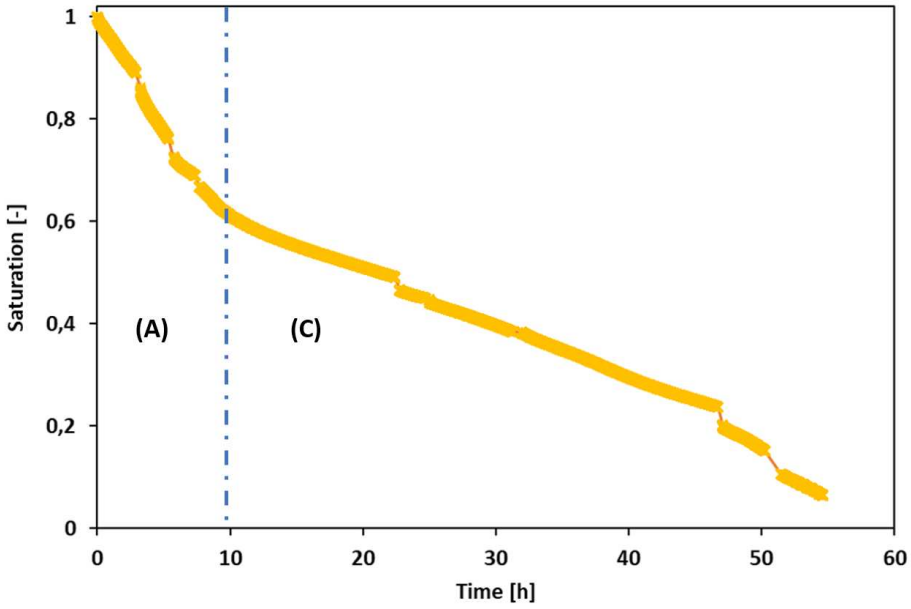

Figure 4.21: Drying kinetics of the sample S2-Cl - balance apparatus

The drying process can be categorized into two distinct stages based on the change in the drying slop: stage (A), marked by a steep drying slope, and stage (C), characterized by a lower drying slope. The end of the first drying stage was marked by the drying of the hydrophobic part.

Making a direct comparison of drying slopes between samples S1-Cl and S2-Cl is not feasible because we would be comparing two different quantities. In the case of sample S1-Cl, the drying data covers only the contents within the sample and it does not include the drying of the brine that is in the efflorescence, whereas in the case of sample S2-Cl, the data encompasses the entire sample along with the efflorescence. However, despite this distinction, both samples exhibited a similar behaviour just before transitioning into stage (C), as depicted in figure 4.22. During the initial stage, in both cases, the hydrophobic part underwent the drying process and the hydraulic connection to the surface was lost by the end of this stage. The sample presented efflorescence that accumulated during the first stage of drying, this efflorescence stopped developing during the second stage of drying. The efflorescence has a "skeleton" morphology but the amount of the efflorescence in this case was not as large as what we saw in the sample S1-Cl as shown in figure 4.23. In figure 4.24 we can see that the efflorescence in the case of the sample S1-Cl covers all of the drying surface in a ring pattern, whereas for sample S2-Cl the efflorescence does not cover all of the drying surface. The sample S2-Cl exhibited subflorescence, which was concentrated at the interface between the hydrophilic and hydrophobic regions, similar to what was observed in the case of sample S1-Cl. The morphology of the subflorescence resembled that of sample S1-Cl, wherein it appeared compact and enveloped the glass beads within the hydrophilic region but exhibited a 'skeleton' shape when accumulating within the hydrophobic region. As shown in figure 4.25. Overall, sample S1-Cl and sample S2-Cl presented similar drying periods of about 60 hours, and similar accumulation patterns at the end of the drying process as shown in figure 4.26.

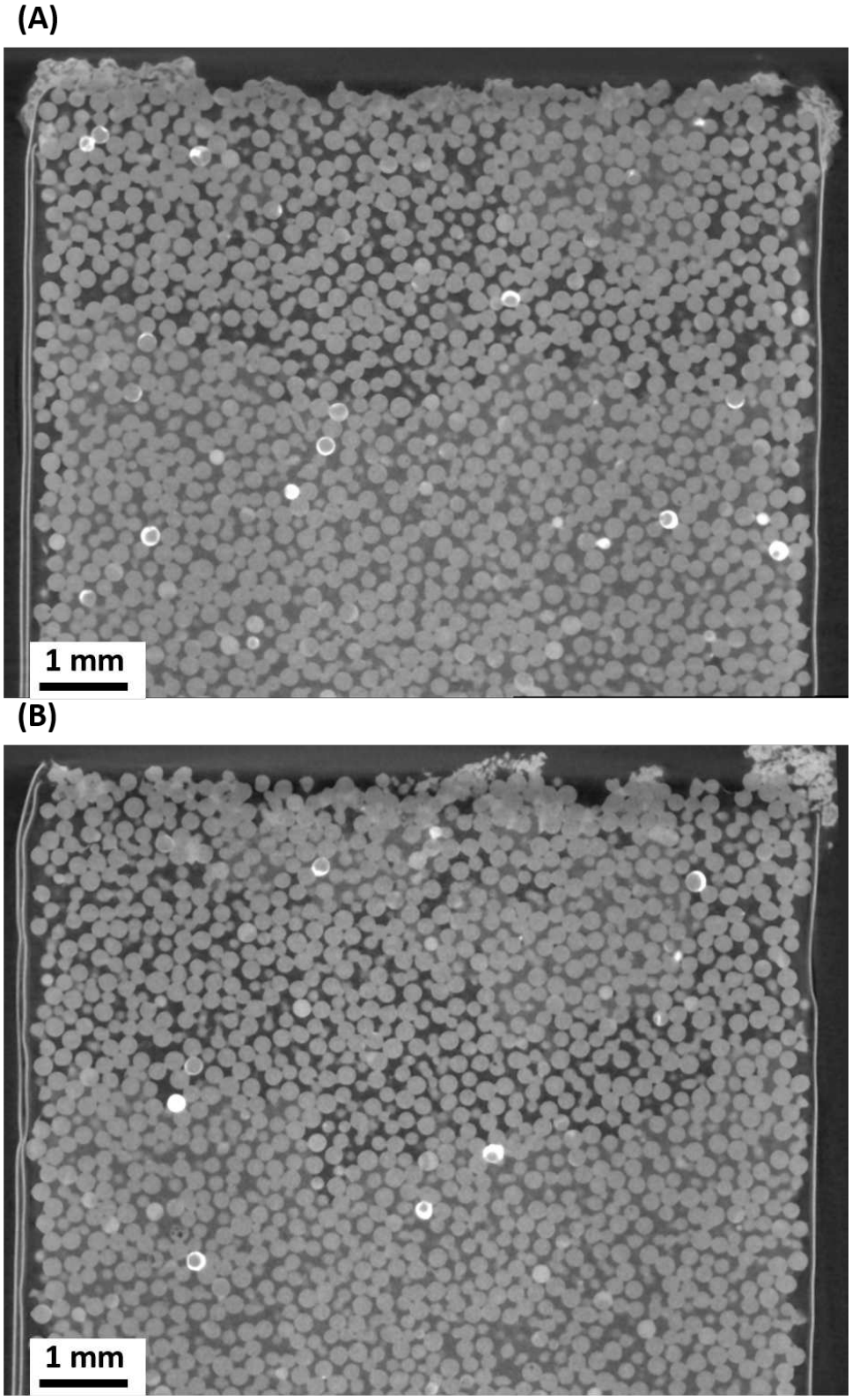

Figure 4.22: Vertical cross sections of the artificial porous media: (A) sample S1-Cl at the end of the first stage of drying, (B) sample S2-Cl at the end of the first stage of drying

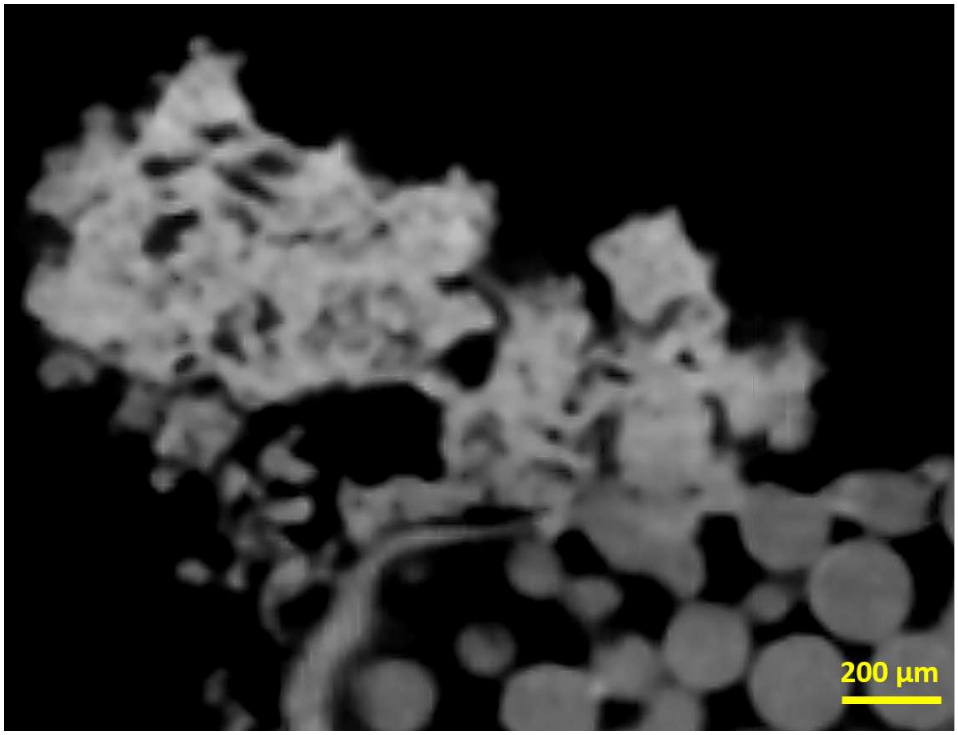

Figure 4.23: Vertical cross section of the sample S2-Cl showing the morphology of the efflorescence

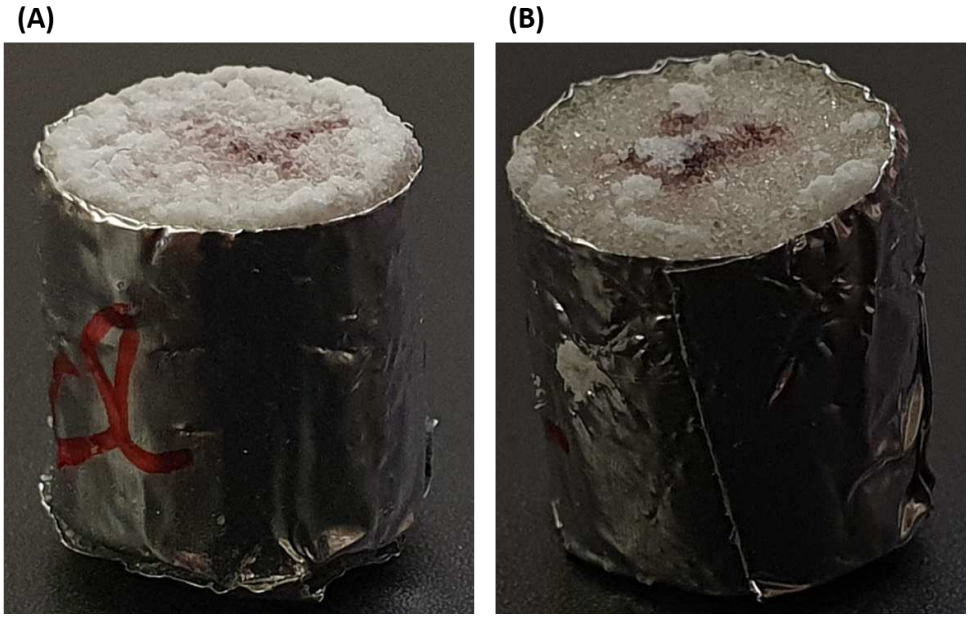

Figure 4.24: Photographs of the artificial porous media : (A) sample S1-Cl, (B) sample S2-Cl

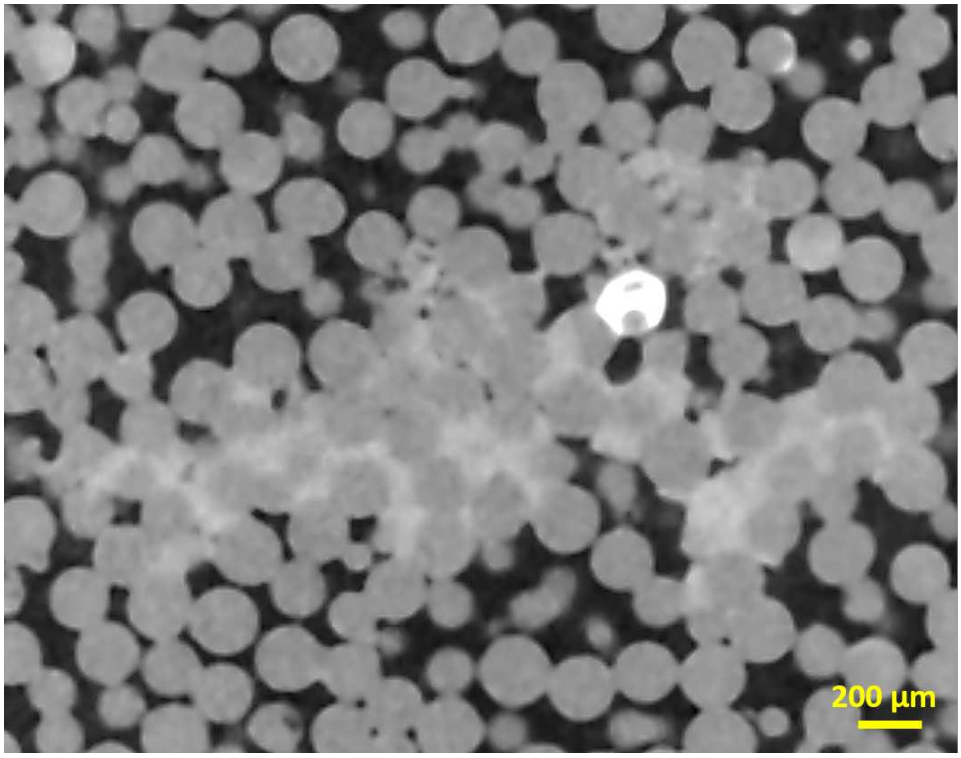

Figure 4.25: Vertical cross section of the sample S2-Cl showing the morphology of the subfluorescence

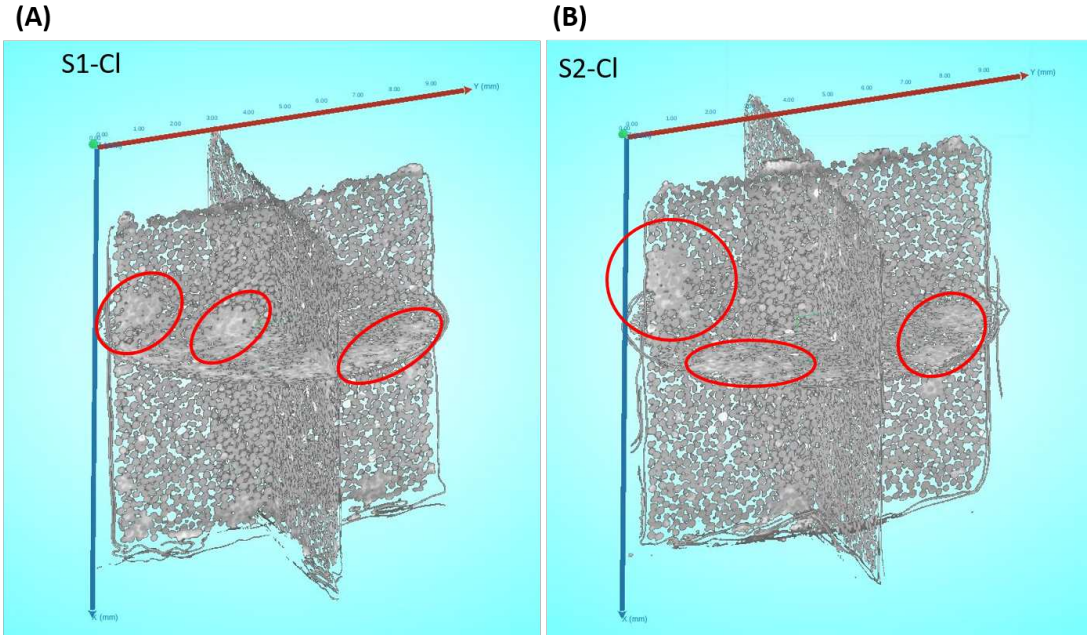

Figure 4.26: 3D slice reconstruction of the artificial porous media at the end of the drying: (A) sample S1-Cl, (B) sample S2-Cl

4.2.3 Drying and accumulation in the presence of Na_2SO_4

4.2.3.1 Drying kinetics and salt accumulation - sample S1-SO first contamination

The drying kinetics of sample S1-SO was determined through image analysis complemented by the intermittent weight measurements when the sample was drying in the climatic chamber. The drying curves are depicted in figure 4.27, representing the water saturation degree in mass fraction (i.e., the mass of water at time t with respect to the initial mass of water). The drying behaviour can be divided into two distinct stages based on the change in drying slope. The initial stage, Stage (A), was characterized by a steep drying slope. This drying regime persisted for a duration of 2 hours and 24 minutes. As the drying process entered the second stage, stage (C), the drying slope decreased. A notable observation, in this case, is that the hydraulic connection to the surface of drying was not lost as we entered stage (C) of drying as shown in figure 4.28. When representing the initial 50h of drying derived from image analysis, we made the assumption that during drying the brine reached quickly its saturated concentration level and that this concentration remained constant throughout the drying process. These assumptions allowed us to calculate the remaining mass of water during the drying process and to put together the results from the image analysis and from the intermittent weight measurements. The water mass was calculated from the brine volume in the following manner:

$$M_{H_2O} = M_{brine} - M_{Na_2SO_4} = \rho.V_{brine} - M_{Na_2SO_4} \tag{4.6}$$

$$m_{sat}.M_{H_2O} = n_{Na_2SO_4} \tag{4.7}$$

$$m_{sat}.M_{H_2O} = \frac{M_{Na_2SO_4}}{M} \tag{4.8}$$

$$m_{sat}.(\rho.V_{brine} - M_{Na_2SO_4}) = \frac{M_{Na_2SO_4}}{M} \tag{4.9}$$

$$M_{Na_2SO_4} = \frac{m_{sat}.M.V_{brine}.\rho}{1 + m_{sat}.M} \tag{4.10}$$

where:

- M_{H_2O} : water mass [g]
- M_{brine} : the mass of the brine [g]
- $M_{Na_2SO_4}$: initial salt mass [g]
- V_{brine}: the volume of the brine [cm^3]
- ρ: density of the brine = 1144.78 [kg/m^3]
- m_{sat} : molality at saturation at 25°C = 1.9[mol/kg]
- M: molar mass of Na_2SO_4 = 142.04 [g/mol]

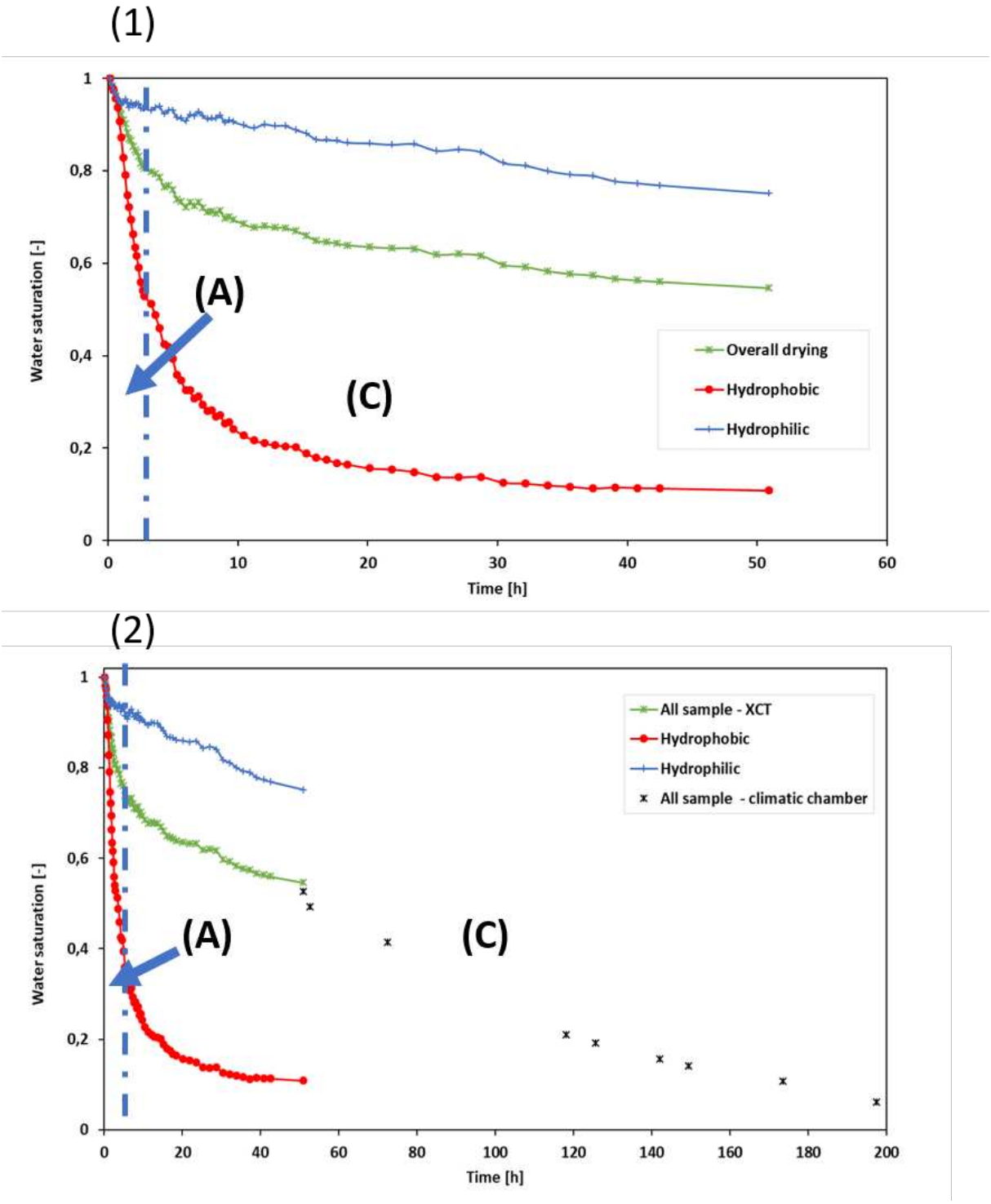

Figure 4.27: Drying kinetics of the sample S1-SO: (1) drying kinetics from XCT, (2) drying kinetics from XCT + climatic chamber

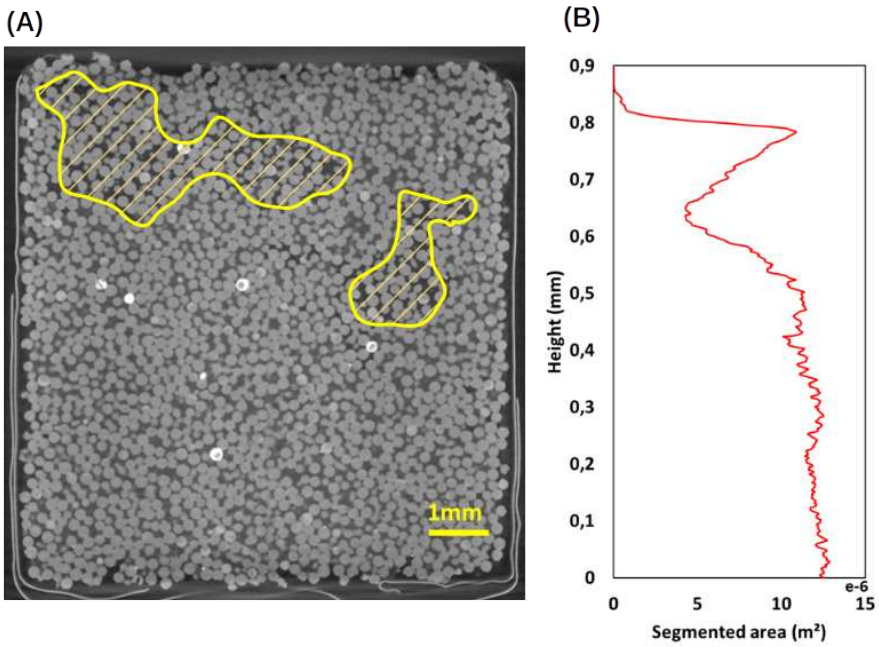

Figure 4.28: Brine evolution through the height of the sample S1-SO at end of stage (A): (A) hatched area represents the dried brine, the quantified brine is the brine in the rest of the sample, (B) slice analysis of the segmented brine

During the scanning period, the observations indicated a relatively minimal amount of salt accumulation, manifested as a thin layer covering the evaporation surface to an extent of approximately 200 micrometres (µm). This outcome corroborates our initial assumption regarding the consistent saturation of the brine throughout the entire scanning period. To obtain a comprehensive understanding of the accumulation of salt within the sample over time, we performed a quantitative analysis of changes in the salt buildup representing both efflorescence and subflorescence, through image analysis. Figure 4.29 provides a visual representation of this analysis, illustrating the dynamic evolution of the ratio of salt accumulated at time t per total salt accumulated at the end of the scanning period and water saturation across the entire duration of the scanning period.

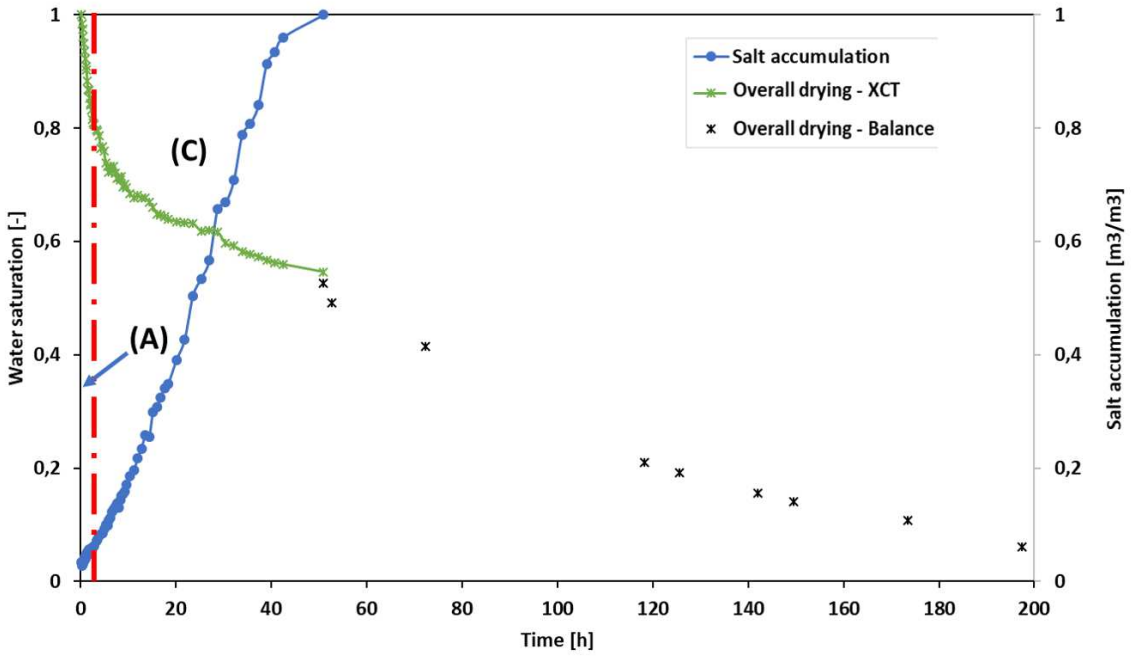

Figure 4.29: Salt accumulation and water saturation of the sample S1-SO - scanner apparatus and climatic chamber apparatus

When comparing the drying kinetics of the sample and the images obtained from the scans, we observed that the onset of the second stage of drying was marked by the formation of a thin layer of salt on the drying surface. As drying progressed, this thin salt layer gradually thickened towards the interior of the sample, as shown in figure 4.30. Throughout the scanning period, that is, the first 50 hours of drying, salt accumulation was observed solely at the surface of drying. At the end of the drying process, the final scan revealed that the majority of the salt accumulation occurred at the interface between the hydrophobic and hydrophilic parts of the sample. This observation is illustrated in figure 4.31. The salt accumulations manifest in a distinctive finger-like pattern extending towards the hydrophilic region, while noticeably absent within the hydrophobic section of the sample except for the thin layer covering the drying surface.

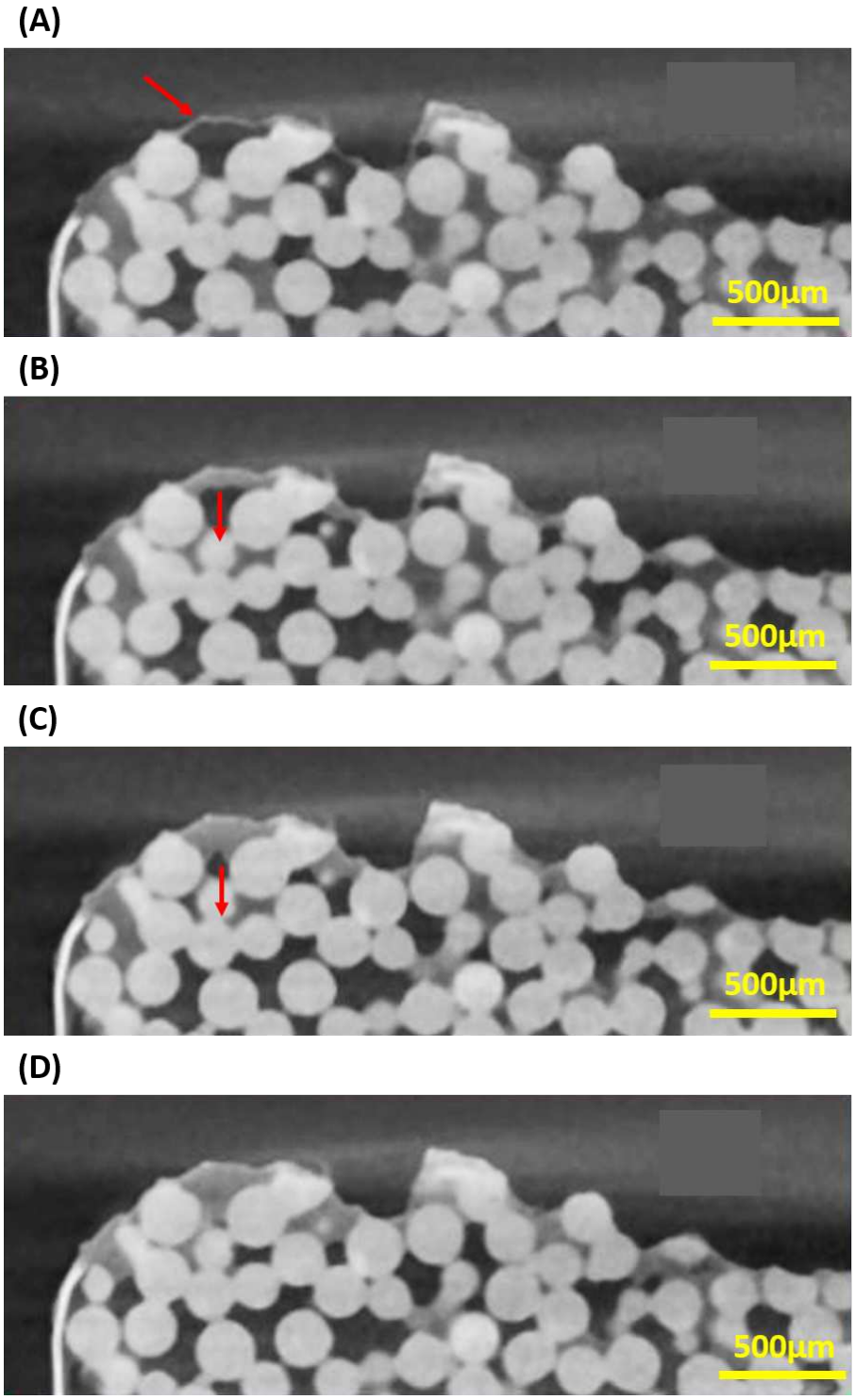

Figure 4.30: Vertical cross sections of the sample S1-SO illustrating the growth of salt at the surface of drying through time where (A) captured at 2h of drying, and (D) after 51h of drying

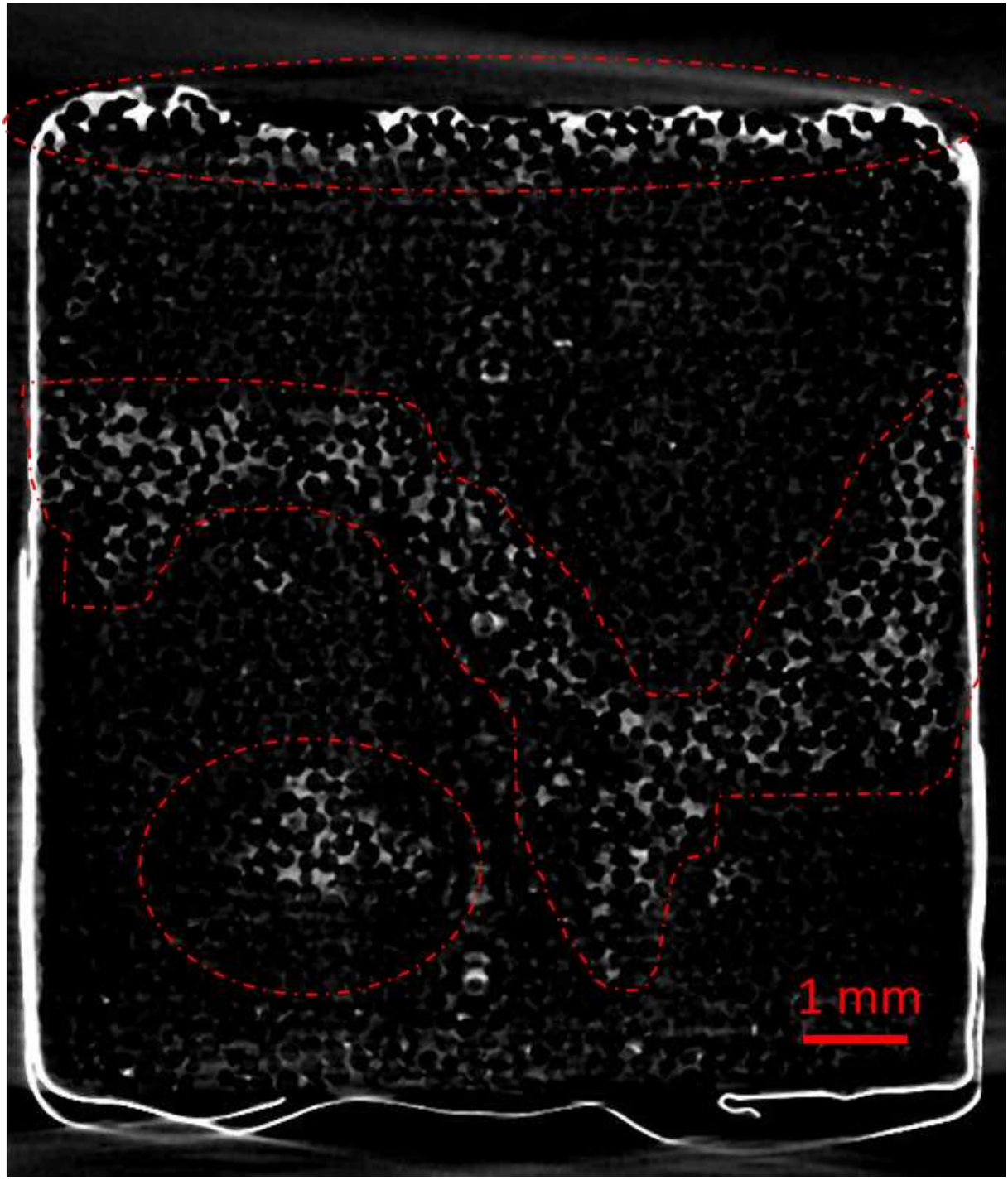

Figure 4.31: Vertical cross section of a differential image of the sample S1-SO: subtraction of the final scan from initial reference scan of the sample in its dry state, dashed red areas represent regions of salt accumulation

4.2.3.2 Drying kinetics and salt accumulation - sample S2-SO

Figure 4.32 presents the temporal evolution of water content variation in sample S2-SO during the drying process in the balance apparatus. This curve illustrates how the saturation in water changes over time, with saturation values calculated according to equation 4.5. The drying process can be categorized into two distinct stages based on the change in the drying slop: stage (A), marked by a steep drying slope, and stage (C), characterized by a lower drying slope.

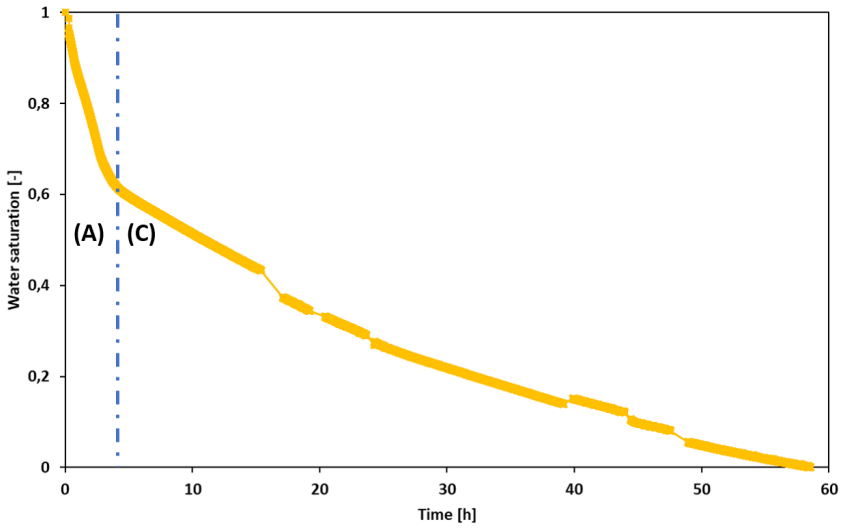

Figure 4.32: Drying kinetics of the samples S2-SO - balance apparatus

At the end of the drying, major salt accumulation occurred at the interface between the hydrophobic and hydrophilic parts of the sample. This observation is illustrated in figure 4.33. Just as we observed for sample S1-SO, the salt accumulations manifest in a distinctive finger-like pattern extending towards the hydrophilic region, while noticeably absent within the hydrophobic section of the sample except for some accumulation below the drying surface.

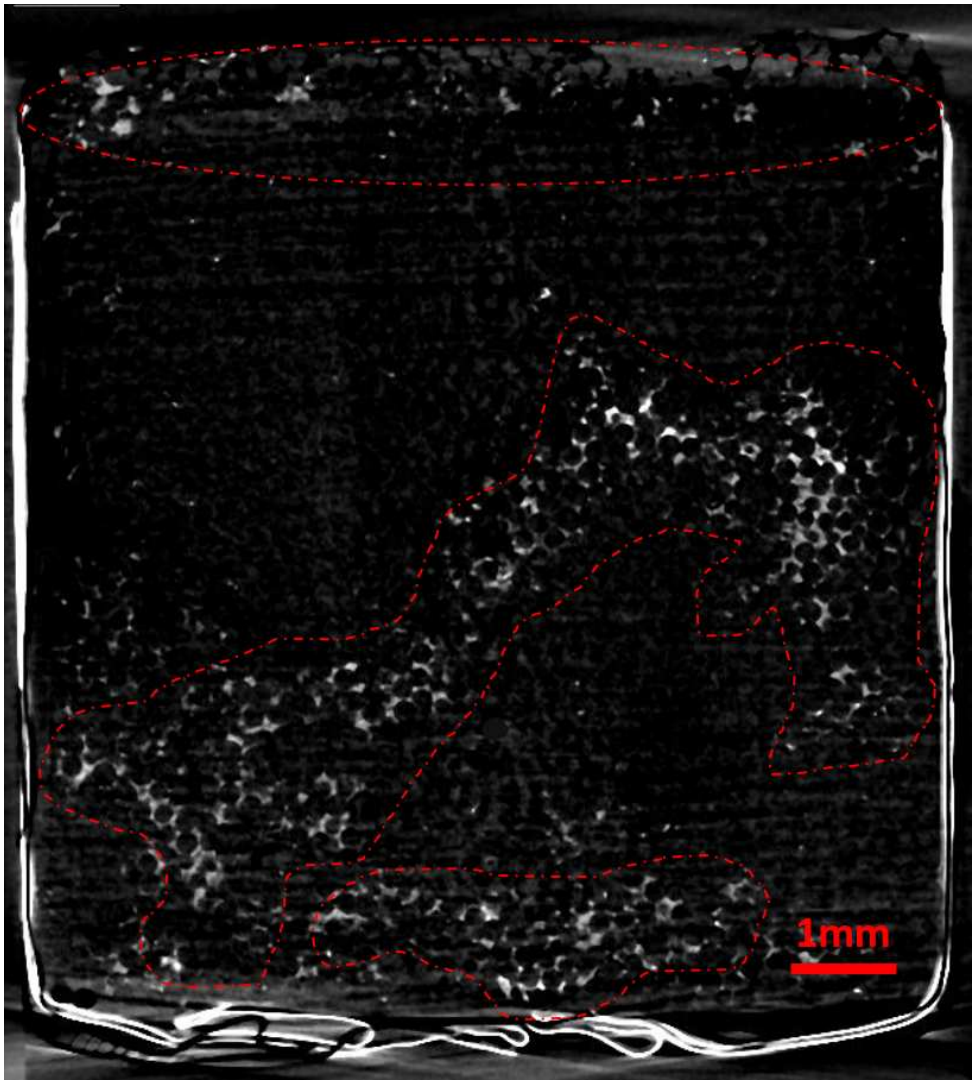

Figure 4.33: Vertical cross section of a differential image of the sample S2-SO: subtraction of the final scan from initial reference scan of the sample in its dry state, dashed red areas represent regions of salt accumulation

In this case, we can compare the drying curves of the samples S1-SO and S2-SO together for comparison since we are approximately comparing the same quantities. Figure 4.34 represents the first 50h of drying of the two samples S1-SO and S2-SO. In this figure, during the first stage of drying before the change in the slope of drying, the two samples showed similar drying kinetics. As we move to the second stage of drying, the sample S1-SO showed a very low slope of drying compared to the sample S2-SO.

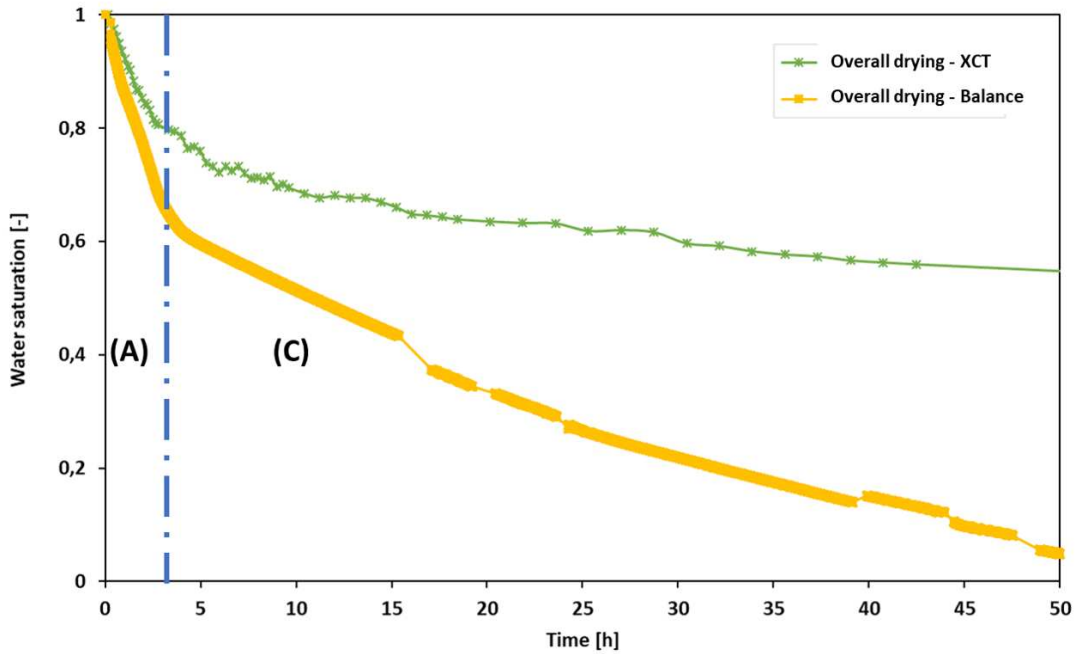

Figure 4.34: Comparison between the drying kinetics of sample S1-SO (XCT) and sample S2-SO (balance) for the first 50h of drying

To explain this difference in the drying behaviour we can refer to the results of the additional experiments on the cleaned S1-SO sample. When we compare the drying behaviour of sample S1-SO before cleaning and the drying behaviour of sample S1-SO after cleaning when saturated with the 1.26 molal sodium sulfate solution, we observed that in the first stage, all of the drying behaviours were similar including the drying behaviour of sample S2-SO when saturated with the same salt solution. As we move to the second stage of drying, the sample S1-SO before cleaning showed a slower drying behaviour compared to the other cases. Whereas, in the other cases after cleaning sample S1-SO and sample S2-SO, the drying behaviour remains the same until the end of drying as shown in figure 4.35.

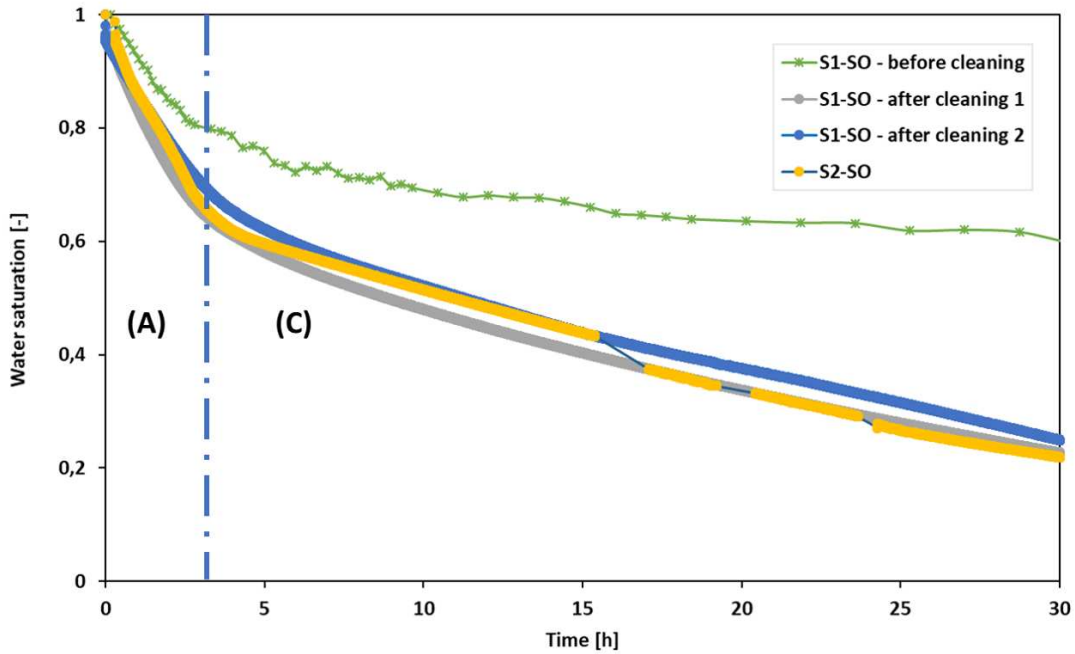

Figure 4.35: Drying kinetics of the sample S1-SO before and after cleaning, and sample S2-SO, when saturated with the 1.26 Na_2SO_4 solution

In all the experiments conducted with the presence of sodium sulfate, we observed a consistent pattern of salt subflorescence. The efflorescence formation was similar in morphology across all samples, as shown in Figure 4.36. Nevertheless, in terms of quantity, the sample S1-SO exhibited more efflorescence during the first saturation compared to the other two saturations after the cleaning of the sample, as depicted in Figure 4.36.

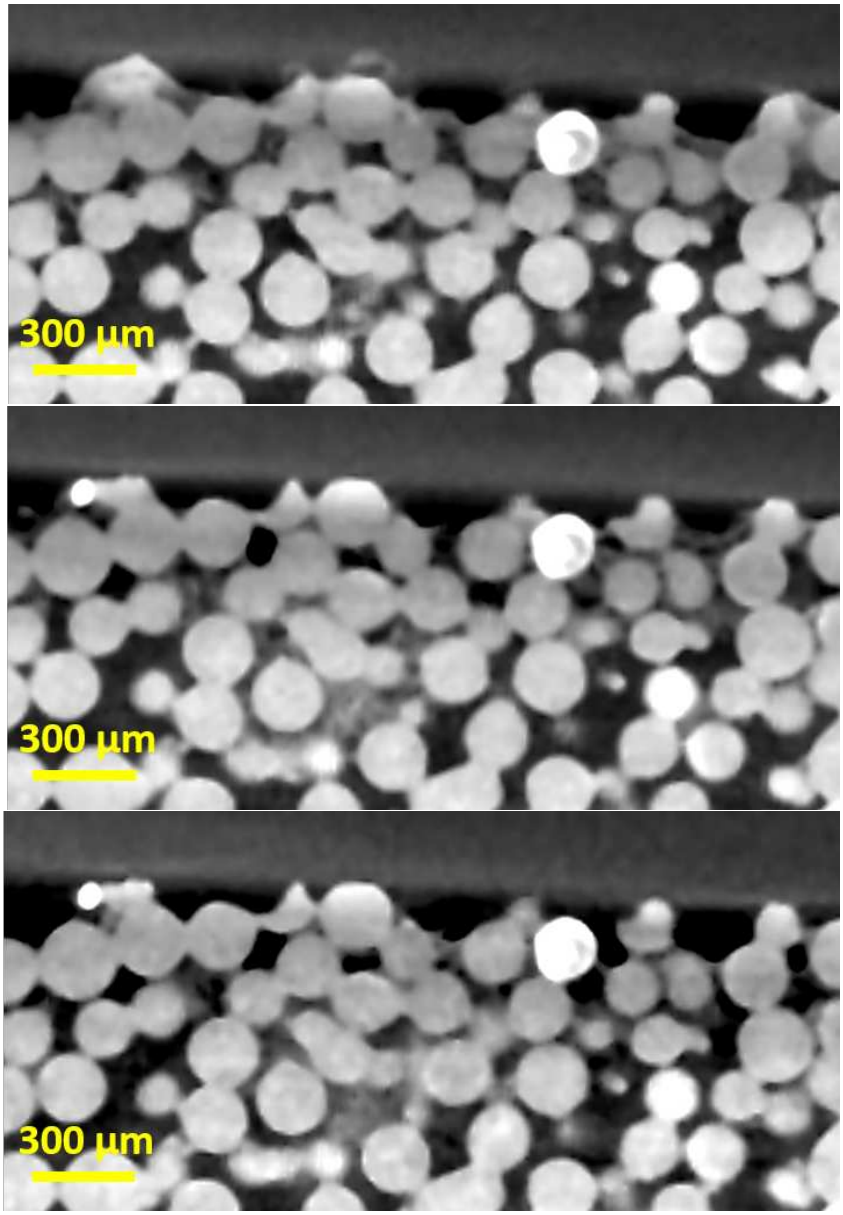

Figure 4.36: Sodium sulfate efflorescence: (A) sample S1-SO first contamination, (B) sample S1-SO after cleaning 1, (C) after cleaning 2

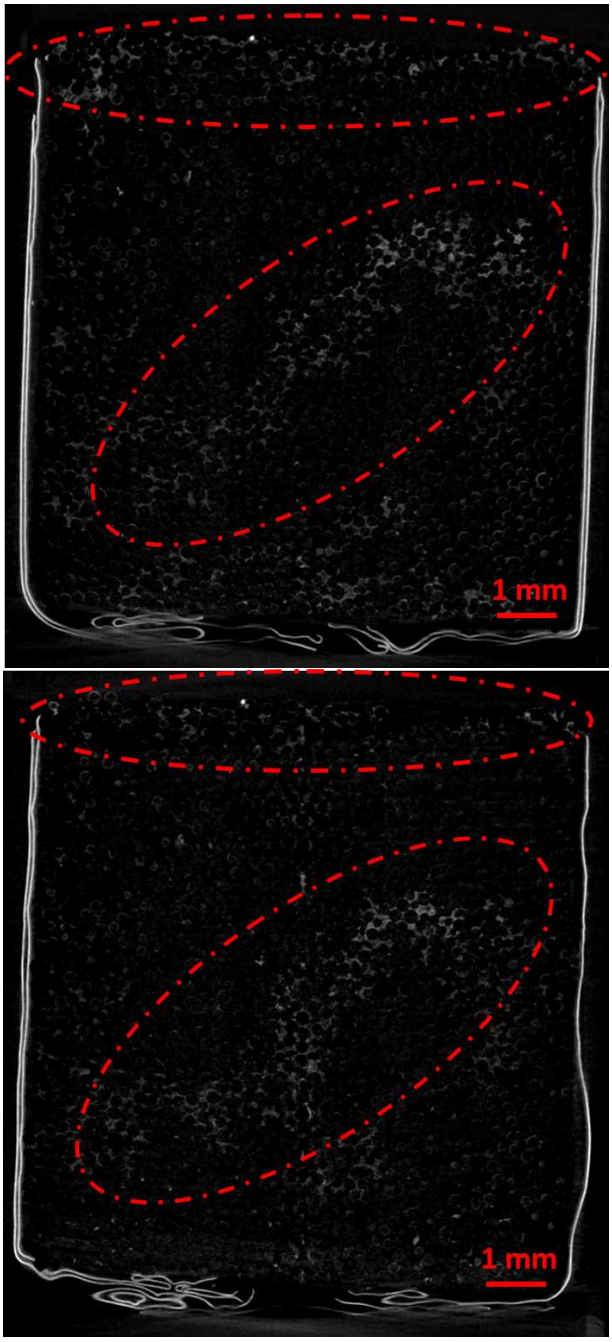

Figure 4.37: Vertical cross sections of the differential image of the sample S1-SO after cleaning 1 and after cleaning 2

In the case of sodium sulfate, the impact of efflorescence or the impact of its presence on the drying of a porous media, in general, was not studied a lot in the literature. If we only consider thermodynamics, and we look at the phase diagram of sodium sulfate, mirabilite is more likely to precipitate in the used experimental conditions as shown in 4.38.

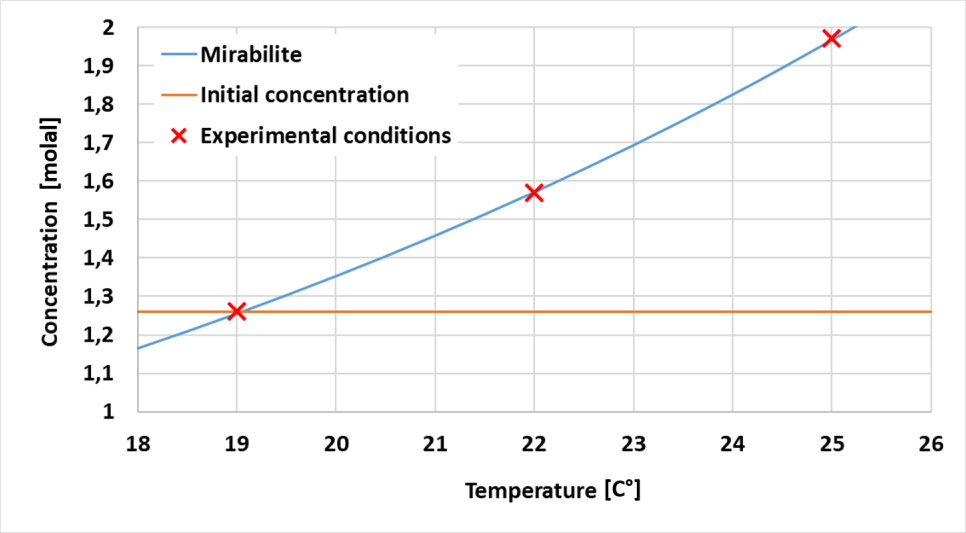

Figure 4.38: Solubility diagram of precipitation of sodium sulfate

To explain the differences in salt accumulation at the drying surface in the three experiments performed on sample S1-SO, we can consider the following hypothesis: the temperature plays a crucial role in the concentration required for the salt to start precipitating. Higher temperatures demand higher concentrations for precipitation as shown in the solubility diagram in Figure 4.38. Consequently, more salt is needed for precipitation at 25°C than at 19°C for example, which explains the higher accumulation of salt at the surface of drying for the experiment conducted at 25°C compared to the experiments conducted at 22°C and at 19°C. In that case, the large accumulation of salt at the surface of drying and the formation of a compact layer initially can significantly reduce the drying slope in the experiment conducted at 25°C. The substantial accumulation of salt at the surface and the presence of the initial compact layer create barriers to vapour diffusion, slowing down the overall drying process. As a result, the drying rate is considerably lower in the experiment compared to the others performed at different temperatures. Furthermore, the solubility diagram in Figure 4.38 also can explain why at 19°C, the accumulation at the interface between the hydrophilic and hydrophobic regions occurs faster than at 25°C.

4.3 Conclusion

The objective of this chapter was the investigation of bi-layered porous media and to attain time-resolved 3D insights into the effects of salt formation on drying kinetics as well as the effect of the assembled wettabilities on salt crystallization for both salts, sodium chloride and sodium sulfate. Our study concluded that different drying kinetics were observed in the case of saturation with sodium sulfate when the temperature was different, whereas similar drying behaviour was observed in the case of saturation with sodium chloride.

The change in the drying slope marked the drying out of the hydrophobic part and losing the hydraulic connection with the surface of drying in the presence of sodium chloride. However in the case of saturation with sodium sulfate, at the end of the first drying stage, the hydrophobic part was still not dry and "fingering-like" percolation patterns were observed towards the hydrophilic part. This suggests that when sodium chloride is present, the drying process occurs more uniformly and progresses in a one-dimensional manner. On the other hand, in the presence of sodium sulfate, drying is characterized by non-uniformity and manifests more as a two-dimensional process. This two-dimensional behavior is evident through variations in the drying pattern both horizontally and vertically, while maintaining a hydraulic connection with the drying surface.

In terms of salt accumulation, in the case of sodium chloride, the majority of salt was concentrated at the interface between the hydrophilic and the hydrophobic parts, however, salt creeping to the hydrophobic part was observed at the end of the drying. In the case of sodium sulfate, the majority of salt was also concentrated at the interface, but a "fingering-like" salt pattern extended towards the hydrophilic part. The samples contaminated with sodium chloride showed high amount of efflorescence, where we saw that it was wet in the beginning of drying and then became dry at the end of the drying. In contrast, samples contaminated with sodium sulfate showed salt primarily accumulating on the drying surface, forming a band-like layer, rather than accumulating outside the drying surface. The use of XCT has enriched our understanding of brine, salt and efflorescence dynamics. X-ray tomography (XCT) has played a crucial role in allowing 3D quantification of the distribution of brine and salt, as well as analysis of their evolution within the porous media. This technique has also provided qualitative information on the development of efflorescence.

Chapter 5

Pore scale analysis of drying-precipitation events in an artificial porous media

The objective of this chapter is to employ a generated pore network to investigate drying and precipitation events at the pore scale of the artificial porous media previously examined in Chapter 4. The pore network was utilized to extract additional, local, information that the global analysis could not provide. Additionally, a perspective section has been included in this chapter to present potential future opportunities utilizing this workflow.

Contents

5.1 Pore network and data generation

This chapter focuses on the investigation of the sample S1-Cl previously examined in chapter 4. As a reminder, the sample was vacuum saturated with a 5.9 molal sodium chloride solution and allowed to dry only from the upper section. The drying process of the sample was monitored through 4D X-ray tomography.

To analyze the pore-scale dynamics, a pore network was constructed using the implemented plugin of OpenPNM [26] within Dragonfly (ORS) software (version 2022.1 and 2022.2 for [Linux]. Comet Technologies Canada Inc., Montreal, Canada; software available at https://www.theobjects.com/dragonfly). The OpenPNM plugin is using PoreSpy's SNOW (Sub-Network of an Over-segmented Watershed) network extraction algorithm. The algorithm determines which pores are connected to each other by using watershed segmentation.
The first step in the algorithm is to obtain the distance transform or distance map of the pore space. The distance map is created from the binary image of the pore space and represents the distance of each voxel from the nearest solid surface. In the next step, the algorithm uses a maximum filter to identify peaks in the distance map. To find the peaks, the algorithm compares the filtered image with the original distance map. Voxels in the filtered image that have the same value as the distance map are considered peaks. This comparison results in a Boolean mask that contains true values at the locations of the peaks. These peaks are then passed as "markers" to a marker-based watershed algorithm to obtain a segmented image partitioned into pore regions. The algorithm determines which pores are connected to each other by scanning the labels in the layer or shell of voxels adjacent to each region in the watershed image. This is accomplished by isolating each region, dilating it, and inspecting the overlapping labels. To determine the size, volume, and location of each pore, the algorithm isolates the region of the watershed image with voxels labelled for that pore and analyzes its properties. The size information is obtained by looking at the corresponding set of voxels in the distance map. The algorithm uses the overlap of the dilated pore region with its neighbours to determine throat properties. The cross-section of the throat connecting two pores is analyzed to find its size and other geometric properties.

To generate the pore network, the previously created binary image of the pore space of the initial state of the sample S1-Cl was used. The generated pore network is presented in figure 5.1.

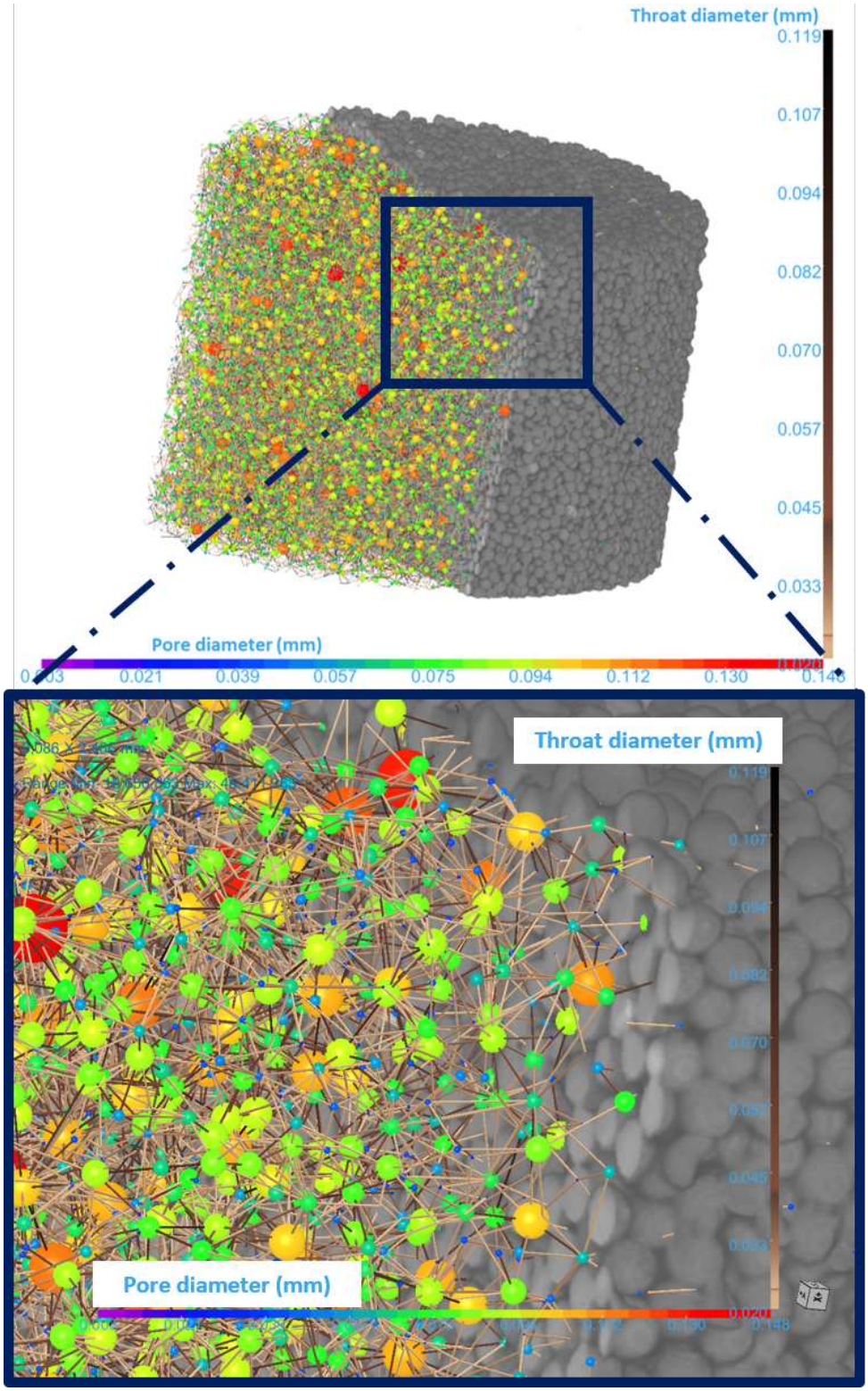

Figure 5.1: Generated pore network for the sample S1-Cl

5.1.1 Pore scale data generation

Morphological data such as diameter, volume, and specific surface, were generated for every pore within the created pore network.

5.1.2 Brine volume, salt volume and grey value generation

The brine and salt volumes were derived from data obtained through the overall analysis. To achieve this, a custom code was developed within the macro builder to map binary images representing the brine volume and binary images representing the salt volume at each time point generated during the overall analysis onto the generated pore network. This process enabled each pore within the network to be associated with the corresponding values of salt and brine volumes for all time steps throughout the scanning duration. Similarly, concerning the grey values, the filtered scans at each time point (t) were also mapped onto the generated pore network. This mapping procedure furnished each pore within the network with the corresponding grey value at each time step during the scanning process as shown in figure 5.2.

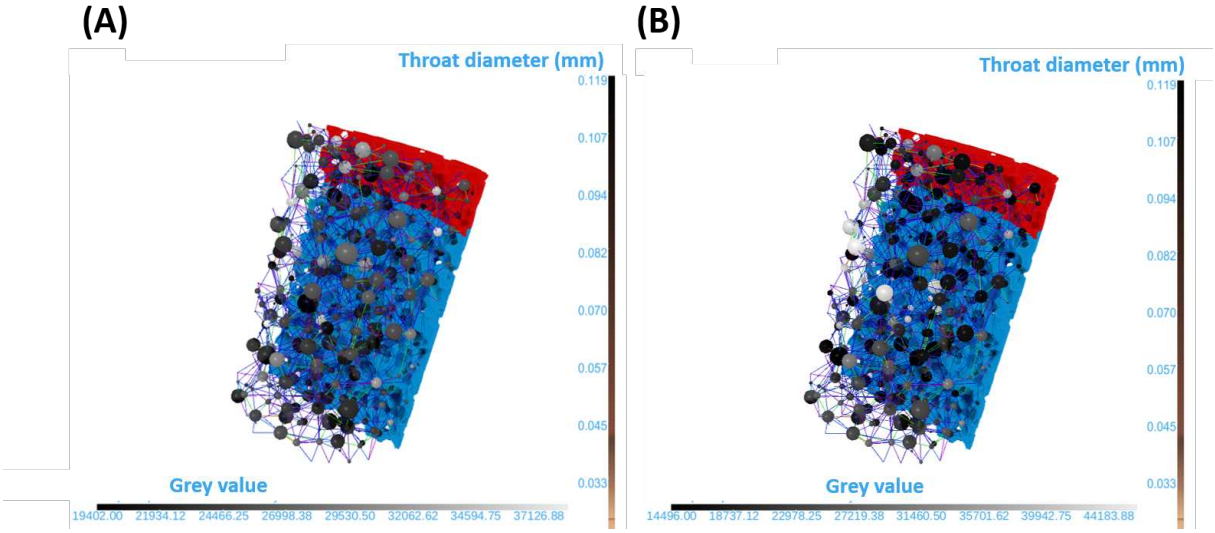

Figure 5.2: Grey value mapping on a REV of the generated pore network: (A) at t=0 of drying, (B) at t=20h of drying

5.1.2.1 Data clustering

The objective of this step is to categorize the generated pores into distinct groups, enabling a thorough investigation into potential variations in drying and salt accumulation within pores of differing diameters. We selected the clustering of the generated pores to explore potential changes in drying and precipitation kinetics as a function of pore diameter. We applied the K-means algorithm to partition the data based on pore size. K-means aims to find groups of data points that are closer to each other within their respective clusters and farther from data points in other clusters. In determining the optimal number of clusters, we based our selection on a comparison of the results with the pore size distribution of the sample as shown in figure

5.3. Our choice of three clusters partitions the pore size distribution effectively. Within this configuration, one cluster (cluster 01) is dedicated to representing the majority of the pores which represent 65% of the pore space, while another cluster (cluster 03) characterizes the smallest pores in the distribution which represent 4% of the pore space. The third cluster (cluster 02) is designed to represent intermediate pore sizes as shown in figure 5.3 which represents 31% of the pore space.

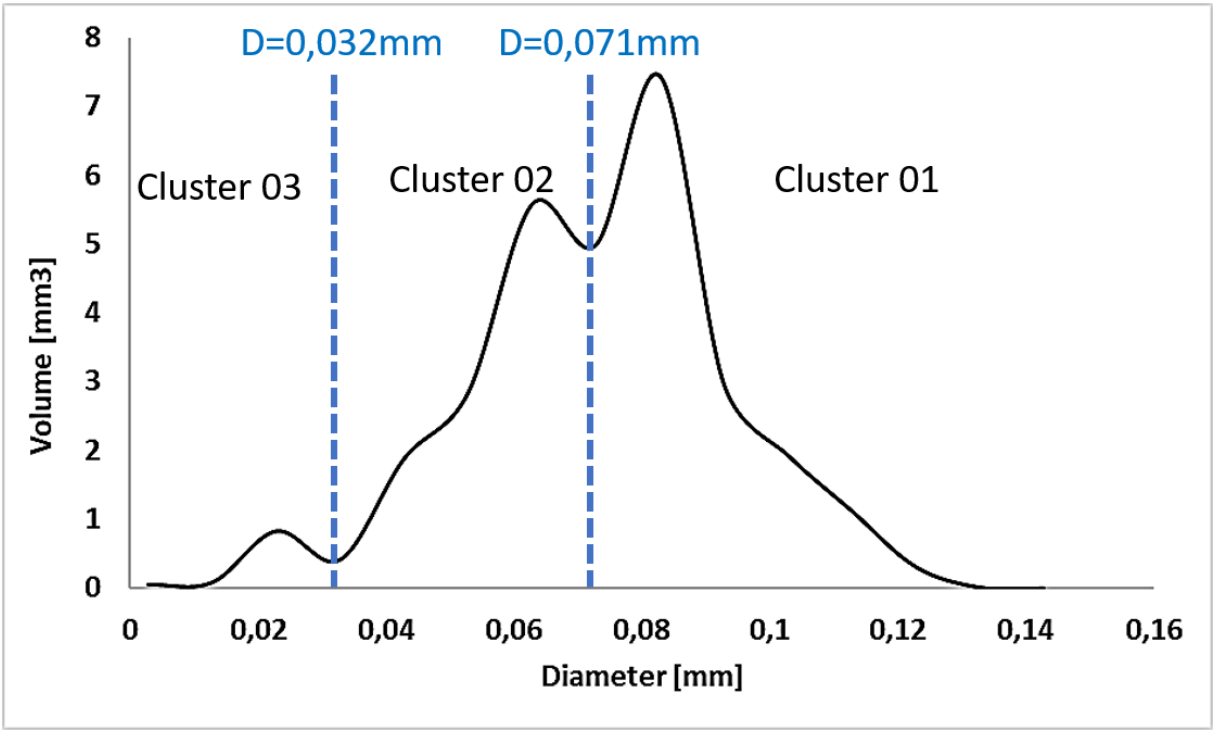

Figure 5.3: Clustering of the pore data of the sample S1-Cl

5.2 Results and discussion

5.2.1 Brine evolution

The drying curves of the different clusters of pores for the hydrophilic and hydrophobic parts are shown in figure 5.4. Each saturation value at every time step represents the average saturation of the pores belonging to the same cluster at that specific time slot. The brine saturation was calculated based on the initial saturation of each cluster in the considered part (hydrophobic or hydrophilic) as shown in equation 5.1

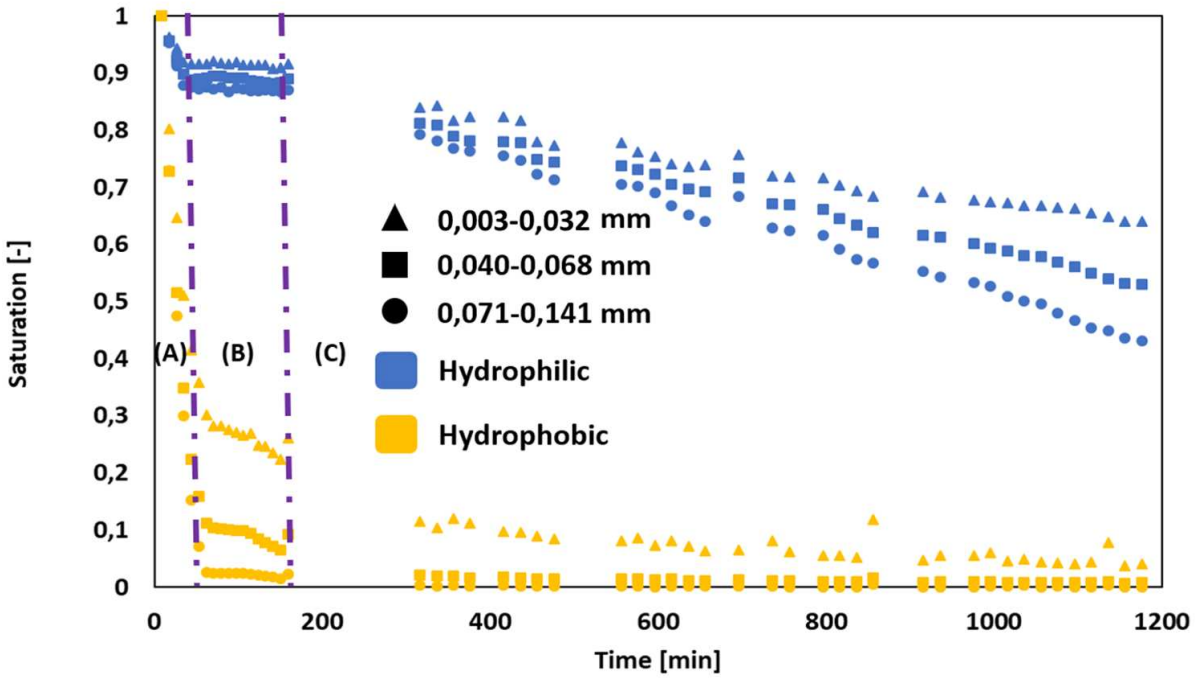

Figure 5.4: Drying curves of the clustered data

$$S(t) = \frac{V_{brine}(t)}{V_{brine}(0)} \tag{5.1}$$

Where $V_{brine}(t)$ is the brine volume at time t and $V_{brine}(0)$ is the initial brine volume in the hydrophobic or in the hydrophilic part.

5.2.1.1 Hydrophobic part

In Chapter 4, our investigation of the overall drying kinetics for sample S1-Cl revealed the existence of three distinct drying stages. However, when looking at the drying behaviour of the different pore clusters, not all pore clusters displayed these three stages of drying.
In particular, when examining the hydrophobic region, we noted that the initial stage (stage (A)) displayed a steep drying slope. During this phase, the drying slopes of the clusters were closely

aligned. However, it is worth noting that the drying slope of the larger pores was slightly higher than that of the smaller pores, as depicted in Figure 5.5. It is worth noting, though, that the larger pores in this hydrophobic segment had nearly achieved complete dryness by the end of the first stage, constituting 98% of the drying, while the other clusters remained incompletely dried. The intermediate-sized pores attained an 80% of dryness, while the smaller pores reached 70% dryness.

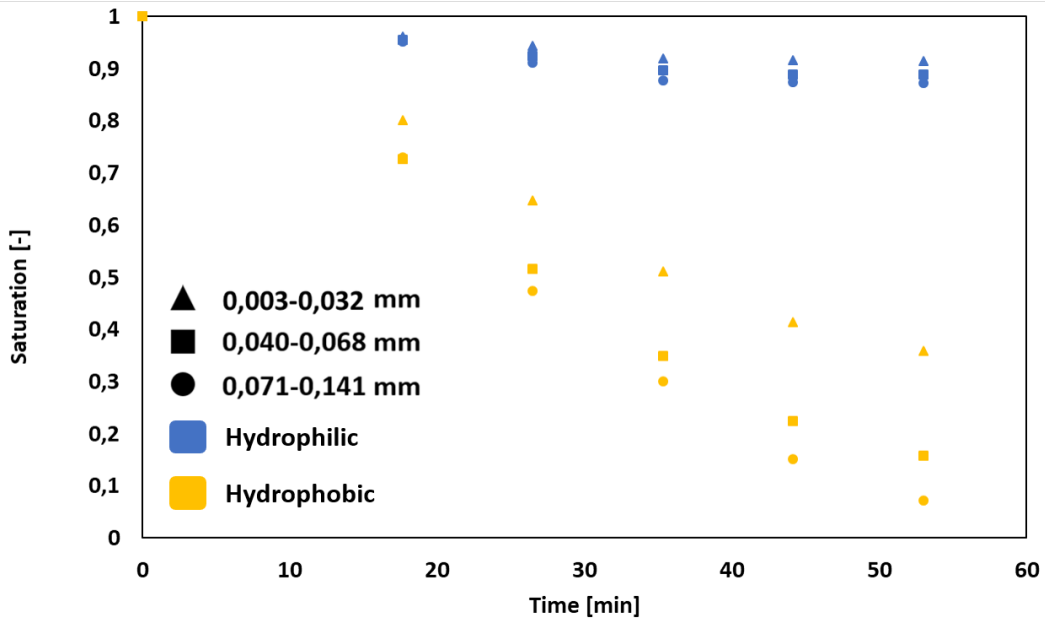

Figure 5.5: Drying curves of the clustered data at the first stage of drying

As we progressed to the second (stage (B)) and third stages (stage (C)) of drying, different behaviours became evident among the distinct pore clusters. The larger pores closely mimicked the second and third stages identified in the overall drying process. In stage (B) of drying, there is a drying rate of zero, and drying only resumes during stage (C). Given their advanced drying status, the remaining 2% of drying occurred during stage (C), as depicted in Figure 5.6. The intermediate pore cluster, also exhibited stage (B) and stage (C) for the larger pores, although stage (C) was very short in duration, lasting for 35 minutes and 19 seconds, as opposed to the 53 minutes observed for the larger pores. The final 30% of drying for the intermediate pores was achieved during stage (C). Shifting our focus to the smaller pores, they displayed only two stages. For this pore cluster, the zero drying rate stage (stage (B)) was not observed. Rather the second stage was characterized by a decreasing drying slope that persisted until the conclusion of the scanning period, resulting in a 96% state of dryness. This observation explained the prior finding in Chapter 4 regarding the incomplete drying of the hydrophobic part at the termination of the scanning period, a phenomenon attributed to the presence of these smaller pores. Another observation is that the difference between the drying states of the larger pores and of the smaller pores keeps decreasing as we advance in the drying process. In this case, the drying curves presented a converging behaviour.

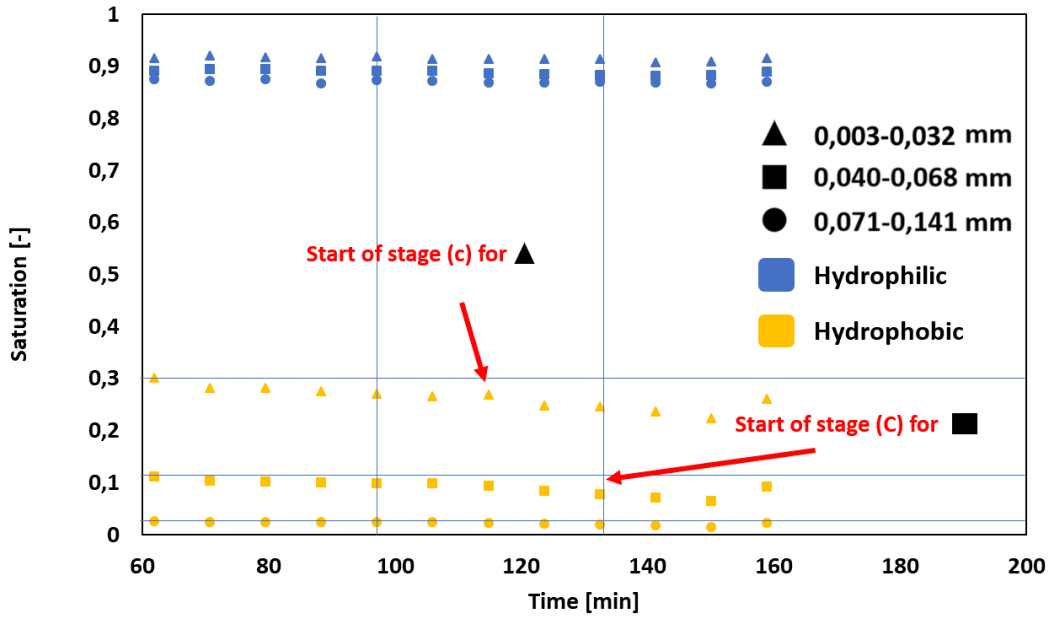

Figure 5.6: Drying curves of the clustered data at showing the beginning of stage (C) in the pore clusters

5.2.2 Hydrophilic part

Conversely, upon investigating the hydrophilic part, the uniform presence of the three drying stages is evident in all pore clusters as shown in figure 5.4. It is important to consider that the first stage may encompass the drying of pores technically situated in the hydrophobic region, potentially due to imperfections in the mask creation process identifying them as hydrophilic pores when in reality they are hydrophobic.
In the second stage of drying, for all pore clusters, we observe a zero drying slope. This implies that the drying process of the sample in the presence of sodium chloride occurs uniformly, resembling one-dimensional drying. In this process, the hydrophobic portion dries first, followed by the hydrophilic part.
Subsequently, in the last stage of drying, all pore clusters started the drying process and presented a linear behaviour as shown in figure 5.7. This is different to what we have observed for the hydrophobic pore clusters where at this stage of drying, the drying curves presented an exponential behaviour as shown in figure 5.8. The slope of drying was however higher in the larger pores and decreases as we go to the smaller pores.

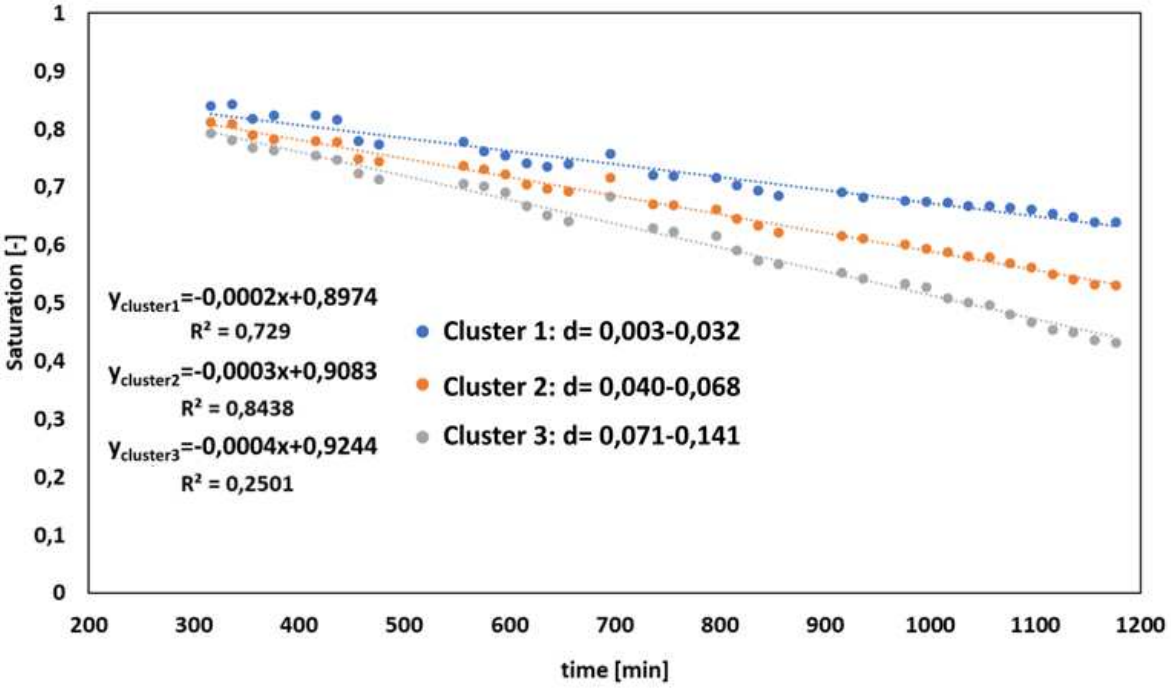

Figure 5.7: Linear fit of the third stage of drying on the hydrophilic pore clusters

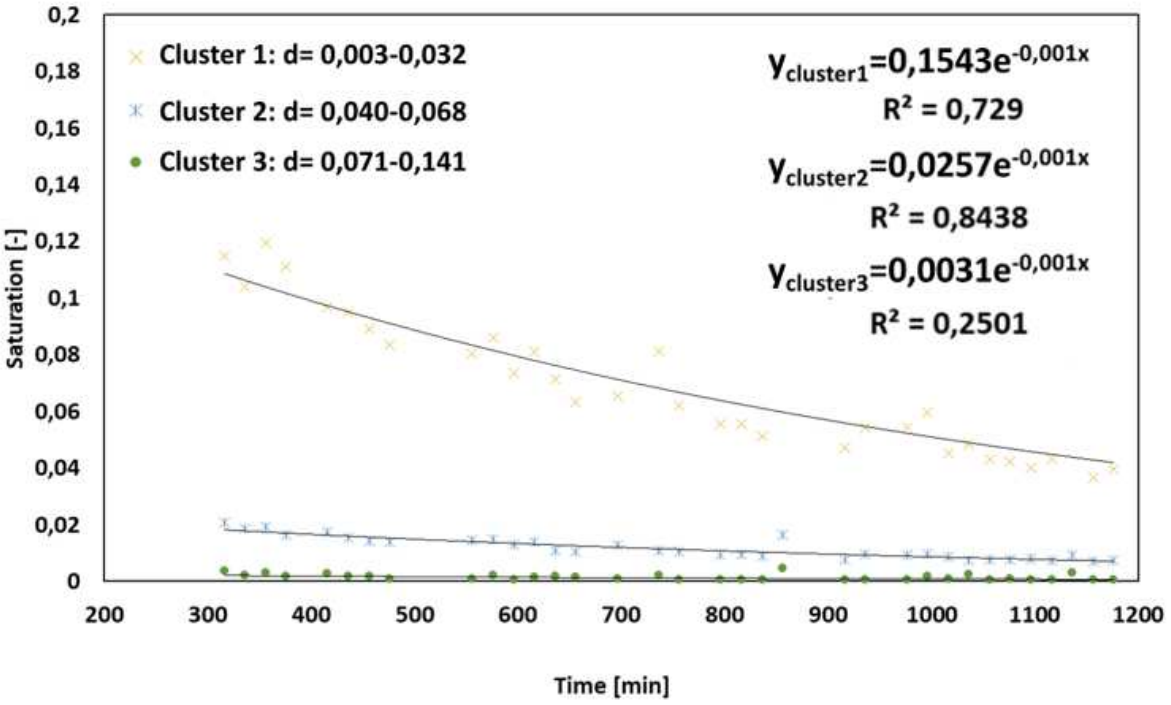

Figure 5.8: Exponential fit of the third stage of drying on the hydrophobic pore clusters

5.2.3 Salt evolution

The salt accumulation curves of the different clusters of pores for the hydrophilic and hydrophobic parts are shown in Figure 5.9. Each salt accumulation value at every time step represents the average salt accumulation of the pores belonging to the same cluster at that specific time slot. The salt accumulation at time t is calculated as shown in equation 5.2

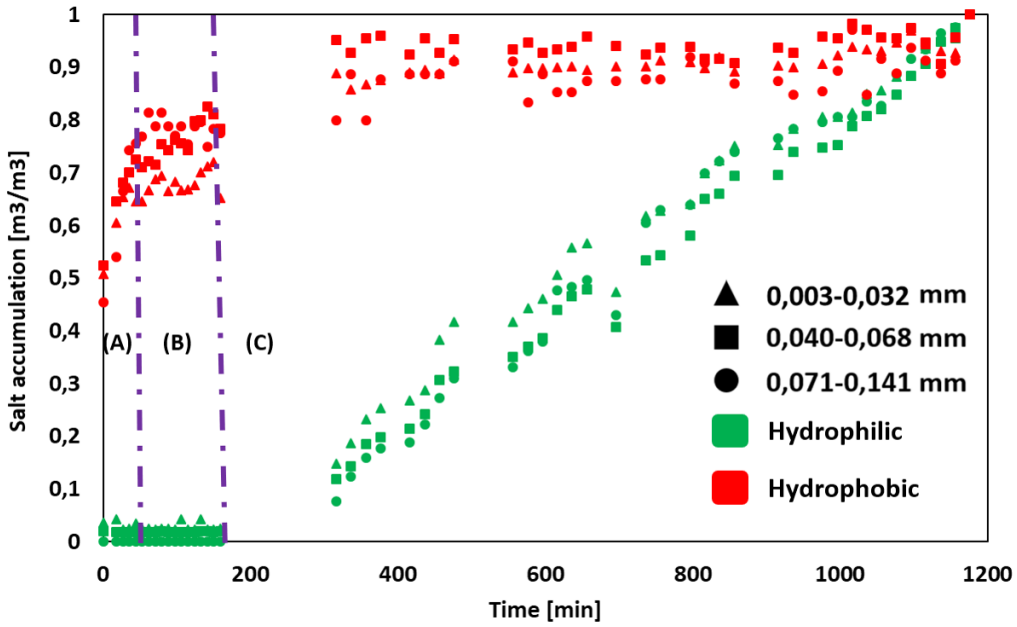

Figure 5.9: Accumulation curves of the clustered data

$$Salt_{accumulation}(t) = \frac{V_{salt}(t)}{V_{salt}(final)} \tag{5.2}$$

Where $V_{salt}(t)$ is the salt volume at time t and $V_{salt}(final)$ is the final salt volume for each cluster in the hydrophobic or hydrophilic part. The accumulation that we see in the hydrophobic part represents what was accumulated just below the surface of drying. In figure 5.10, if we compare the drying curves and the accumulation curves for the hydrophobic part, we can see that for the first stage (stage (A)), the pores with faster drying showed faster accumulation of salt.

As we move to the second stage, the accumulation stopped in the larger and intermediate pores, but it continuous in the smaller pores which is consistent since only the smaller pores continued to dry at that stage.

In the third stage of drying a small accumulation was observed in the smaller pores, but no accumulation was observed in the larger and intermediate pores. This accumulation at the end of the drying stage is probably due to the salt creeping from the hydrophilic part towards the hydrophobic part that was previously observed in chapter 4.

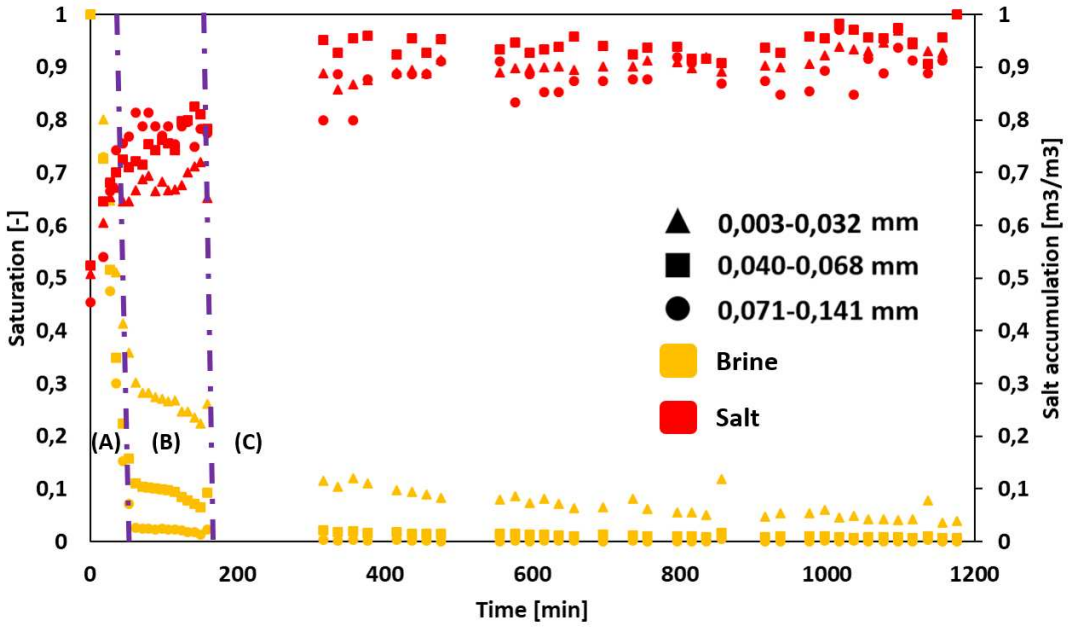

Figure 5.10: Accumulation curves and drying curves of the hydrophobic clusters

In the context of the hydrophilic part, it is noteworthy that no salt accumulation was observed during the initial and second stages of the drying process. The onset of salt accumulation was evident during the third stage of drying, which correlates with the overall accumulation patterns shown previously in Chapter 4 of our study. Notably, while distinct drying rates were observed among the three clusters during this stage, the accumulation rates displayed similarity across all clusters as shown in figure 5.11. One plausible explanation for this uniform accumulation behaviour is the proximity of the salt solution to saturation. So since the solution had already approached a state of saturation, thereby facilitated consistent salt accumulation regardless of the variations in drying kinetics.

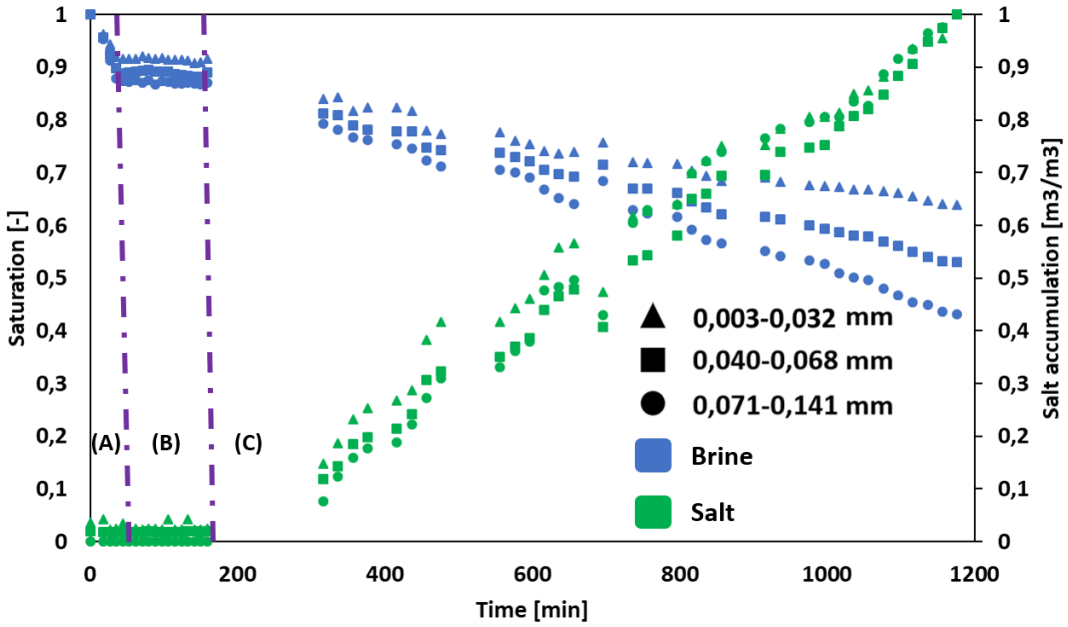

Figure 5.11: Accumulation curves and drying curves of the hydrophilic clusters

5.2.4 Grey value evolution

In this section, our focus is on analyzing the changes in grey values within pores that remained saturated at the conclusion of the scanning period. To conduct this analysis, the data obtained from the mapping of the generated pore network onto the scans of the samples at all time slots during scanning underwent a filtration process. Specifically, only the pores that retained saturation with brine by the end of the scanning period were retained for analysis. Subsequently, we calculated the average grey value for each pore cluster and depicted the results over time in figure 5.12 where the grey value threshold interval for the brine is [22638 to 31964].

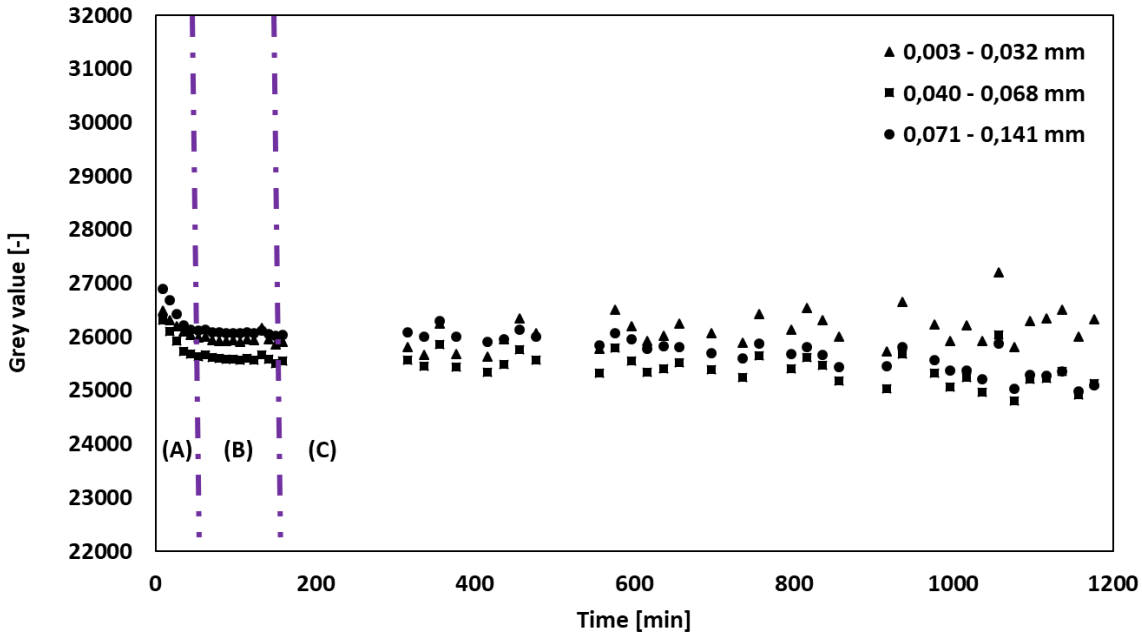

Figure 5.12: Variation of grey value in function of time for the three pore clusters

In the obtained curve, it is evident that the grey values remained consistent for all pore clusters throughout the entire scanning period. This stability can likely be attributed to the salt solution used, which was already near its saturation point. Upon reaching saturation, salt crystallization initiated, and, the solution maintained a constant level of saturation over the entire scanning duration.

5.3 Conclusion

The objective of this supplementary study was to explore the interrelationships between evaporation, precipitation, wettability, and pore size during drying-precipitation events. Pore size exerted a discernible influence on the drying process in both the hydrophobic and hydrophilic regions, with larger pores displaying higher drying rates in both areas.

In both regions, we observed that the smaller pores dries slower than larger pores. The salt accumulation observed in this analysis, characterized by an initial accumulation at the beginning of the drying process and a secondary accumulation towards the end of the scanning period, is in agreement with the patterns previously observed in Chapter 4. In the hydrophobic part, the majority of salt accumulated near the surface at the beginning of drying, and some salt creeping from the hydrophilic region to the hydrophobic part as the scanning period concluded. Conversely, in the hydrophilic region, salt accumulation displayed a uniform distribution across all salt clusters, characterized by a linear trend until the end of the scanning period. Regarding the grey value, we observed no significant variations in the pores that remained saturated by the end of the scanning period, likely attributable to the solution's near-saturation level.
This supplementary analysis revealed that, in the hydrophobic region, small pores remained wet by the end of the scanning period, a finding that was not evident in our initial overall analysis. Additionally, we observed that the stage of zero slope in the drying process was exclusively observed for larger and intermediate-sized pores, but not for smaller pores that continued to dry at that stage for the hydrophobic part.

Chapter 6

General conclusion and perspectives

In this thesis, we addressed the crystallization damage resulting from the interplay of salts, environmental changes, and material properties which is a common issue in both the durability of building materials and cultural heritage preservation. Motivated by the knowledge gap in comprehending this issue within multilayered porous materials, the primary objective of this work was to investigate the impact of sodium chloride and sodium sulfate on bi-layered porous materials in terms of drying, accumulation patterns, and damage. To fulfil this objective, antique Dutch tiles served as a case study representing materials with a porous layer and an impermeable layer. Furthermore, an artificial porous media made from sintered glass beads, featuring a hydrophobic and a hydrophilic part was used as a case study for materials with variable wettability. We have shown the significance of the use of 3D and 4D X-ray tomography as a non-invasive method for gathering qualitative and quantitative data concerning drying kinetics and salt accumulation patterns in these materials.

The study on Dutch tiles introduced an accelerated weathering protocol that induced damage in the Dutch tiles in a relatively short period (less than a month) using two types of salt sodium chloride and sodium sulfate, a combination that was not previously achieved in the existing literature. In the weathering test conducted in this study, both sodium chloride and sodium sulfate contamination led to salt accumulation over multiple cycles before visible damage occurred. The test's effectiveness aligns with previous literature recommendations defining an effective weathering test with two phases, an accumulation phase and a propagation phase. The tested salts exhibited distinct accumulation patterns: sodium sulfate showed minimal efflorescence, while sodium chloride consistently displayed efflorescence in all samples. X-ray tomography offered crucial 3D insights, showing sodium chloride accumulating in small patches throughout the clay body and sodium sulfate forming clusters near the glaze-clay body interface. The consistent accumulation patterns, independent of the tile's type, are intriguing and suggest a substantial influence of the salt's nature on these patterns. Despite different patterns, both salts caused damage to the Dutch tiles, affecting both the glaze and the clay body.

Although damage was not observed in all of the tested samples, deformation profiles indicated internal displacements. The displacements were amplified with cycling in the region close to the glaze-clay body interface. This later suggested potential damage with prolonged cycling even in samples that only showed efflorescence, an accumulation classified as non damaging in the introduction of this thesis. Damage in these tiles is a coupled problem where other factors than salt alone, like the state of the glaze, the pore size distribution of the clay body, or its hygric expansion, play a role. When coupled with salt accumulation, this makes understanding the damage in these materials complex.
For conservators working with similar materials, these findings constitute valuable additions to the current knowledge, enabling adjustments in preservation methods. The study challenges assumptions, indicating that tiles with glaze defects like crazing may not necessarily be more vulnerable. Moreover, the presence of a seemingly "healthy" glaze without macroscopic damage does not guarantee immunity from future damage. Additionally, the insight that practises like removing the efflorescence may not always resolve underlying issues highlights the potential development of internal deformations within the structure, indicating the need for a more comprehensive approach to prevent future damage.

These findings open the door for prospective research that could complement our study. One plausible direction involves investigating the size and shape effects of tile weathering. As elucidated in chapter 3 (refer to section 3.2.3.2), the TESCAN UniTom XL scanner permits the imaging of larger samples, specifically 2x2cm, in contrast to the 5mm cylindrical samples examined in this thesis. Regrettably, this advanced scanner was not available in our laboratory during the study period. Our results underscored the creation of deformations throughout the cycling process. The implementation of the non-rigid registration tool in the Dragonfly software facilitated the tracking of these deformations. Looking ahead, we could enhance our weathering tests by utilizing the TESCAN UniTom XL scanner, providing faster scanning, along with the non-rigid registration feature in Dragonfly. One idea is to conduct multiple scans throughout the cycling stages. This procedure will allow the following deformation inside the tiles and provide better insights into the initiation of damage that will help in improving further the weathering protocol. Additionally, we observed that several parameters, including the state of the glaze layer, can influence the initiation of damage in these tiles. We hypothesized based on our study and on previous observations in the literature that glaze crazing attenuates stress from the clay body while expanding. To test this hypothesis, we propose creating a model porous medium that mimics the tile system.

Pereira and Mimoso (2012) introduced a model system, detailed in their work [45], that emulates tiles. This system allows for adjusting the parameters of the glaze layer, illustrated in Figure 6.1. In this model, they utilized only the clay body. Instead of using a traditional glaze, they opted for glass sheets affixed on top of the clay body. They have experimented with various glaze configurations, exploring scenarios involving delamination between the glaze and clay body, as well as defects like holes in the glaze layer.

Models created by (Pereira et al., 2007)

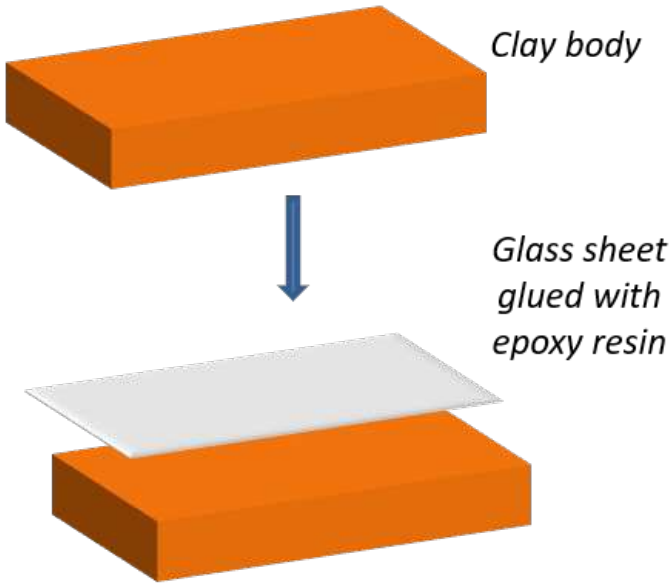

Figure 6.1: Artificial porous media mimicking the tiles proposed by Pereira and Mimoso [45]

In a prospective study, we suggest examining the impact of crazing on tiles. This investigation would entail utilizing the clay bodies of both crazed and intact tiles, each with two glaze configurations: one intact and the other exhibiting crazing. We can design a glaze configuration that simulates crazing and apply it to both types of clay bodies. Conducting this study promises to offer fresh insights into how the glaze configuration influences weathering. Another possible study that will allow us to address the effect of the pore size distribution is the use of a porous

medium consisting of glass beads packed together using epoxy resin, with the protocol for making these artificial porous media detailed in Appendix 6 as shown in figure 6.2. The use of this porous medium provides the opportunity to modify the pore size distribution by introducing glass beads of different sizes. Analyzing the accumulation pattern in the varied pore size configuration will allow us to draw conclusions on the potential influence of pore size distribution on damage.

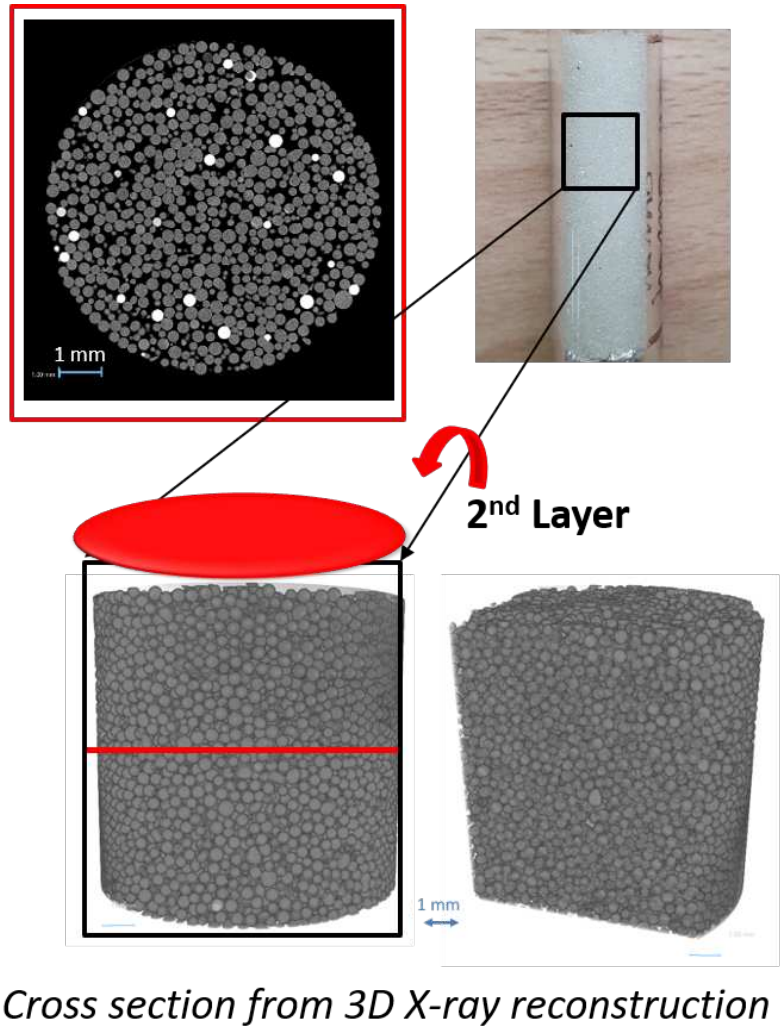

Figure 6.2: Artificial porous media mimicking the tiles using the packed glass beads

Regarding the study on hydrophobic-hydrophilic artificial porous media, the utilization of time-resolved 3D X-ray tomography provided valuable insights into the influence of assembled wettability on the crystallization of sodium chloride and sodium sulfate. Samples contaminated with sodium chloride exhibited a significant amount of efflorescence. Notably, we observed a wet efflorescence at the beginning of drying, transitioning to a dried-out efflorescence at the process's conclusion.
The sustained wet efflorescence exhibited a high drying slope, diminishing rapidly as the drying progressed, resulting in a substantial reduction in efflorescence development. This phenomenon effectively expelled the majority of salt, with efflorescence levels peaking at 4.5 times higher than subflorescence.
For conservators, this finding presents a potential starting point for developing procedures to remove sodium chloride contamination from artworks or buildings. The hydrophobic layer in these samples facilitated efflorescence creation, acting as a pump to expel salt from the porous material, whereas less subflorescence concentrated at the interface between the hydrophobic and hydrophilic parts. Conversely, samples contaminated with sodium sulfate displayed minimal or no efflorescence, with salt primarily accumulating on the drying surface in a band-like layer. The majority of salt in this scenario is concentrated at the interface between the hydrophobic and hydrophilic layers.
It is noteworthy that, for both salts, the interface between the hydrophobic and hydrophilic layers emerges as a targeted zone for potential damage. Nonetheless, this study suggests that sodium sulfate is more likely to cause damage in these structures compared to sodium chloride. Unlike sodium chloride, which exits the structure, sodium sulfate stays inside, indicating a higher risk of long-term harm.

One prospective experimental study that could complement this current work involves investigating sodium chloride and sodium sulfate accumulation in capillary-saturated samples. In the current study, the saturation of the hydrophobic part led to a significant amount of efflorescence in the case of sodium chloride. By not saturating the hydrophobic part in the prospective study, we would eliminate the efflorescence effect, simplifying the investigation.

Global bibliography

[1] M. Angeli. Multiscale study of stone decay by salt crystallization in porous networks. Theses, Université de Cergy Pontoise, Nov. 2007.

[2] G. Bailey, R. Price, E. Voelkl, I. Musselman, E. Doehne, C. Selwitz, D. Carson, and A. de Tagle. Prevention of salt damage to monuments: esem and time-lapse studies. Microscopy and Microanalysis, 7(S2):466–467, 2001.

[3] K. Balksten and P. S.-d. Bruijn. Understanding Deterioration due to Salt and Ice Crystallization in Scandinavian Massive Brick Masonry. Heritage, 4:349–370, 2021.

[4] J. Bear. Dynamics of fluids in porous media. Courier Corporation, 2013.

[5] R. Beare, B. Lowekamp, and Z. Yaniv. Image Segmentation, Registration and Characterization in R with SimpleITK. Journal of Statistical Software, 86(8):1–35, 2018.

[6] K. V. L. Campagne. Een verkeerde loop in't vuur1 : an initial investigation into what Dutch archival sources can tell us about techniques and problems in the production of 17th and 18th century Dutch tin-glaze tiles. In GlazeArch2015, pages 27–33, Lisbon, 2015.

[7] K. V. L. Campagne. 17th Century Dutch Tiles in the Tropics : the Importance of State and Trait on the Deterioration Process. In ICOM Committee for Conservation. Working Group on Glass and Ceramics. Interim meeting, Wrocław, Poland, pages 159–168, 2016.

[8] K. Campagne, Kate Van Lookeren, L. Megens, and M. van Bommel. Understanding 17th-18th century Dutch Tin-glaze through the interpretation and reconstruction of historical recipes. In GlazeArt 2018, pages 150–164, 2018.

[9] H. Carasek, P. Japiassú, O. Cascudo, and A. Velosa. Bond between 19th Century lime mortars and glazed ceramic tiles. Construction and Building Materials, 59:85–98, 2014.

[10] O. Chapuis and M. Prat. Influence of wettability conditions on slow evaporation in two-dimensional porous media. Physical Review E - Statistical, Nonlinear, and Soft Matter Physics, 75(4):1–11, 2007.

[11] A. E. Charola and C. Bläuer. Salts in Masonry: An Overview of the Problem. Restoration of Buildings and Monuments, 21(4-6):119–135, 2015.

[12] E. Colas. Impact de l'humidité et des solutions salines sur le comportement dimensionnel de grès du Buntsandstein : contribution à la sélection de faciès de restauration. PhD thesis, Université de REIMS CHAMPAGNE-ARDENNE, 2011.

[13] C. W. Correns and W. Steinborn. Experimente zur messung und erklärung der sogenannten kristallisationskraft. Zeitschrift für Kristallographie-Crystalline Materials, 101(1-6):117–133, 1939.

[14] M. Costa, P. Cachim, J. Coroado, F. Rocha, and A. Velosa. Ancient Wall Tiles – The Importance of the Glaze/Ceramic Interface in Glaze Detachment. Materials Science, 20(1):108–113, 2014.

[15] P. Coussot. Scaling approach of the convective drying of a porous medium. European Physical Journal B, 15(3):557–566, 2000.

[16] A. M. D'Altri, S. de Miranda, K. Beck, T. De Kock, and H. Derluyn. Towards a more effective and reliable salt crystallisation test for porous building materials: Predictive modelling of sodium chloride salt distribution. Construction and Building Materials, 304:124436, 2021.

[17] H. Derluyn. Salt transport and crystallization in porous limestone: neutron-X-ray imaging and poromechanical modeling. PhD thesis, ETH Zurich, 2012.

[18] H. Derluyn and M. Prat. Cristallisation de sels en milieu poreux. Enclypopédie SCIENCES. ISTE Editions, 2023.

[19] J. Desarnaud, H. Derluyn, L. Molari, S. De Miranda, V. Cnudde, and N. Shahidzadeh. Drying of salt contaminated porous media: Effect of primary and secondary nucleation. Journal of Applied Physics, 118(11), 2015.

[20] E. Doehne. Salt weathering: A selective review. Geological Society Special Publication, 205:51–64, 2002.

[21] R. M. Espinosa-Marzal and G. W. Scherer. Impact of in-pore salt crystallization on transport properties. Environmental Earth Sciences, 69(8):2657–2669, 2013.

[22] L. Esteves, A. E. Candeias, and J. M. Mimoso. Experimental Research with Salt Crystallization in Historical Portuguese Azulejos. International Journal of Architectural Heritage, 10(7):857–866, 2016.

[23] L. Esteves, J. Mirao, L. Dias, A. Candeias, and J. M. Mimoso. Levantamentos in-situ da degradação de azulejos e da presença de sais. Conservar Patrimonio, (23):43–53, 2016.

[24] R. J. Flatt, F. Caruso, A. M. A. Sanchez, and G. W. Scherer. Chemo-mechanics of salt damage in stone. Nature Communications, 5:1–5, 2014.

[25] R. J. Flatt, N. A. Mohamed, F. Caruso, H. Derluyn, J. Desarnaud, B. Lubelli, R. M. Espinosa-marzal, L. Pel, C. Rodriguez-navarro, G. W. Scherer, N. Shahidzadeh, and M. Steiger. Predicting salt damage in practice: a theoretical insight into laboratory tests. RILEM Technical Letters, 2:108–118, 2017.

[26] J. Gostick, M. Aghighi, J. Hinebaugh, T. Tranter, M. A. Hoeh, H. Day, B. Spellacy, M. H. Sharqawy, A. Bazylak, A. Burns, W. Lehnert, and A. Putz. OpenPNM: A Pore Network Modeling Package. Computing in Science and Engineering, 18(4):60–74, 2016.

[27] M. J. Heap, F. B. Wadsworth, Z. Heng, T. Xu, L. Griffiths, A. Aguilar Velasco, E. Vairé, M. Vistour, T. Reuschlé, V. R. Troll, F. M. Deegan, and C. Tang. The tensile strength of volcanic rocks: Experiments and models. Journal of Volcanology and Geothermal Research, 418:107348, 2021.

[28] H. Hens. Building Physics - Heat, Air and Moisture: Fundamentals and Engineering Methods with Exam 2012.

[29] J. H. Hubbell and S. M. Seltzer. Tables of X-Ray Mass Attenuation. National Inst. of Standards and Technology-PL, Gaithersburg, MD (United States). Ionizing Radiation Div, page 120, 1995.

[30] P. Iassonov, T. Gebrenegus, and M. Tuller. Segmentation of X-ray computed tomography images of porous materials: A crucial step for characterization and quantitative analysis of pore structures. Water Resources Research, 45(9):1–12, 2009.

[31] ISO. Carreaux et dalles céramiques Partie 3: Détermination de l'absorption d'eau, de la porosité ouverte, de la densité relative apparente et de la masse volumique globale, 2018.

[32] T. Klimentos and A. Parker. The preparation (by an epoxy-resin method) and physical properties of artificial sandstones. Sedimentary Geology, 59(3-4):307–312, 1988.

[33] J. Lavalle. Recherches sur la formation lente des cristaux à la température ordinaire. Compte Rend. Acad. Sci.(Paris), 36:493–495, 1853.

[34] R. W. Liefferink, A. Naillon, D. Bonn, M. Prat, and N. Shahidzadeh. Single layer porous media with entrapped minerals for microscale studies of multiphase flow. Lab on a Chip, 18(7):1094–1104, 2018.

[35] T. Lombardo, E. Doehne, S. Simon, D. Kwiatkowski, and R. Löfvendahl. The response of NaCl and Umm Ishrin sandstone to humidity cycling: Mechanisms of salt weathering. Proceedings of the 10th International Congress on Deterioration and Conservation of Stone, Stockholm, June 27–July 2, 2004, (July):203–10, 2004.

[36] B. C. Lowekamp, D. T. Chen, L. Ibáñez, and D. Blezek. The design of simpleITK. Frontiers in Neuroinformatics, 7(DEC):1–14, 2013.

[37] B. Lubelli, A. M. Aguilar, K. Beck, T. De Kock, J. Desarnaud, E. Franzoni, D. Gulotta, I. Ioannou, A. Kamat, B. Menendez, I. Rörig-Dalgaard, and E. Sassoni. A new accelerated salt weathering test by RILEM TC 271-ASC: preliminary round robin validation. Materials and Structures/Materiaux et Constructions, 55(9), 2022.

[38] B. A. Lubelli. Sodium chloride damage to porous building materials. PhD thesis, 2006.

[39] J. M. Mimoso. Levantamento em obra de patologias em azulejos históricos. Technical report, Laboratorio nacional de engenharia civil, Lisboa, 2011.

[40] J. M. Mimoso, A. S. Silva, D. R. Costa, T. D. Gonçalves, and S. X. Coentro. Decay of historic azulejos in Portugal : an assessment of research needs. In International Seminar "Conservation of glazed ceramic tiles", National Laboratory for Civil Engineering, Lisbon, pages 1–9, 2009.

[41] Normes Françaises et Européennes. Carreaux et dalles céramiques - Partie 4 : détermination de la résistance à la flexion et de la force de rupture. Technical report, 2014.

[42] C. Nunes, A. Maria Aguilar Sanchez, S. Godts, D. Gulotta, I. Ioannou, B. Lubelli, B. Menendez, N. Shahidzadeh, Z. Slížková, and M. Theodoridou. Experimental research on salt contamination procedures and methods for assessment of the salt distribution. Construction and Building Materials, 298:123862, 2021.

[43] Z. Pavlik, P. Michalek, M. Pavlikova, I. Kopecka, I. Maxova, and R. Cerny. Water and salt transport and storage properties of Msene sandstone. Construction and Building Materials, 22:1736–1748, 2008.

[44] S. Pereira. Salt Degradation of Historic Azulejos. In Azulejar 2012, number October, pages 1–10, Aveiro, 2012.

[45] S. Pereira, D. Rodrigues, and J. M. Mimoso. Tiles degradation due to glaze-ceramics interface defects: study on simulated tiles. Proc. Azulejar, Aveiro, Portugal, pages 01–09, 2012.

[46] S. M. Pereira, J. M. Mimoso, and A. S. Silva. Physical-chemical characterization of historic Portuguese tiles. Technical report, Laboratorio nacional de engenharia civil, Lisbon, 2011.

[47] M. Prat and F. Bouleux. Drying of capillary porous media with a stabilized front in two dimensions. Physical Review E - Statistical Physics, Plasmas, Fluids, and Related Interdisciplinary Topics, 60(5 B):5647–5656, 1999.

[48] A. Putnis and G. Mauthe. The effect of pore size on cementation in porous rocks. Geofluids, 1(1):37–41, 2001.

[49] M. N. Rad, N. Shokri, A. Keshmiri, and P. J. Withers. Effects of Grain and Pore Size on Salt Precipitation During Evaporation from Porous Media. Transport in Porous Media, 110(2):281–294, 2015.

[50] L. A. Rijniers, H. P. Huinink, L. Pel, and K. Kopinga. Experimental evidence of crystallization pressure inside porous media. Physical Review Letters, 94(7):23–26, 2005.

[51] Robert J. Flatt. Salt damage in porous materials : how high supersaturations are generated. Journal of Crystal Growth, 242:435–454, 2002.

[52] C. Rodriguez-Navarro, E. Doehne, and E. Sebastian. How does sodium sulfate crystallize? Implications for the decay and testing of building materials. Cement and Concrete Research, 30(10):1527–1534, 2000.

[53] S. Roels. Characterisation of pore structure by combining mercury porosimetry and micrography. Materials and Structures, 34(236):76–82, 2005.

[54] N. Sghaier and M. Prat. Effect of efflorescence formation on drying kinetics of porous media. Transport in Porous Media, 80(3):441–454, 2009.

[55] N. Shahidzadeh. Effect of Hydrophobization on Wetting, Drying and Salt Crystallization in Porous Materials. Restoration of Buildings and Monuments, 20(6):385–394, 2014.

[56] N. Shahidzadeh-Bonn, S. Rafai, D. Bonn, and G. Wegdam. Salt crystallization during evaporation: Impact of interfacial properties. Langmuir, 24(16):8599–8605, 2008.

[57] M. Steiger. Crystal growth in porous materials - II: Influence of crystal size on the crystallization pressure. Journal of Crystal Growth, 282(3-4):470–481, 2005.

[58] M. Steiger. Salts in porous materials: Thermodynamics of phase transitions, modeling and preventive conservation/salze in porösen materialien: Thermodynamische analyse von phasenübergängen, modellierung und passive konservierung. Restoration of Buildings and Monuments, 11(6):419–432, 2005.

[59] M. Steiger and S. Asmussen. Crystallization of sodium sulfate phases in porous materials: The phase diagram Na2SO4-H2O and the generation of stress. Geochimica et Cosmochimica Acta, 72(17):4291–4306, 2008.

[60] K. Wilhelm. Improving non-destructive techniques for stone weathering research in situ. PhD thesis, University of Oxford, 2016.

[61] Z. Yaniv, B. C. Lowekamp, H. J. Johnson, and R. Beare. SimpleITK Image-Analysis Notebooks: a Collaborative Environment for Education and Reproducible Research. Journal of Digital Imaging, 31(3):290–303, 2018.

Appendix: 3D artificial porous media using glass beads and epoxy resin

1. Introduction

The purpose of this protocol is to create artificial porous media based on the method explained in [32]. The principle of this method is using epoxy resin as a bonding agent for any granular media that does not react with epoxy resin in order to make consolidated artificial porous media with various shapes, sizes, porosities, and pore size distribution.

2. Protocol

There are two main components in preparing this artificial porous media: (i) the epoxy resin mixture; and (ii) the granular media which could be glass beads, sand, or any other packing of grains that will not react chemically with the epoxy resin.

2.1 Epoxy resin mixture

The epoxy resin mixture was prepared in the laboratory under a fume cupboard at 40% relative humidity and 19 °C. In a beaker, 10 parts by volume of epoxy resin (CY1301) and 1.5 parts by volume of hardener (Triethylenetetramine, 60%) were stirred using a magnetic stirrer for 5 minutes. Subsequently, 50 parts of acetone were added to the same beaker, and the mixture was stirred again for 5 minutes. The resulting mixture was promptly stored in a hermetic bottle.

2.2 Preparation of the consolidated porous media

In this section, glass beads with a size range of 250-300 µm or Fontainebleau sand were selected to create artificial porous media. The granular media's desired volume was placed in a beaker, followed by the addition of an epoxy mixture until complete coverage of the granular media, as depicted in Figure 3. The mixture was thoroughly stirred for 5 minutes by hand.

Figure 3: Mixture granular media - epoxy

The wetted beads or sand grains were then positioned in a perforated Büchner funnel above an evacuated flask, as shown in Figure 4. The vacuum flask was sealed, and a vacuum at 20 kPa pressure was applied. The duration of vacuum evacuation depended on the desired porosity (refer to 6) for maximum porosity, the evacuation was repeated until the epoxy-granular media mixture achieved a constant weight.

Figure 4: Vacuum evacuation of epoxy

Subsequently, small quantities of the mixture were introduced into a mold i.e. glass cylindrical capillaries or plastic cylinders and compacted using a compaction tool, following the procedure in Figure 5.

Figure 5: Compaction of the mixture granular media - epoxy into a mold

Each introduced quantity's layer should not exceed 3 mm for optimal homogeneity. The samples were stored in a climatic chamber for 24 hours under the conditions of 21°C and 25% relative humidity. Afterwards, the samples were transferred to an oven under climatic conditions of 40°C and 17% relative humidity for an additional 24 hours. The resulting porous media is presented in Figure 6 and Figure 7.

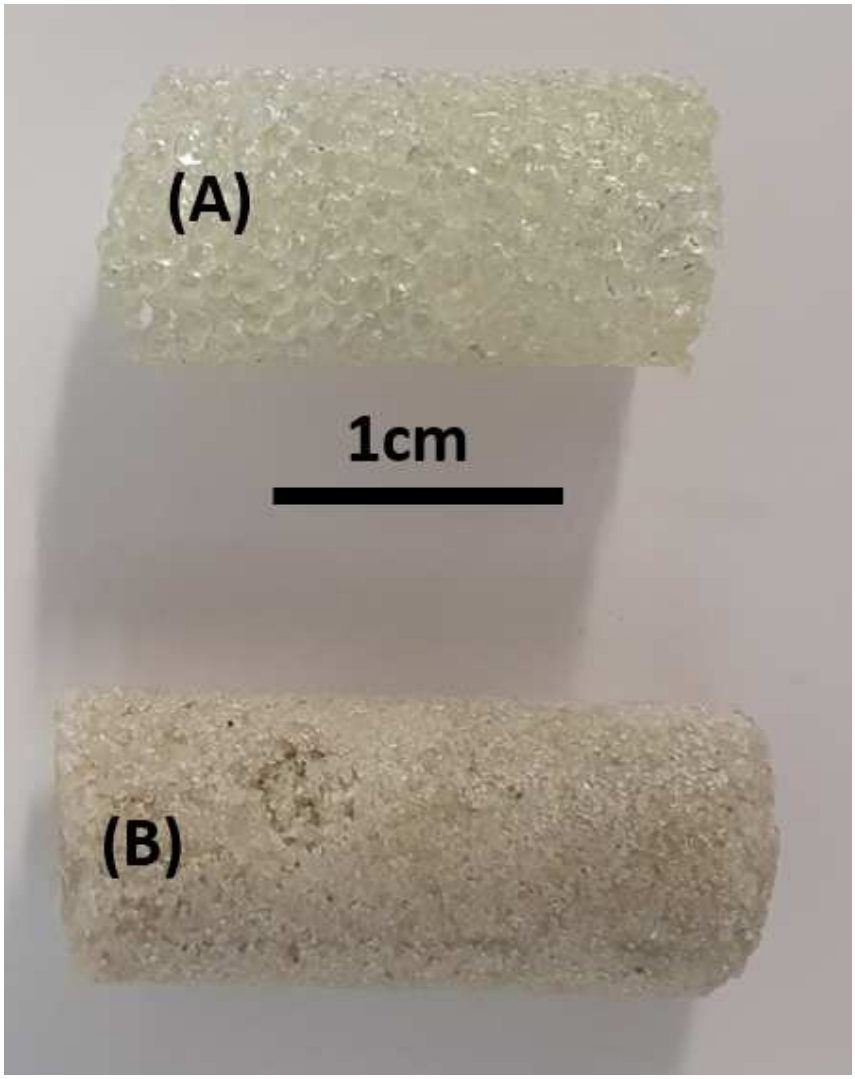

Figure 6: Consolidated porous media: (A) glass beads, (B) Fontainebleau sand

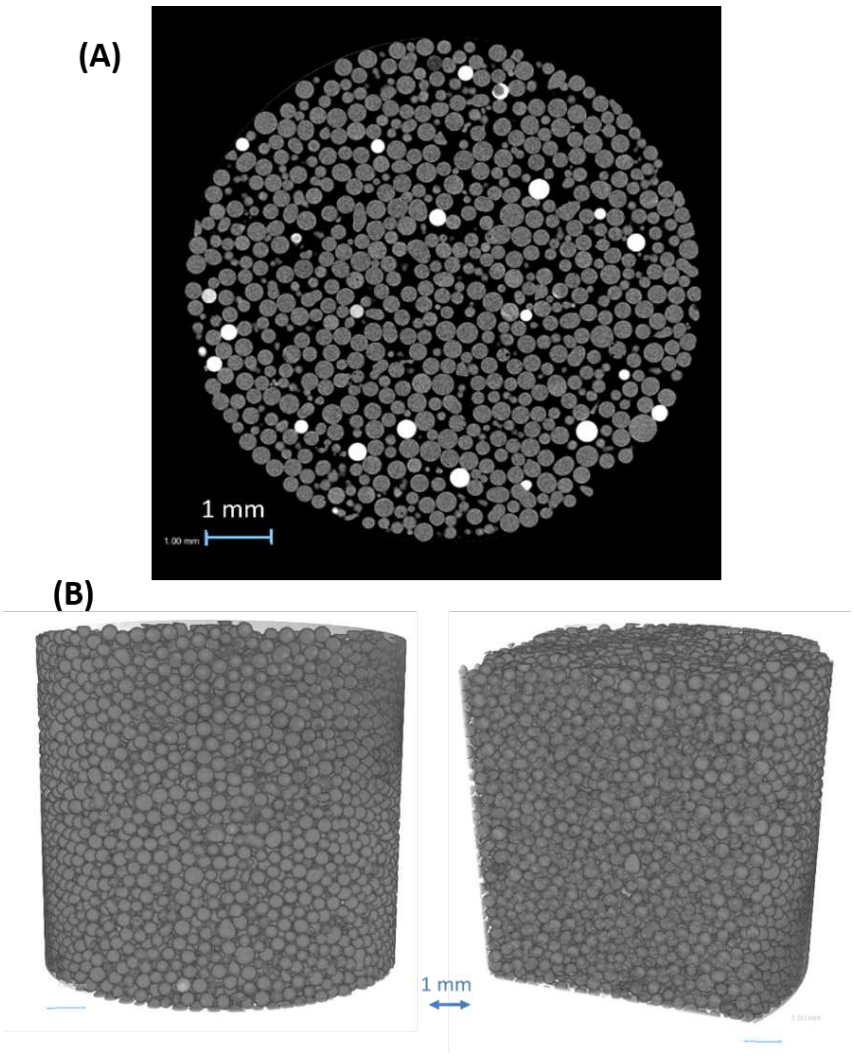

Figure 7: (a) horizontal cross section of the 3D reconstruction of the sample, (B) 3D rendering of the reconstruction of the resulted scan of the glass beads sample.

3. Porosity pre-definition

The mass of the epoxy resin left in the sample

$$M_{r_{\text{fin}}} = M_f - M_g \tag{1}$$

Where $M_{r_{\text{fin}}}$ is the mass of the resin left inside the sample, M_f is the final mass after vacuum evacuation of the mixture granular media - epoxy resin, and M_g is the mass of the granular media. From the density of the epoxy mixture (without the beads) which is $\rho_{\text{epoxy}} = 1.17$ g/cm^3, we can pre-calculate the porosity of our sample as shown below:

$$V_{r_{\text{fin}}} = M_{r_{\text{fin}}} \times \rho_{epoxy} \tag{2}$$

Where $V_{r_{\text{fin}}}$ is the final volume of epoxy left in the sample. The initial volume of void $V_{v_{\text{init}}}$ is calculated based on the initial porosity of the granular packing Φ_{init} and the volume of the mold V_t

$$V_{v_{\text{init}}} = \Phi_{\text{init}} \times V_t \tag{3}$$

The final volume of the void $V_{v_{\text{fin}}}$ is calculated as follows:

$$V_{v_{\text{fin}}} = V_{v_{\text{init}}} - V_{r_{\text{fin}}} \tag{4}$$

From there we can calculate the final porosity Φ_{fin}

$$\Phi_{\text{fin}} = \frac{V_{v_{\text{fin}}}}{V_t} \tag{5}$$

By adjusting the mass of the epoxy left in the granular media-epoxy mixture, we can predefine the porosity of the resulting consolidated porous media.

ECOLE DOCTORALE

ED 211 – Sciences exactes et leurs application

LABORATOIRE

Laboratoire des Fluides Complexes et leurs Réservoirs